Attosecond Four-Wave Mixing: A Tabletop Nonlinear Spectroscopy in the Extreme Ultraviolet

By

Yen-Cheng Lin

A dissertation submitted in partial satisfaction of the

requirements for the degree of

Doctor of Philosophy

in

Chemistry

in the

Graduate Division

of the

University of California, Berkeley

Committee in charge:

Professor Stephen R. Leone, Co-chair
Professor Daniel M. Neumark, Co-chair
Professor David Attwood

Summer 2023

Attosecond Four-Wave Mixing: A Tabletop Nonlinear Spectroscopy in the Extreme Ultraviolet

Abstract

Attosecond Four-Wave Mixing: A Tabletop Nonlinear Spectroscopy in the Extreme Ultraviolet

by

Yen-Cheng Lin

Doctor of Philosophy in Chemistry

University of California, Berkeley

Professor Stephen R. Leone, Co-chair
Professor Daniel M. Neumark, Co-chair

Nonlinear spectroscopies employ multiple short coherent pulses to generate higher-order polarization signals. The rich degrees of freedom available for controlling the properties of each beam enable highly selective measurements in both the frequency and time domains. Despite their widespread use with optical pulses, nonlinear spectroscopies have been relatively unexplored in the extreme ultraviolet (XUV) or X-ray spectral regions due to the lack of strong coherent light sources until recently. The objective of this project is to develop nonlinear spectroscopies in these short wavelength regions.

A table-top technique, attosecond FWM spectroscopy, has been successfully demonstrated, which utilizes a short attosecond XUV pulse and two noncollinear, few-cycle near-infrared pulses to generate background-free third-order polarization signals. The work detailed in this dissertation has broadened the scope of attosecond FWM spectroscopy and thus has taken the development of nonlinear spectroscopy in the XUV one step further. It includes the successful demonstration of probing ultrafast dynamics in molecules, such as O_2 and CO_2, and exploring the potential of non-resonant FWM process in a wave packet dynamic in Ar.

Looking ahead, the upcoming implementation of attosecond FWM experiments at the carbon K-edge will offer new avenues for investigating chemically and biologically significant organic molecules with nonlinear spectroscopies. Ultimately, attosecond FWM spectroscopy will serve as a solid foundation for future explorations in nonlinear spectroscopy at short wavelength, opening doors to innovative applications in various scientific fields.

Table of Contents

List of Figures

List of Tables

Acknowledgments

It has been a long journey to earn this PhD degree, and I wouldn't have reached this point without the help of many people. First, I would like to thank both of my research advisors, Professors Steve Leone and Dan Neumark. They provided support for the research project and gave proper advice when needed. I want to especially thank Steve for understanding the challenges that international students face and always supporting me whenever anything happened.

Secondly, I want to express my gratitude to all the partners in the Hill Atto project. Hugo and Ashley were my mentors when I first joined the project. Without them, I wouldn't have been able to gain a solid understanding of the project and achieve some success. Special thanks to Ashley for her efforts in preparing and considering a lot for the new apparatus before she left. Her contributions made my life in the 3rd and 4th year much easier. James and Nicki were my lab partners in the second half of my PhD journey. Without them, I couldn't have made the new apparatus work and taken the Hill Atto lab to the next level. Patrick joined just before I left, and I know that he and Nicki will take full advantage of the machine and elevate the Hill Atto project to new heights.

I also want to extend my thanks to everyone in the Leone and Neumark group, as well as the people at building 2, for all the informative scientific discussions we've had, especially with the people in the D93 project. I spent the first two months in the D93 project when I joined the group and learned a lot from Andrew and Lou. Also, thanks to Andrew, Val, and Eric for answering many of our questions when we were building the new apparatus. In the Hill Atto lab, Oliver Gessner and Dan Slaughter provided valuable help whenever we needed something urgently. Additionally, Robert Lucchese and William McCurdy are my theoretical collaborators, and without their assistance, I couldn't have published meaningful O2 and CO2 papers.

Mental health is crucial during the PhD journey, so I would also like to thank all my friends here. Every Taiwanese friend I have here is friendly, and I truly enjoy the time when we hang out together, especially with Sarah, Reichi, and Chin. Those moments when we play board games and share our grievances about the PhD life are the most relaxing times for me during the past few years. I knew Chin even before I came to Berkeley and want to thank her for helping me settle down at Berkeley in the beginning. Reichi has been my best friend here, and I'm incredibly grateful to her for always driving me around.

Chapter 1: Introduction

Nonlinear Spectroscopy has been widely applied to a variety of fields over the past few decades and has proven its power in probing structures and dynamics in complex chemical and biological systems [1-3]. However, most of the current nonlinear spectroscopies operate in the spectral regions of ultraviolet, visible, infrared, or electromagnetic radiation with even longer wavelengths, due to the limitation of reliable light sources. The recent advances in pulse generation in the extreme ultraviolet (XUV) and X-ray, including the development of high harmonic generation (HHG) [4,5], have enabled the applications of nonlinear spectroscopy in these shorter wavelength regions. This dissertation focuses on the experiments of a recently developed tabletop nonlinear spectroscopy in the extreme ultraviolet, that of attosecond four-wave mixing (FWM) spectroscopy [6-19]. In this chapter, the basic concept of nonlinear spectroscopy, as well as its extension to the XUV region, will be introduced.

1.1 Introduction to Nonlinear Spectroscopy

Spectroscopy is an important scientific technique that is used to study the interaction between light and matter. Light, as an electromagnetic radiation, can be absorbed, transmitted, or scattered, when it interacts with the matter. This interaction could be analyzed as a function of wavelength or frequency of the light and provide the detailed information about chemical and physical properties of the matter. Spectroscopy has numerous practical applications in a wide range of scientific disciplines, including physics, chemistry, astronomy, biology. For instance, it enables the study of chemical reaction dynamics and kinetics.

1.1.1 Linear Spectroscopy

There are several different types of spectroscopic techniques and one of the simplest methods is absorption spectroscopy [20,21]. A general schematic of absorption spectroscopy is shown in Figure 1.1. It consists of a light source (XUV pulse), a sample, a monochromator (grating), and a detector (CCD camera). When light passes through a certain sample, it could be absorbed, resulting in the attenuation of the intensity of the outgoing light. Absorption spectroscopies measure this intensity difference as absorbance:

$$A = \log\left(I_0/I\right) \tag{1.1}$$

where A represents the absorbance, I_0 is the intensity of the incident light, and I is the intensity of the outgoing light.

One of the interpretations of absorption is based on the concept of energy quantization. According to quantum mechanics, atoms, molecules, and other particles can exist only in discrete energy states. As illustrated in Figure 1.2, when the frequency of the incident light matches the energy difference between two energy states, it can induce transitions between these states. The transition is accompanied by the absorption of photons. The absorbance is related to the collision probability between photon and sample particles and in a uniform sample it could be described with the well-known Beer-Lambert Law:

$$A(\omega) = \sigma(\omega) ln \tag{1.2}$$

where $\sigma(\omega)$ is the absorption cross section as a function of frequency, l is the sample

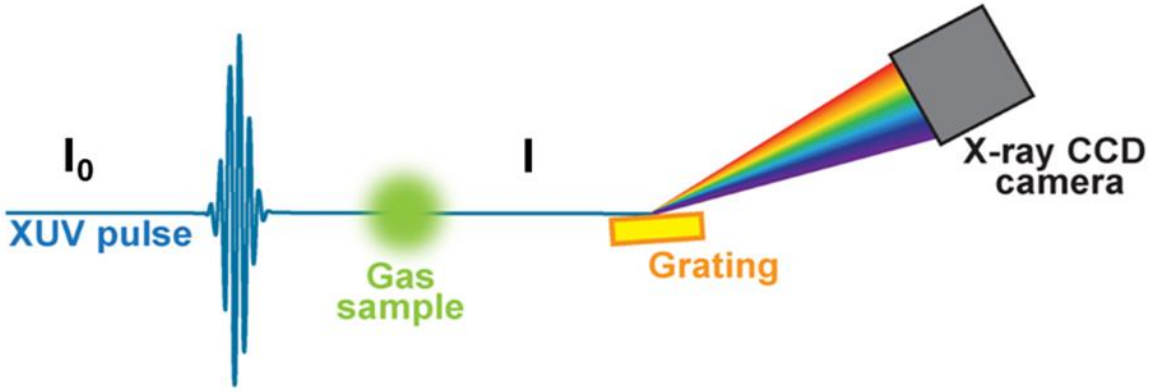

Figure 1.1 ***Schematic of a XUV absorption spectroscopy.*** *There are four major components of absorption spectroscopy including a light source (XUV pulse), a sample, a monochromator (grating), and a detector (CCD camera).*

distance that light passes through, and n is the number density of the sample. Since the absorption cross section is characteristic of the matter being studied, Equation (1.2) explains how spectroscopy is used for analysis of composition, structure, and properties of materials.

While interpretations of absorption using the photon nature of the light are easier to understand, it is sometimes more useful to describe light in the form of an electromagnetic wave [22-26]. In this view, the interaction between light and matter is treated as the propagation of an electromagnetic wave through a dielectric medium. During the propagation process, the oscillating electric filed in the light could induce an oscillating electric dipole in the medium, which is also known as polarization. In a homogeneous, isotropic dielectric medium, polarization usually depends linearly on the electric field, especially when the intensity of the light is weak. This relationship can be described by the following equation:

$$P = \varepsilon_0 \chi E \tag{1.3}$$

where P represents the polarization, ε_0 is the vacuum permittivity, χ is called the electric susceptibility of the matter, and E is the electric field of the light in free space.

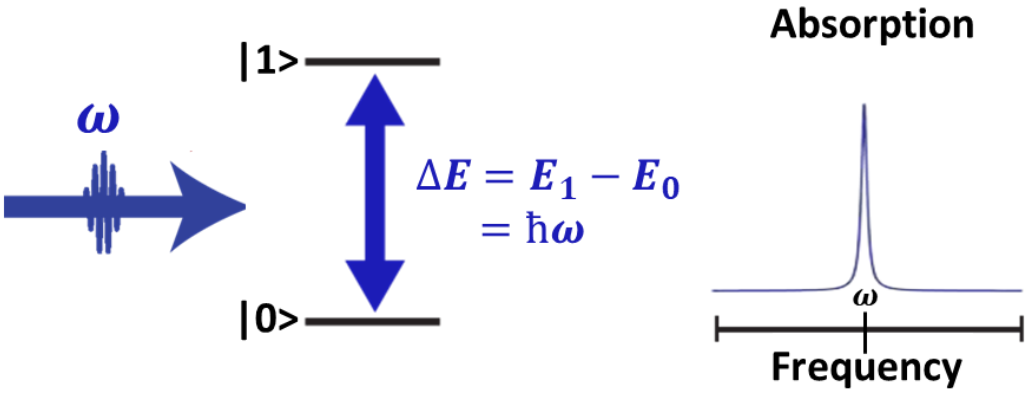

Figure 1.2 ***Concept of energy quantization and absorption.*** *In a quantum system, particles exist in discrete energy states. Absorption of light occurs when the energy difference between these states matches the frequency of the incident light.*

The oscillating nature of the polarization will emit another oscillating electric field, which is typically out of the phase with the incident light field [24], leading to destructive interference, as shown in Figure 1.3. This destructive interference results in the attenuation of light intensity and is the origin of absorption. Since Equation (1.3) is a linear equation, spectroscopies that utilize this behavior are referred to as linear spectroscopy.

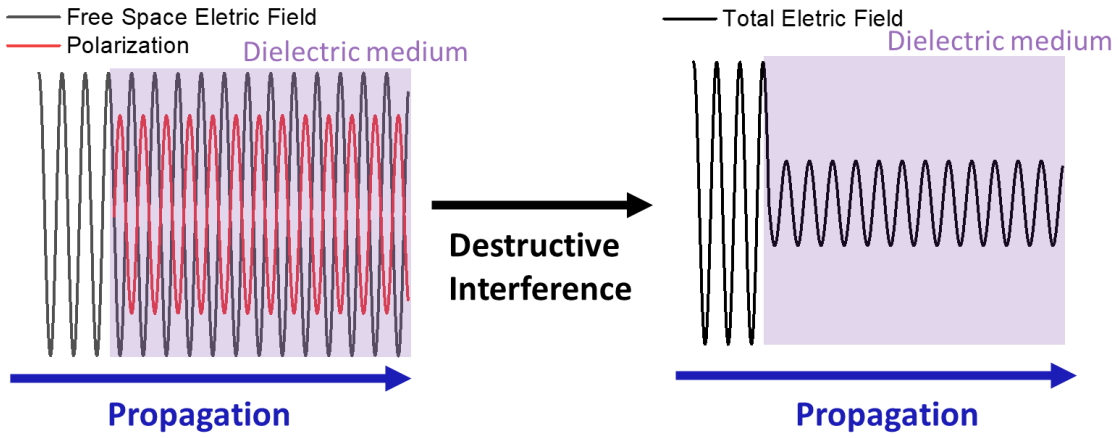

Figure 1.3 ***Induced polarization in the medium.*** *The field generated by the polarization is usually out of the phase with the incident field of light in the free space. The resulting destructive interference attenuates the intensity of the field in the medium.*

1.1.2 Time Dependent Perturbation Theory

To connect the electromagnetic wave nature of the light with quantum mechanics, treatment with time dependent perturbation theory is introduced in this subsection [24,25,27]. For simplicity, this subsection focuses on a two-level system comprising a ground state and an excited state.

Consider a 2-level system with field-free Hamiltonian $\hat{H}_0$:

$$\hat{H}_0 = \begin{pmatrix} E_0 & 0 \\ 0 & E_1 \end{pmatrix} \tag{1.4}$$

where E_0 and E_1 are the energy eigenvalues for the ground state $|0\rangle$ and excited state $|1\rangle$, respectively. Solving the time-dependent Schrödinger equation gives the expression of the time-dependent wavefunction $|\Psi(t)\rangle$ in the field free region:

$$|\Psi(t)\rangle = \mathrm{c}_0 e^{-iE_0 t/\hbar}|0\rangle + \mathrm{c}_1 e^{-iE_1 t/\hbar}\,|1\rangle \tag{1.5}$$

Here, c_0 and c_1 are just constants. Now, let's introduce light to the system as an oscillating electric field $E(t)$:

$$E(t) = E'(t)\cos(\omega t) \tag{1.6}$$

The energy of interaction between the system and this field, $\hat{W}(t)$, is determined by the dipole of the system $\hat{\mu}$ and the strength of electric field:

$$\hat{W}(t) = -\hat{\mu}E(t) \tag{1.7}$$

The total Hamiltonian with the present of the electric field is the sum of $\widehat{H}_0$ and $\widehat{W}(t)$:

$$\widehat{H} = \widehat{H}_0 + \widehat{W}(t) \tag{1.8}$$

To solve the time dependent Schrödinger equation with this total Hamiltonian, it is assumed that $\widehat{W}(t) \ll \widehat{H}_0$ and the first order time-dependent perturbation theory is applied to get a set of differential equations with $\omega_{01} \equiv (E_1 - E_0)/\hbar$:

$$\begin{aligned} \frac{\partial}{\partial t}\mathrm{c}_1(t) &= \frac{i}{\hbar}\mathrm{c}_0(t)e^{-i\omega_{01}t}\langle 1|\hat{\mu}|0\rangle E(t) \\ \frac{\partial}{\partial t}\mathrm{c}_0(t) &= \frac{i}{\hbar}\mathrm{c}_1(t)e^{-i\omega_{01}t}\langle 0|\hat{\mu}|1\rangle E(t) \end{aligned} \tag{1.9}$$

This set of differential equations is complicated and mostly solved numerically especially with complicated shapes of the pulse $E'(t)$. However, Equation (1.9) suggests that the effect of the light field is just to change coefficient c_0 and c_1 and thus prepare a different wave packet for the system. For now, the behavior of the system when a light field is present is ignored, and the focus is on the evolution of the system before and after the light pulse.

For most of the experiments introduced in this dissertation, the system was in its ground state $|0\rangle$ before an XUV pulse approached. The XUV pulse then excited the system from the ground state $|0\rangle$ to the excited state $|1\rangle$. Thus, the system will be in a superposition of the eigenstates $|0\rangle$ and $|1\rangle$ after XUV pulse passes by, as illustrated in Figure 1.4. The wavefunction of the system after the XUV pulse could be written as

$$|\Psi(t)\rangle = \mathrm{c}_0(t)|0\rangle + i\mathrm{c}_1(t)|1\rangle = \mathrm{c}_0 e^{-iE_0 t/\hbar}|0\rangle + i\mathrm{c}_1 e^{-iE_1 t/\hbar}\, e^{-t/2\tau}|1\rangle \tag{1.10}$$

Slightly different from Equation (1.5), here, 'i' is added before c_1 to ensure that both c_0 and c_1 are real numbers and this equation originates from Equation (1.9). A decay term $e^{-t/2\tau}$ is also added after c_1 as the lifetimes of XUV excited states are usually short. In a typical XUV experiment, since the XUV intensity is weak, $\mathrm{c}_1 \ll \mathrm{c}_0$ and $\mathrm{c}_0 \approx 1$. Thus, the imaginary part of c_0 is ignored. The light-induced polarization is the expectation value of the transition dipole:

$$P(t) = \langle\hat{\mu}\rangle = \langle\Psi(t)|\hat{\mu}|\Psi(t)\rangle = \mathrm{c}_0\mathrm{c}_1\langle 0|\hat{\mu}|1\rangle \sin(\omega_{01}\mathrm{t})\, e^{-t/2\tau} + c.c. \tag{1.11}$$

According to Equation (1.11), the polarization oscillates at frequency ω_{01} and decays with $e^{-t/2\tau}$, as illustrated in Figure 1.4. Also, according to Maxwell's equations [24,26], the oscillating polarization will create an electromagnetic wave that is phase-shifted by 90 degrees. Thus, with $P(t) \sim \sin(\omega_{01}\mathrm{t})$, the emitted electric field will be proportional to $-\cos(\omega_{01}\mathrm{t})$, which has the opposite sign of the incident field. This results in a destructive interference and absorption as discussed before in Subsection 1.1.1.

The wavefunction picture used so far can only be applied to a pure quantum state that produces a coherent superposition. However, quantum systems in a statistical ensemble of states are also possible. To address this, the density matrix is introduced:

$$\rho(t) = \sum_s |\Psi_s(t)\rangle\langle\Psi_s(t)| \tag{1.12}$$

Here, $\Psi_s(t)$ represents a pure state wavefunction. If the entire system is in one pure state with the wavefunction form described in Equation (1.10), one can write the density matrix as:

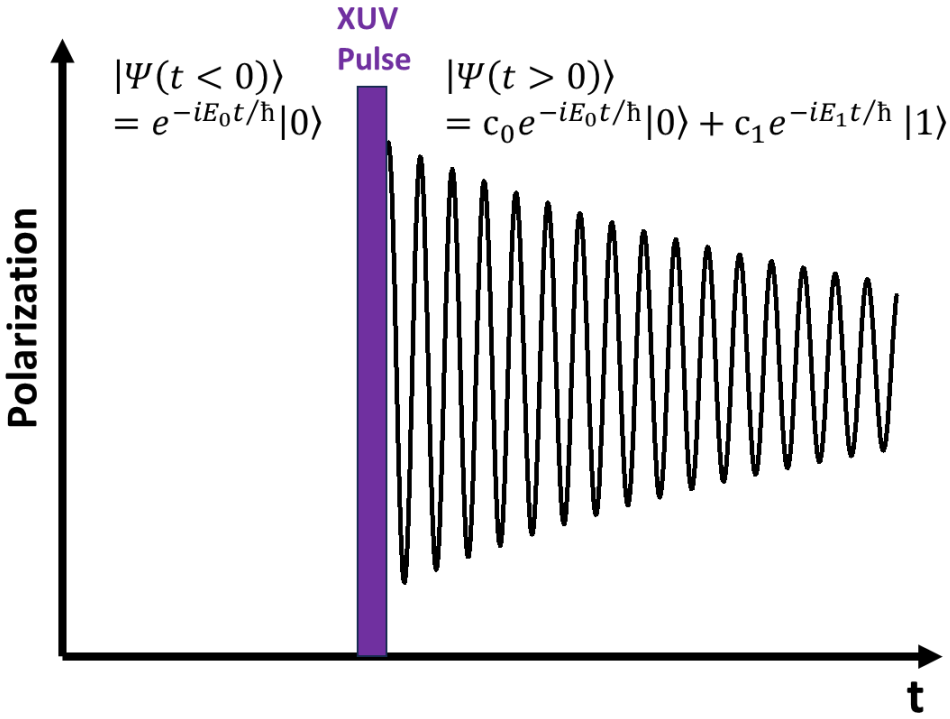

Figure 1. 4 ***Wave packet and polarization after XUV pulse.*** *The system was in its ground state and the XUV pulse excites the ground state to an excited state creating a wave packet consisting of a linear combination of ground and excited state.*

$$\rho(t) = \begin{pmatrix} c_0^2 & -ic_0c_1e^{+i\omega_{01}t}e^{-t/2\tau} \\ ic_0c_1e^{-i\omega_{01}t}e^{-t/2\tau} & c_1^2e^{-t/\tau} \end{pmatrix} \tag{1.13}$$

Recall that polarization is the expectation value of the transition dipole, and the expectation value of the system can be expressed using the density matrix as

$$P(t) = \langle\hat{\mu}\rangle = Tr(\hat{\mu}\rho(t)) \tag{1.14}$$

The Equation (1.14) gives the same results for the polarization as Equation (1.11), confirming the density matrix method is equivalent to the wavefunction picture for a pure state.

A more general form of density matrix $\rho(t)$ of the statistical ensemble of states generated by the light field is written as follows [24]:

$$\rho(t) = \begin{pmatrix} \langle c_0(t)c_0^*(t)\rangle & -i\langle c_0(t)c_1^*(t)\rangle \\ i\langle c_1(t)c_0^*(t)\rangle & \langle c_1(t)c_1^*(t)\rangle \end{pmatrix} = \begin{pmatrix} \rho_{00} & -\rho_{01}e^{+i\omega t}e^{-t/T_2} \\ \rho_{10}e^{-i\omega t}e^{-t/T_2} & \rho_{11}e^{-t/T_1} \end{pmatrix} \tag{1.15}$$

Here, ω is the frequency of the incident light, and T_1 and T_2 are some decay constants. In the density matrix, the diagonal elements correspond to the populations of the ground and excited states, while the off-diagonal elements describe the coherence between both states. Equation (1.15) suggests that the coherence generated by the photoexcitation oscillates at the frequency of incident light and decay with a so-called dephasing time T_2, while the population decays with a population lifetime T_1 [24,28]. These two lifetimes are related by the equation:

$$\frac{1}{T_2} = \frac{1}{2T_1} + \frac{1}{T_2^*} \tag{1.16}$$

where T_2^* represents the pure dephasing time due to the fluctuations of the environment. For a pure state or in most of the gas-phase systems, as discussed in this dissertation, T_2^* can be neglected to establish the relationship:

$$T_2 = 2T_1 \tag{1.17}$$

This relationship is indeed also implied in Equation (1.13). Since the dipole operator $\hat{\mu}$ only consists of off-diagonal matrix elements:

$$\hat{\mu} = \begin{pmatrix} 0 & \mu_{01} \\ \mu_{10} & 0 \end{pmatrix} \tag{1.18}$$

Only the off-diagonal elements in the density matrix, or the coherence, contributed to the polarization and emit electric field. Therefore, nonlinear spectroscopies are usually more sensitive to coherence than population, while the excited state population lifetime is of greater interest in most of the topic discussed in this dissertation. Equation (1.18) is essential in connecting the measurements to the physics of interest.

Now that the behaviors of the system before and after the light pulse have been discussed, the focus shifts to the evolution of the system when the pulse is present. Instead of solving Equation (1.9), which is based on the wave function picture, the density matrix will be used for a more generalized description throughout the rest of this subsection. The temporal evolution of the density matrix follows the Liouville–von Neumann equation:

$$\frac{d}{dt}\rho(t) = -\frac{i}{\hbar}\left[\hat{H}, \rho(t)\right] \tag{1.19}$$

With the relationship shown in Equation (1.19) and the application of perturbation theory, the first order correction of the density matrix can be calculated by assuming the light field is a δ-function in time and only present at t=0:

$$\rho^{(1)} \sim i(\hat{\mu}(0)\rho(-\infty) - \rho(-\infty)\hat{\mu}(0)) \tag{1.20}$$

Here, $\rho(-\infty)$ represents the density matrix of the system before the light pulse arrives. For simplicity, Equation (1.20) is written in a unit-less form, and the intensity of the light field is neglected. A first-order response function $S^{(1)}$ can be defined as the polarization induced by a δ-function field and could be calculated using Equation (1.14) and (1.20):

$$S^{(1)}(t_1) = i\langle\hat{\mu}(t_1)\hat{\mu}(0)\rho(-\infty)\rangle - i\langle\rho(-\infty)\hat{\mu}(0)\hat{\mu}(t_1)\rangle \tag{1.21}$$

where the angle bracket takes the trace of the matrix. The second term of the response function is the complex conjugate of the first term, so only the calculation of the first term is performed below. Here, it is assumed that the density matrix starts in its ground state:

$$\rho(-\infty) = \begin{pmatrix} 1 & 0 \\ 0 & 0 \end{pmatrix} \tag{1.22}$$

The dipole operator in Equation (1.18) is rewritten with a unit-less form:

$$\hat{\mu} = \begin{pmatrix} 0 & 1 \\ 1 & 0 \end{pmatrix} \tag{1.23}$$

Then the first term in Equation (1.20) can be calculated:

$$i\hat{\mu}(0)\rho(-\infty) = \begin{pmatrix} 0 & 0 \\ i & 0 \end{pmatrix} \tag{1.24}$$

This is the first order correction to the density matrix at time zero when interacting with the light field. This density matrix will then evolve in a field-free condition as given by Equation (1.15):

$$e^{-i\omega t_1} e^{-t_1/T_2} i\hat{\mu}(0)\rho(-\infty) = \begin{pmatrix} 0 & 0 \\ ie^{-i\omega t_1} e^{-t_1/T_2} & 0 \end{pmatrix} \tag{1.25}$$

The first term of the first-order response function is then:

$$i\langle \hat{\mu}(t_1)\hat{\mu}(0)\rho(-\infty)\rangle = \langle \begin{pmatrix} 0 & 1 \\ 1 & 0 \end{pmatrix} * \begin{pmatrix} 0 & 0 \\ ie^{-i\omega t_1} e^{-t_1/T_2} & 0 \end{pmatrix} \rangle = ie^{-i\omega t_1} e^{-t_1/T_2} \tag{1.26}$$

The complete first-order response function can be obtained now since the first term is determined and the second term is simply the complex conjugate of the first term:

$$S^{(1)}(t_1) = ie^{-i\omega t_1} e^{-t_1/T_2} - ie^{+i\omega t_1} e^{-t_1/T_2} = R^{(1)}(t_1) + R^{*(1)}(t_1) \tag{1.27}$$

Here, $R^{(1)}(t_1) = ie^{-i\omega t_1} e^{-t_1/T_2}$ is defined for future usage. Recall that the first-order response function represents the polarization of the system induced by a δ-function of pulse field at t=0. To obtain the first order polarization induced by any shape of pulse $E'(t)$, a convolution integral is utilized:

$$P^{(1)}(t) = \int_0^\infty dt_1 \, E'(t - t_1) S^{(1)}(t_1) \tag{1.28}$$

The electric field $E(t)$ can be further expanded into a pair of conjugate complex terms:

$$E'(t) = 2E''(t)\cos(\omega t) = E''(t)\left(e^{-i\omega t} + e^{+i\omega t}\right) = E(t) + E^*(t) \tag{1.29}$$

And the Equation (1.28) is rewritten:

$$P^{(1)}(t) = \int_0^\infty dt_1 \, [E(t - t_1) + E^*(t - t_1)][R^{(1)}(t_1) + R^{*(1)}(t_1)] \tag{1.30}$$

There are four different terms in the first order polarization, each term representing a certain quantum pathway. These terms can be illustrated in a set of double-side Feynman diagrams as shown in Figure 1.5.

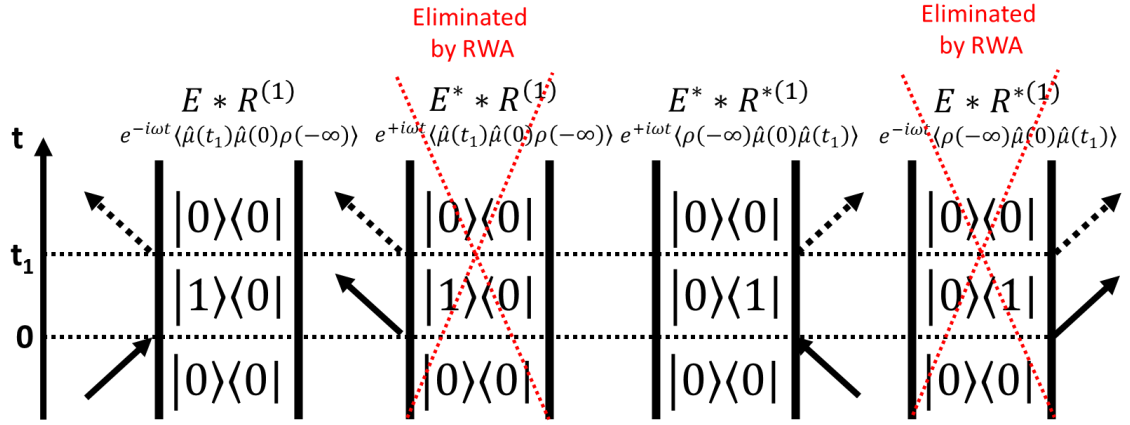

Figure 1.5 ***Double sided Feynman diagrams of linear response.*** *There are four different terms in the first order polarization representing four different possible quantum pathways in the Feynman diagrams. However, only two of them will survive the Rotating Wave Approximation while the other two will be eliminated.*

In these Feynman diagrams, two vertical lines represent the time evolution of the density matrix from the bottom to the top. Interaction with the dipole operator could be applied to either the ket or the bra of the density matrix and are represented by arrows. An arrow pointing to the right represents a field with $e^{-i\omega t}$, while an arrow pointing to the left represents a field with $e^{+i\omega t}$. An arrow pointing towards the system represents an excitation, while an arrow pointing away from the system represents a de-excitation.

Using the results from Equation (1.27), the integral in Equation (1.30) can be calculated. Two of the terms in Equation (1.30) contain some highly oscillating functions in the Integral, as shown below:

$$\int_0^\infty dt_1\, E^*(t-t_1)R^{(1)}(t_1) = ie^{+i\omega t}\int_0^\infty dt_1\, E''(t-t_1)e^{-i2\omega t_1}e^{-t_1/T_2} \tag{1.31}$$

$$\int_0^\infty dt_1\, E(t-t_1)R^{*(1)}(t_1) = ie^{-i\omega t}\int_0^\infty dt_1\, E''(t-t_1)e^{+i2\omega t_1}e^{-t_1/T_2} \tag{1.32}$$

These two terms could be neglected by making the so-called rotating wave approximation (RWA). As shown in Figure 1.5, only the other two terms contribute to the first order polarization within the RWA, and they are complex conjugates of each other. The RWA has an intuitive physical interpretation: both pathways that are eliminated by the RWA have their first step as de-excitation of a ground state. The RWA ensures that the excited state is not lower than the ground state in energy.

Now that the first order polarization is calculated by using time-dependent perturbation theory, the absorption due to the destructive interference can be described in a more quantitative way. Recall that the polarization creates an electromagnetic wave that is phase-shifted by 90 degrees:

$$E_{sig}(t) = iP(t) \tag{1.33}$$

The absorption can be calculated using the emitted field:

$$\begin{aligned} A(\omega) &= -\log\left(\frac{I(\omega)}{I_0(\omega)}\right) = -\log\left(\frac{|E_0(\omega)+E_{sig}(\omega)|^2}{|E_0(\omega)|^2}\right) \\ &= -\log\left(1+\frac{2*Re\left(E_0(\omega)E_{sig}(\omega)\right)+|E_{sig}(\omega)|^2}{|E_0(\omega)|^2}\right) \end{aligned} \tag{1.34}$$

where E_0 is the electric field of the incident light. In this Equation, all the functions are written as a function of frequency ω. $E_{sig}(\omega)$ is just the Fourier transform of $E_{sig}(t)$. Here, it is assumed that the $E_{sig}(t) \ll E_0(\omega)$, allowing us to expand the log function with small x approximation and eliminate the $|E_{sig}(\omega)|^2$ term, resulting in this expression:

$$\begin{aligned} A(\omega) &\propto Re\left(E_{sig}(\omega)\right) \propto Re\left(\int_0^\infty dt_1\, e^{-i(\omega-\omega_{01})t}e^{-t_1/T_2}\right) \\ &\propto Re\left(\frac{1}{i(\omega-\omega_{01})-1/T_2}\right) \propto \frac{1/T_2}{(\omega-\omega_{01})^2+1/{T_2}^2} \end{aligned} \tag{1.35}$$

Equation (1.35) suggests the absorption line shape in linear spectroscopy will be a Lorentzian line shape function. It also reveals that the spectral line width is related to the excited state decay time:

$$\Delta E * \Delta t = \hbar\Delta\omega * T_1 = \hbar/\mathbf{2} * \Delta\omega * T_2 \geq \hbar/\mathbf{2} \tag{1.36}$$

Here, ΔE represents the spectral linewidth in the unit of energy, and Δt is equivalent to the excited state lifetime, T_1. Equation (1.17) is used to relate T_1 to T_2. Equation (1.36) suggests that linewidth measurements in the frequency domain can provide meaningful information about the lifetime of ultrafast dynamics. However, these measurements may be influenced by artificial spectral broadening, such as Doppler broadening. Additionally, spectral congestion caused by multiple quantum states being close in energy could sometimes make it difficult to determine the linewidth accurately [29]. As a result, direct measurements in the time domain will provide the most accurate results for studying ultrafast dynamics. This could be performed using nonlinear spectroscopy.

1.1.3 Nonlinear Spectroscopy

When the light field is intense, the linear relationship described in the Equation (1.3) will no longer hold and the polarization function must be expanded to include some higher order terms [24,25]:

$$P = P^{(1)} + P^{(2)} + P^{(3)} + \cdots = \varepsilon_0(\chi^{(1)}E + \chi^{(2)}E^2 + \chi^{(3)}E^3 + \cdots) \tag{1.37}$$

Here, $P^{(n)}$ represents the n-th order polarization, and $\chi^{(n)}$ denotes the n-th order susceptibility. Spectroscopies that involve the higher order polarization are defined as nonlinear spectroscopy. The 2-nd order polarization $P^{(2)}$ has its own importance in applications such as second harmonic generation but vanish in a centrosymmetric medium due to the symmetry considerations [25]. The third-order polarization $P^{(3)}$ is thus the lowest universal nonlinear term and forms the basis for most of the nonlinear spectroscopies.

In the various form of nonlinear spectroscopies, multiple short coherent light pulses are typically used instead of a single pulse to generate a nonlinear polarization. For example, one can use three different incident light fields to interact with the medium and generate a third-order polarization $P^{(3)}$, which will emit a fourth field, as shown in Figure 1.6. A better mathematical form for third-order polarization $P^{(3)}$ is then:

$$P^{(3)} = \varepsilon_0\chi^{(3)}E_1E_2E_3 \tag{1.38}$$

Here, E_1, E_2, and E_3 denote the electric fields of three different incident light fields. During the nonlinear process, two basic physical laws must be obeyed: conservation of energy and conservation of momentum. Conservation of energy requires the frequency of the emitted signal ω_4 to be the sum or difference of the frequencies of the incident fields ω_1, ω_2, and ω_3:

$$\omega_4 = \pm\omega_1 \pm \omega_2 \pm \omega_3 \tag{1.39}$$

Meanwhile, Conservation of momentum, also known as the phase matching condition, requires the wavevector of the emitted signal $\overrightarrow{k_4}$ to be the sum or difference of the wavevectors of the incident fields $\overrightarrow{k_1}$, $\overrightarrow{k_2}$, and $\overrightarrow{k_3}$:

$$\overrightarrow{k_4} = \pm\overrightarrow{k_1} \pm \overrightarrow{k_2} \pm \overrightarrow{k_3} \tag{1.40}$$

One of the examples of phase matching is also provided in Figure 1.6. These two conditions add some constraints in the nonlinear process. They could also be used to differentiate and isolate the different possible quantum pathways in the nonlinear spectroscopy, which will be discussed later.

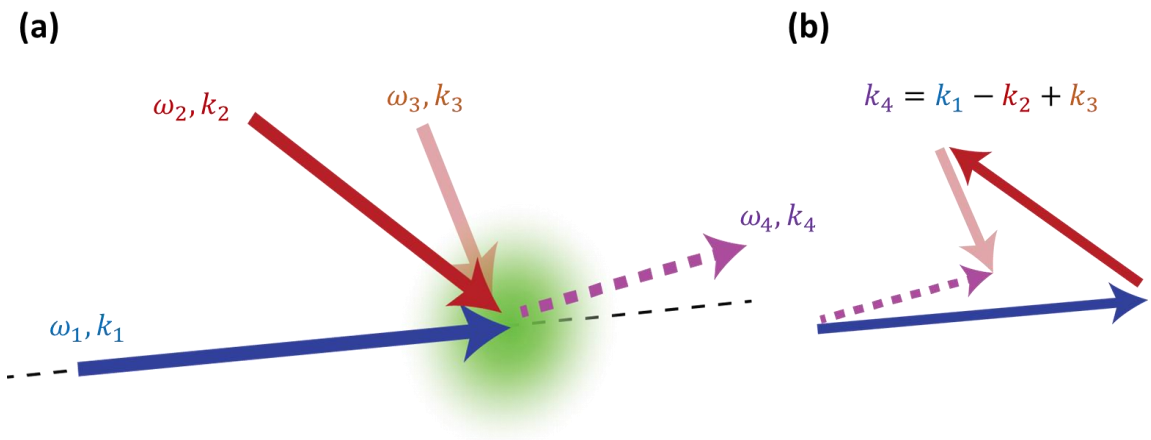

Figure 1.6 ***Scheme of generation of third order polarization.*** *(a) Three different incident light fields interact with the medium to generate third-order polarization and emit a fourth light field. (b) Phase matching condition is used to determine the wavevector of the emit field.*

The perturbation method described in Subsection 1.1.2 can be extended to explain the nonlinear spectroscopy. Specifically, the polarization is the convolution integral of the electric fields and response function, and each n-th order polarization $P^{(n)}$ will have a corresponding n-th order response function $S^{(n)}$. Third order polarization $P^{(3)}$ is expressed with this assumption:

$$P^{(3)}(t) \propto \int_0^\infty dt_3 \int_0^\infty dt_2 \int_0^\infty dt_1 \, E_3'(t-t_3)E_2'(t-t_3-t_2) \\ * E_1'(t-t_3-t_2-t_1)S^{(3)}(t_3,t_2,t_1) \tag{1.41}$$

where t_n are time variables defined by the pulse sequence. A scheme of pulse sequence is illustrated in Figure 1.7. Since time zero is arbitrary, the timing of the first pulse is set as time zero. t_1 is the time difference between the first and the second pulses, t_2 is the time difference between the second and the third pulses, and t_3 is the time difference between the third pulse and emitted polarization. Equation (1.21) is extended to obtain the third order response function $S^{(n)}$:

$$S^{(3)}(t_3,t_2,t_1) \propto i\,\langle \hat{\mu}(t_3+t_2+t_1)\left[\hat{\mu}(t_2+t_1),\left[\hat{\mu}(t_1),[\hat{\mu}(0),\rho(-\infty)]\right]\right]\rangle \\ = i\,\langle \hat{\mu}_3\left[\hat{\mu}_2,\left[\hat{\mu}_1,[\hat{\mu}_0,\rho(-\infty)]\right]\right]\rangle \tag{1.42}$$

The expansion of triple nested commutators will yield eight different terms and four of them are just complex conjugates of the other four:

$$i\,\langle \hat{\mu}_3\left[\hat{\mu}_2,\left[\hat{\mu}_1,[\hat{\mu}_0,\rho(-\infty)]\right]\right]\rangle = \\ \begin{aligned} &i\langle \hat{\mu}_3\hat{\mu}_1\,\rho(-\infty)\hat{\mu}_0\hat{\mu}_2\rangle - i\langle \hat{\mu}_2\hat{\mu}_0\,\rho(-\infty)\hat{\mu}_1\hat{\mu}_3\rangle && \Longrightarrow R_1 + R_1^* \\ &i\langle \hat{\mu}_3\hat{\mu}_2\,\rho(-\infty)\hat{\mu}_0\hat{\mu}_1\rangle - i\langle \hat{\mu}_1\hat{\mu}_0\,\rho(-\infty)\hat{\mu}_2\hat{\mu}_3\rangle && \Longrightarrow R_2 + R_2^* \\ &i\langle \hat{\mu}_3\hat{\mu}_0\,\rho(-\infty)\hat{\mu}_1\hat{\mu}_2\rangle - i\langle \hat{\mu}_2\hat{\mu}_1\,\rho(-\infty)\hat{\mu}_0\hat{\mu}_3\rangle && \Longrightarrow R_3 + R_3^* \\ &i\langle \hat{\mu}_3\hat{\mu}_2\hat{\mu}_1\hat{\mu}_0\,\rho(-\infty)\rangle - i\langle\,\rho(-\infty)\hat{\mu}_0\hat{\mu}_1\hat{\mu}_2\hat{\mu}_3\rangle && \Longrightarrow R_4 + R_4^* \end{aligned} \tag{1.43}$$

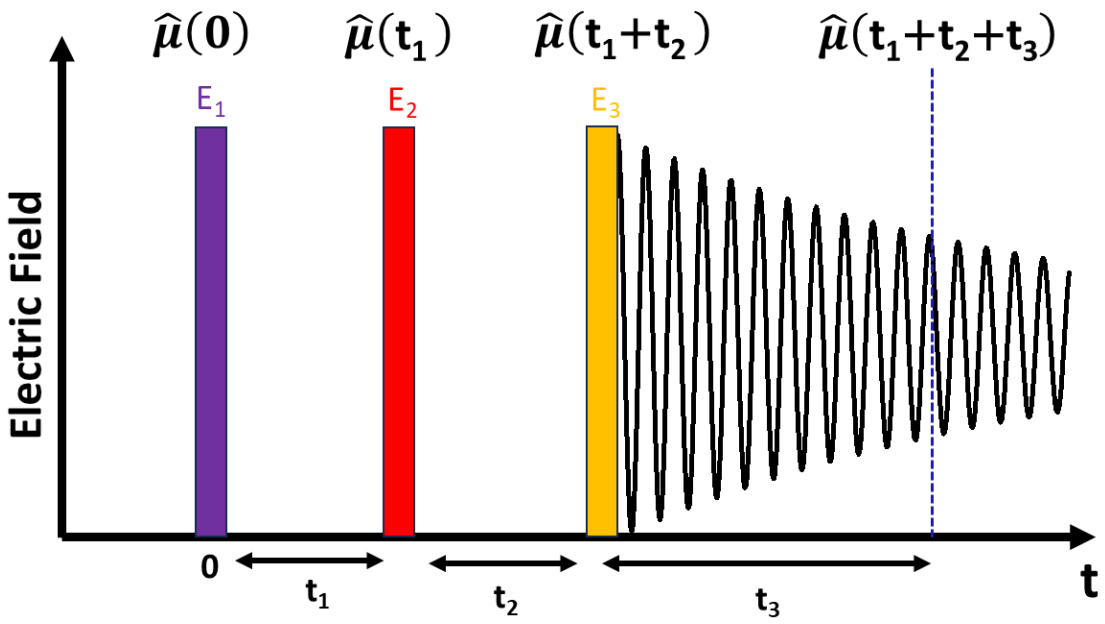

Figure 1.7 ***Scheme of pulse sequence for a three-pulse experiment.*** *Time zero is set as the timing of the first pulse, and subsequent pulses are delayed accordingly: the second pulse by t_1, the third pulse by another t_2 with respect to the second pulse, and finally, the polarization is created and emits a field after the third pulse with an additional time delay of t_3.*

For the polarization, each term in the response function will be multiplied by E_1, E_2, and E_3, which, when fields are expressed in the complex conjugate pairs, yields eight terms. Fortunately, with the RWA, only one term survives for each term in the response function. There are thus a total of eight pathways in the third-order polarization, which are illustrated in Figure 1.8. Note that, some of the pathways are eliminated by RWA only in a two-level system. For example, an additional pathway R_5 that could be allowed in a three-level system is shown in Figure 1.8.

Since there are many possible pathways to generate third-order polarization, sometimes the separation of pathways is needed to simplify the interpretation of nonlinear spectroscopies. One of the easiest ways is to measure the frequency of the emitted field. For example, pathway R_5 emitted the field at frequency of ω_{12} while pathway R_1 emitted the field at frequency of ω_{01}. They can thus be differentiated based on the difference in frequency. Another commonly used approach to differentiate different pathways is to utilize the phase matching condition. For pathway R_1, the wavevector of the emitted field will be $-k_1+k_2+k_3$, while for pathway R_3, the wavevector of the emitted field will be $k_1-k_2+k_3$. With proper design of the beam geometry, the signals from these pathways could be spatially isolated.

While the frequencies and wavevectors of the incident pulses can be used to distinguish different pathways of the third-order polarization signals, controlling the pulse sequence allows us to gain information on the dynamics. For example, by using the same method that led to Equation (1.26), one could derive the functional form for pathway R_1 [24]:

$$R_1(t_1, t_2, t_3) \propto e^{-i\omega_{01}t_1}e^{-t_1/T_2} * e^{-t_2/T_1} * e^{-i\omega_{01}t_3}e^{-t_3/T_2} \quad (1.44)$$

This suggests that by recording the signal generated by the R_1 pathway while changing the delay t_1 and t_2, information for T_2 and T_1 could be obtained, respectively. The functional form for different pathways can also be calculated, and they may carry distinct dynamics information, especially in multi-level systems.

Nonlinear spectroscopy has broader applications than linear spectroscopy due to the extra degrees of freedom introduced by additional pulses. For example, with the proper pathway, nonlinear spectroscopy could be used to access the information of 1-photon forbidden states [18]. With the development of multidimensional spectroscopies, nonlinear spectroscopy also has the capability to disentangle the coupling between multiple degrees of freedom in complex chemical systems [1-3]. Overall, nonlinear spectroscopic techniques are powerful tools with a variety of applications.

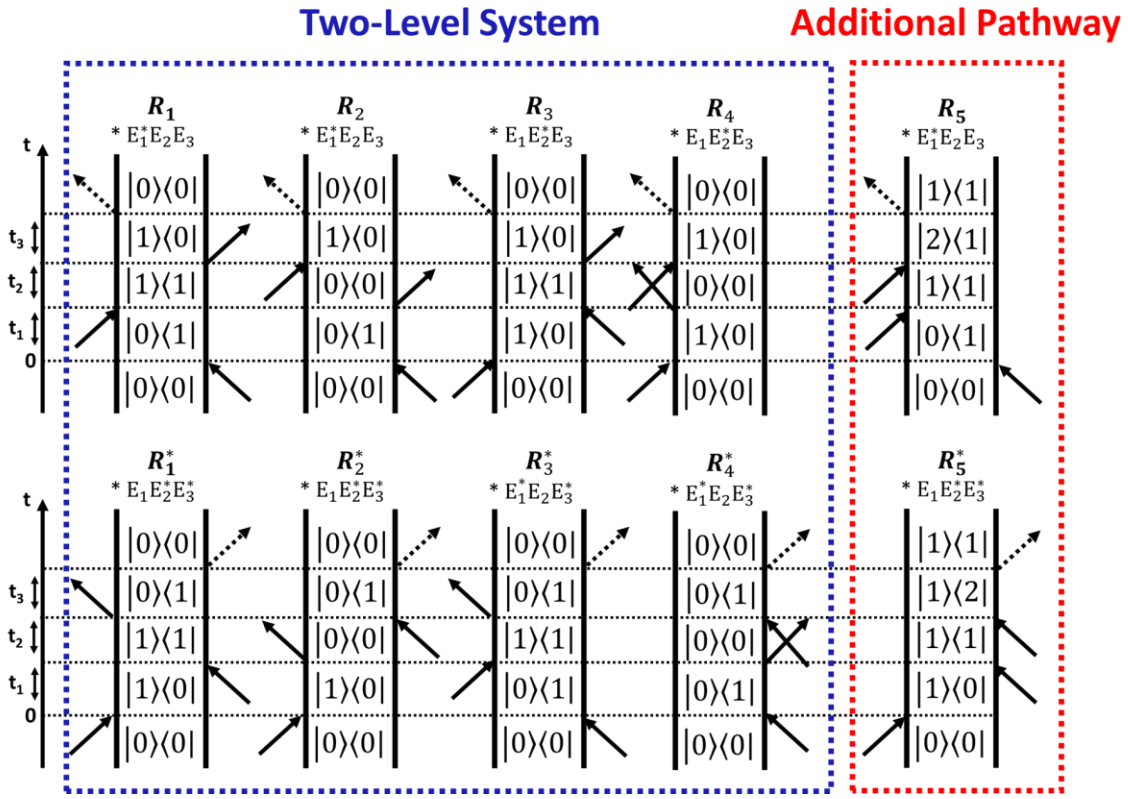

Figure 1.8 ***Double sided Feynman diagrams of the third order response.*** *There are eight different pathways in the third order polarization signals that survived the RWA in a two-level system. An additional pathway which requires a third level is also shown*

1.2 Nonlinear Spectroscopy with Attosecond XUV Pulse

In the previous section, the basic concept of nonlinear spectroscopy has been introduced. While there are many different variants of nonlinear spectroscopy, this dissertation focuses on nonlinear spectroscopy in the extreme ultraviolet (XUV) region. This section covers the knowledge of XUV spectroscopy, the generation of attosecond XUV pulses by the process of high harmonic generation (HHG), and the description of attosecond four-wave mixing (FWM) spectroscopy.

1.2.1 Introduction to the XUV Spectroscopy

XUV is a specific region within the electromagnetic spectrum. While the range of XUV is sometimes vague, it is commonly defined as electromagnetic radiation with wavelength from approximately 10 to 124 nanometers (nm), which corresponds to photons with energy from about 124 to 10 electron volts (eV).

Extension of nonlinear spectroscopy using short wavelengths, such as XUV, offers several advantages over using traditional optical pulses in the UV/Vis or IR region, and it has attracted significant interest [30-35]. The first advantage is that XUV can support shorter temporal durations. The duration of the pulse is limited by the period of an oscillation, and while the near-infrared (NIR) light at 800 nm has a period of 2.6 femtosecond (fs, 10^{-15} s), the optical period for XUV pulse at 100 eV is only 41 attosecond (as, 10^{-18} s). XUV pulses can thus achieve a much shorter temporal resolution, allowing for measurements of much shorter events, such as electron motion. Secondly, the spatial resolution of imaging techniques, such as microscopy, is usually limited by the Rayleigh criterion and is linearly proportional to the wavelength. XUV, with a shorter wavelength, can thus achieve a better spatial resolution than traditional optical pulses. Additionally, XUV can excite atoms or molecules to their inner valence excited states or even core-excited states. These states usually have distinct energies for different elements, allowing for local element-specific probing in a chemical environment.

The XUV excited states are usually at an energy above the ionization potential and can thus undergo autoionization decay [11,14,16,18]. The dynamics of autoionization has attracted great interest since it is one of the simplest examples of multi-electron dynamics. However, lifetimes determined by linewidth measurements in the frequency domain may not be optimal due to the extra spectral complexity in the autoionizing states. Interference between the discrete and continuum states could occur in autoionizing states, resulting in a characteristic asymmetric line shape called a Fano profile in the spectrum [36]:

$$\sigma_{Fano}(E) = \sigma_0 \frac{(q+\varepsilon)^2}{1+\varepsilon^2} \tag{1.45}$$

where $\sigma_{Fano}(E)$ is the absorption cross section of a Fano profile as a function of photon energy (E), σ_0 is the cross section far away from the resonance and q is the Fano parameter that relates to the coupling strength between discrete and continuum states. In Equation (1.45), a reduced energy ε is used and it is defined as

$$\varepsilon = \frac{(E-E_0)}{\hbar(\Gamma/2)} \tag{1.46}$$

where E_0 is the resonance energy of the discrete autoionizing states, and Γ is the natural spectral linewidths, which can be related to the lifetimes of the states. The spectrum shape of Fano profiles with different q are illustrated in Figure (1.9a). The additional parameters of q increase the uncertainty in determining Γ and thus the corresponding lifetime. Meanwhile, as the lifetime in the XUV excited states are usually short, the spectral linewidths of the states are broad. This increases the possibility of spectrum overlaps between multiple states with close resonance energy. A XUV absorption spectrum of O_2 around 20-25 eV is plotted in Figure (1.9b). Most of the features shown in this spectrum are complex, and it is difficult to determine the linewidth for each individual state. Broadening due to multiple vibrational and rotational states causes further problems with linewidth determinations. Direct measurements in the time domain are thus needed to

determine the lifetimes in these autoionizing states, and this can be achieved with nonlinear spectroscopy.

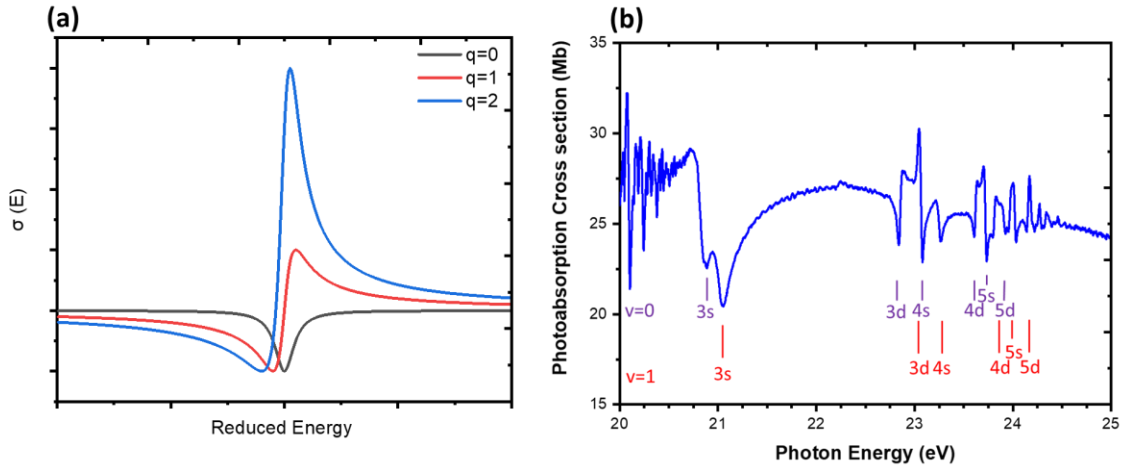

Figure 1.9 ***Absorption Features in the XUV spectrum.*** *(a) The Fano profile as a function of reduced energy is plotted with different Fano parameters q=0, q=1, and q=2 (b) XUV absorption spectrum of O_2 molecule is plotted in the photon energy of 20 to 25 eV*

1.2.2 Generation of Attosecond XUV Pulses through HHG

To extend nonlinear spectroscopy to the XUV region, a reliable source of a strong and short coherent XUV pulses is needed. One of the methods to produce the brightest coherent XUV pulse is through a free electron laser (FEL) [37-39]. However, FELs are only available in costly large facilities and are not easily accessible. A less expensive method, High Harmonic Generation (HHG), is one of the most common methods to generate short XUV pulse in a tabletop setup [4,5,37,39-43].

HHG is a process that converts low-energy photons to much-higher energy photons through a highly nonlinear interaction with a medium. In most of the applications, it can easily upconvert a NIR pulse with a photon energy of 1.5 eV to a broadband XUV pulse covering a range of photo energies from 10 to 100 eV. This is achieved by focusing a strong NIR field into a nonlinear medium, usually a rare gas. The mechanism of generating XUV pulses through this process is commonly interpretated in a semiclassical three-step model [5,37,39,40]. The three steps are tunnel ionization of a electron, propagation of the electron driven by the laser field, and recombination of the electron with the parent ion as illustrated in the Figure 1.10.

The electric field of the driving laser at the focus is usually in the order of magnitude of 10^{14}-10^{15} W/cm^2, which is comparable with the Coulombic potential between an electron and a nuclear in an atom. The total effective potential $V(r,t)$ of the system under the influence of external electric field could be expressed as:

$$V(r,t) = -\frac{e^2}{4\pi\varepsilon_0 r} + eE(t)r \tag{1.47}$$

where $E(t)$ represents the electric field of driving laser. In this equation, the first term on the right-hand side represents the Coulombic potential of the system, and the second term represents the potential induced by the external field. Both terms as well as the total potential are plotted in Figure 1.10(a). It is shown that the total potential is highly distorted

from the columbic potential and has a much lower barrier for the bound electron. This has allowed for the increased probability of tunneling ionization, which is the first step of HHG.

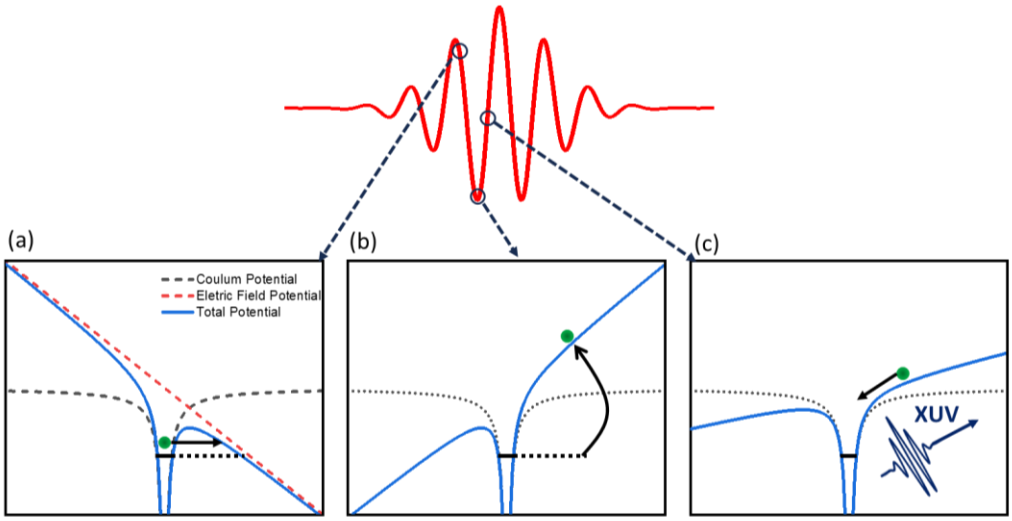

Figure 1.10 ***A schematic of semiclassical three-step model of high harmonic generation (HHG).*** *On the top of the figure, the driving electric field of incident light is plotted in a red line. The system experiences different potentials with the propagation of the driving field. The three steps occur at different phases of the driving field, which include (a) tunneling ionization, (b) propagation, and (c) recombination. An XUV photon is emitted at the end of the recombination. This figure is inspired by ref [5,40].*

Once the electron tunnels through the potential barrier, it becomes a free electron. The second step, propagation, describes the movement of this free electron, and it's fully governed by the driving field. After the electron escaped the barrier, it'll first be accelerated by the driving field and move away from the parent ion. Since the driving field is oscillating, as the time evolves, the sign of the electric field will change, and it start to pull the electron back toward the parent ion. During this process, electron will gain kinetic energy from the driving field.

Eventually, the electron will recollide with the parent ion and recombine with it. During this third step, a small fraction of the time, energy will be released and emitted in the form of a photon. The energy of the photon will be the sum of the kinetic energy gained in the field (KE) and ionization potential (IP) of the atom used for HHG:

$$E_{photon} = \hbar\omega_{photn} = KE + IP \tag{1.48}$$

The kinetic energy can be calculated if we know the phase of driving field at the time of the tunneling ionization. The maximum available kinetic energy happens when the phase of the field is approximately 18° and the maximum energy could be expressed with the ponderomotive energy, $U_{p,}$ which is the cycle-averaged quiver energy of a free electron in the field[37,39]:

$$U_p = \hbar\omega_{photn} = \frac{e^2 {E_0}^2}{4m_e {\omega_0}^2} \tag{1.49}$$

$$E_{photon}^{max} = IP + 3.17U_p \tag{1.50}$$

Here, E_0 represents the peak strength of the driving field, m_e represent the mass of the electron and ω_0 is the frequency of the driving field. With intensity of a NIR driving field at 10^{14}-10^{15} W/cm^2, the emitted photon's energy should fall within the XUV energy region. Also, the pulse emitted in the HHG process is much shorter than the optical period of the driving field and it is typically in the attosecond region.

It is noteworthy that the described HHG process can happen every half-cycle of the driving field. Without proper control, HHG usually yields an attosecond pulse train as shown Figure 1.11 (a) [41,42]. The Fourier transform of an attosecond pulse train yields a HHG spectrum that only contains odd-order harmonics. The shape of a typical HHG spectrum is illustrated in Figure 1.11 (b). Besides the fact that only odd harmonics can be observed, there is another distinctive feature in a typical HHG spectrum. That is, the HHG spectrum could usually be divided into three different regions [37]. In the so-called perturbative region and cut-off region, the harmonic intensity decreases dramatically with the harmonic order, and a plateau region can be found between the two regions. In the plateau region, the harmonic intensities of different harmonic orders are roughly equal.

While an attosecond pulse train has its useful applications, studying dynamics on sub-fs to few-fs timescales requires an isolated attosecond pulse (IAP). The IAP also serves as a better light source for performing nonlinear spectroscopy, as the dipole operator can be better defined. The generation of IAPs can be achieved with proper temporal gating methods [43]. Various gating methods have been demonstrated, including amplitude gating, ionization gating, polarization gating, and double optical gating. Amplitude gating is one of the simplest gating methods and is used for all the experiments performed in this dissertation.

The concept behind amplitude gating is that a specific threshold of the driving field is required to initiate the HHG process and produce attosecond XUV photons. By shortening the pulse duration of the driving field, a condition can be created where only the most intense half-cycle of the driving laser pulse exceeds that threshold, resulting in the generation of an IAP. Controlling carrier-envelope phase (CEP) of the driving pulse is crucial in the amplitude gating. As shown in Figure 1.12, IAPs are predominantly generated only when CEP=0. Also, for amplitude gating, it is easier to get IAPs at the cutoff region as it will require the higher threshold and hence better gating selectivity.

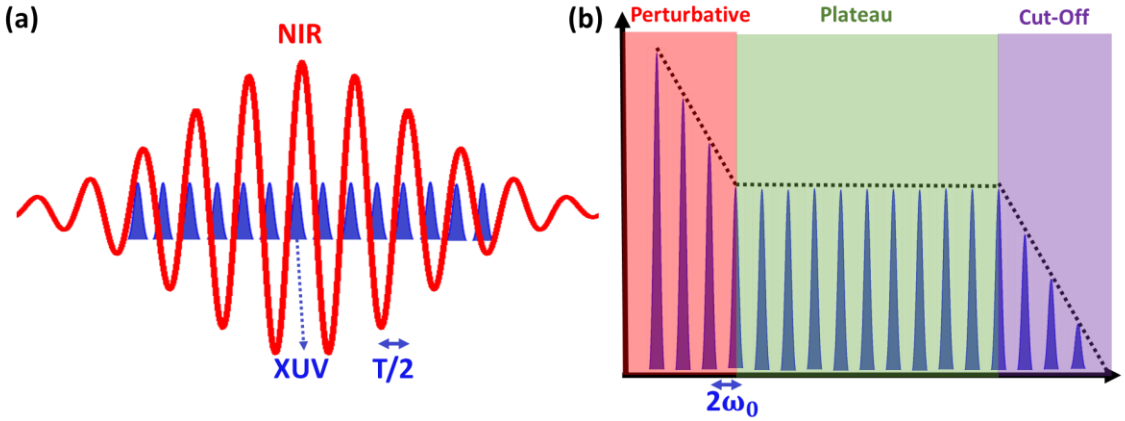

Figure 1.11 ***An attosecond pulse train and its related HHG spectrum.*** *(a) Attosecond pulses are generated every half-cycle of the driving filed, resulting in an attosecond pulse train. (b) The corresponding HHG spectrum only contains odd harmonics and can be divided into three different regions: perturbative region, plateau region, and cut-off region.*

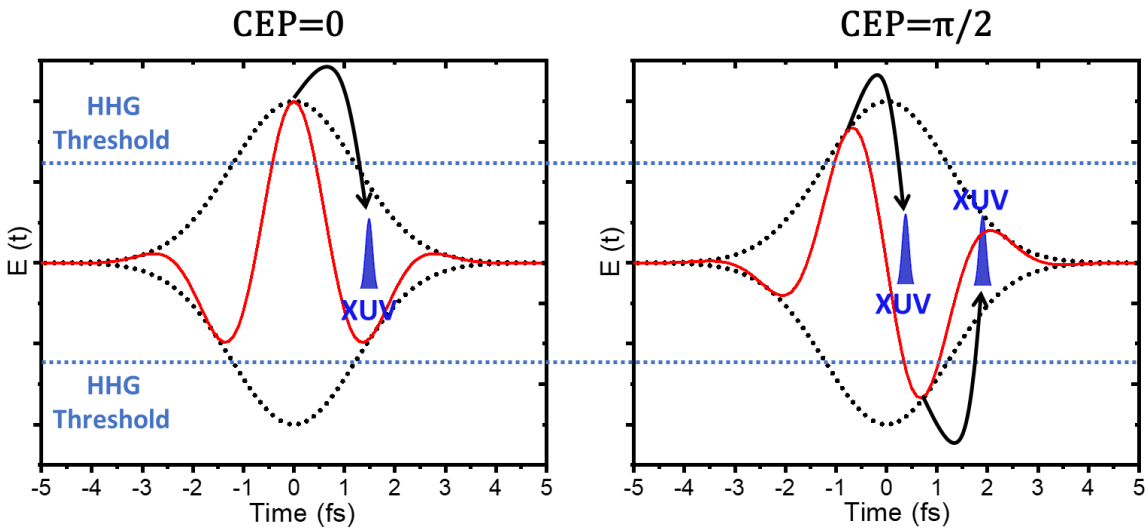

Figure 1.12 ***CEP effect on generating isolated attosecond pulses.*** *The electric field as well as the carrier envelope of 4.5 fs pulses (~2 cycle in 800 nm) are plotted for both CEP=0 and CEP=π/2 cases. A blue dashed line represents the threshold to generate HHG photons. In the CEP=0 case, only the strongest half cycle exceeds the threshold and generates an isolated attosecond pulse. In CEP=π/2 case, there are two equally strong half-cycles, and both generate attosecond pulses.*

1.2.3 Attosecond Four Wave Mixing Spectroscopy

Attosecond pulses produced by HHG can be utilized to perform nonlinear spectroscopy in the XUV region. It is challenging to generate nonlinear signals with XUV pulses alone, as the XUV pulse energies from HHG are quite low, typically on the order of nJ or pJ. However, nonlinear signals can be generated by incorporating them with other optical pulses with longer wavelength, such as NIR pulses. This forms the basis of so-called attosecond four wave mixing (FWM) spectroscopy.

As illustrated in Figure 1.13, attosecond FWM spectroscopy utilizes a short attosecond XUV pulse produced by HHG and two few-cycle NIR pulses to generate third-order polarization signals, or FWM signals. The two NIR pulses are noncollinear and in a crossbeam geometry with respect to XUV pulse, allowing spatially isolation of FWM signals from the incident XUV due to the phase matching condition. The delay for each pulse is properly controlled to perform time-domain measurements of ultrafast dynamics.

To better interpret the information provided by attosecond FWM spectroscopy, an understanding of the pathways involved in the generation of third order polarization is needed. For the scope described in this dissertation, the XUV pulse can excite an electron from its inner valence or core level to a Rydberg state. NIR, on the other hand, can couple with Rydberg electrons but not with the ground state molecules. As a result, the XUV must interact with the system first to generate polarization in the Rydberg states, and the NIR that follows can only interact on the same side of the Feynman diagram to resonant with Rydberg states. This provides that all the pathways discussed in this dissertation are $R_4 + R_4^*$ terms in Equation (1.43).

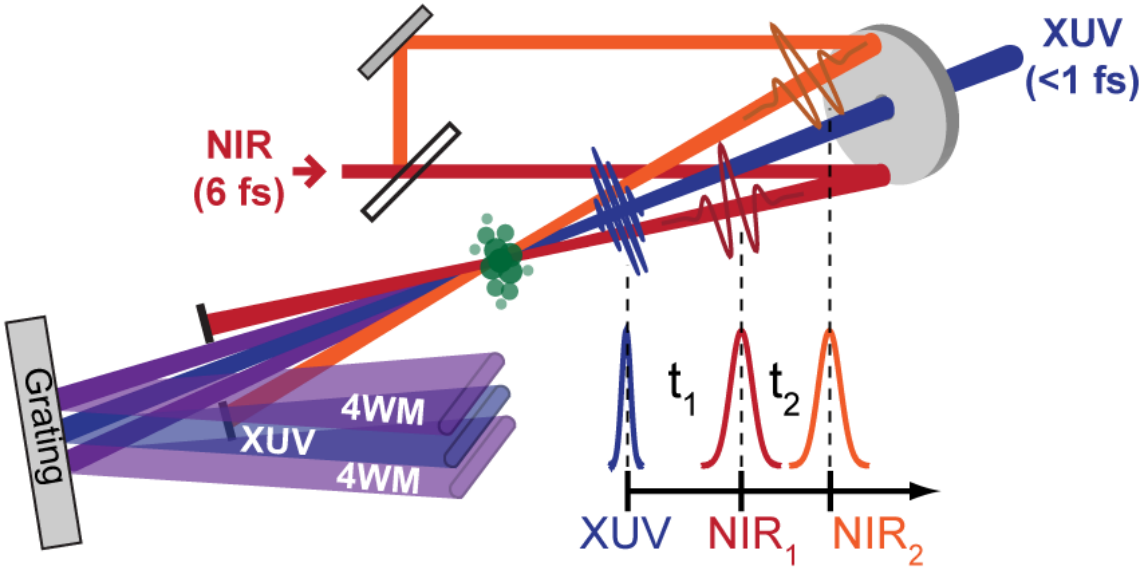

Figure 1.13 ***Scheme of attosecond FWM spectroscopy.*** *An attosecond XUV pulse and two noncollinear NIR pulses are utilized to generate spatially isolated FWM signals. The delay for each pulse is controlled properly.*

A further consideration of the wavevector and different states involved in the pathways yields three different categories of the pathways: Λ-type coupling, V-type coupling, and ladder-type coupling, as shown in Figure 1.14. The ladder-type coupling can further be divided into two sub-categories: ladder up and ladder down. All these pathways involve the same interaction as they are all corresponding to R_4 terms: after the XUV pulse excites the polarization in a one-photon allowed bright state, two NIR pulses interact with the system to generate third-order polarization in the same or different bright state through the coupling with a one-photon forbidden dark state. The pathways involving the other side of the Feynman diagram, R_4^*, are also allowed but not shown here, and they are just the complex conjugate of R_4 pathways.

Since the wavevector involved in different categories of the pathways are different, they can be disentangled easily with proper experiment design. Ladder-type coupling and Λ or V-type coupling can be separated by setting the angle of two NIR pulses differently, which will be discussed in Chapter 3. Separation between Λ-type coupling and V-type coupling can be achieved when one NIR pulse is properly delayed with the other [15,18].

There could still be many pathways in the same categories depending on the number of the states involved in the FWM process. For example, two V-type pathways involving two different initially XUV excited states can exist, and they can emit the polarization from the same final state, as shown in Figure 1.15 (a). These pathways can not be separated easily as they carry the same wavevector and frequency information. Without separation, the different pathways will interference with each other, resulting in an oscillation in the FWM signals at the frequency of the energy difference between the different excited states involved, also known as quantum beating. This is illustrated in Figure 1.15 (b). To deal with this, a pulse shaper can be implemented to further separate the pathways through multidimensional spectroscopy [10]. Additionally, a global fit can be done to interpret the data with these oscillations if the energy of each state is well known, which will be discussed in the Chapter 5.

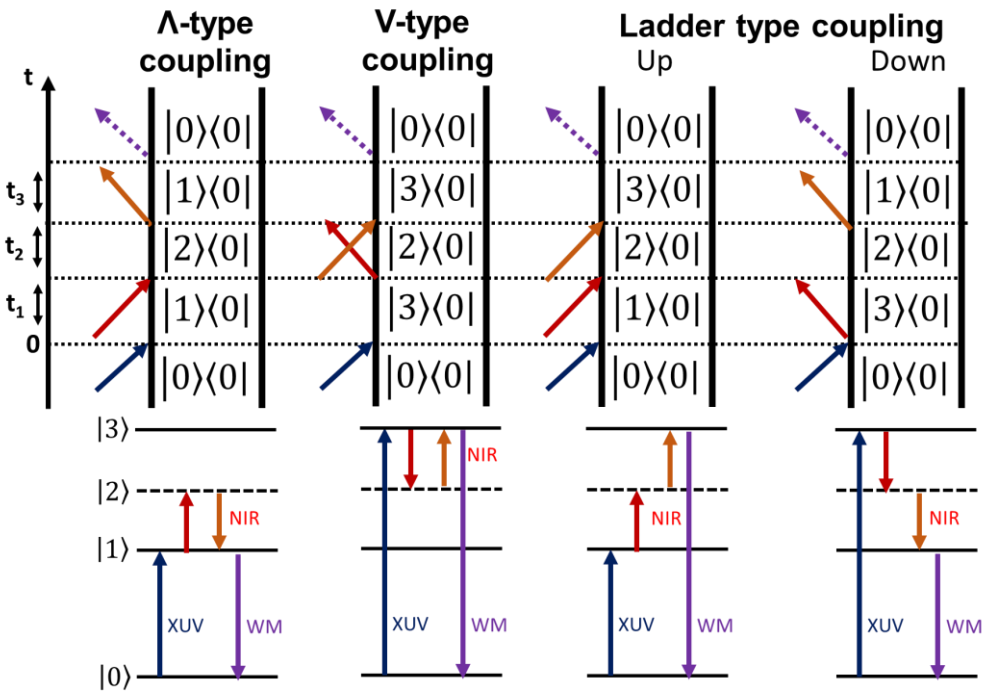

Figure 1.14 ***Different categories of the pathways involved in the attosecond FWM spectroscopy.*** *There are three different categories of the pathways: Λ-type coupling, V-type coupling, and ladder-type coupling. All of them involving a XUV pulse to generate polarize at an initially bright state, followed by two NIR pulses coupling with dark state to generate third-order polarization in a final bright state. However, they involve different set of the wavevector combinations of the incident fields.*

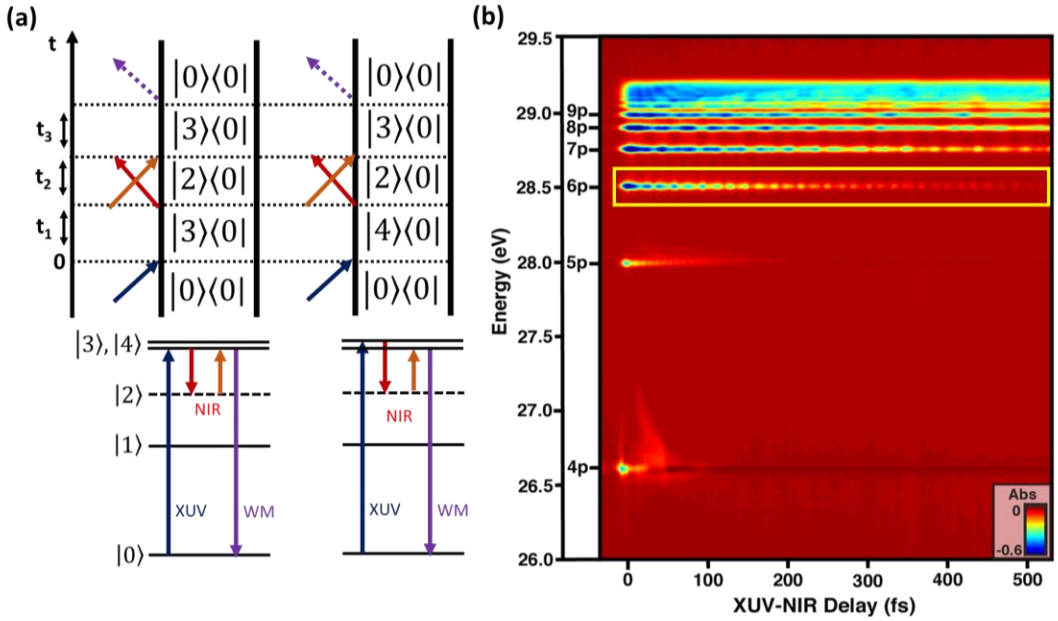

Figure 1.15 ***Interference of different pathways.*** *(a) Two different V-type coupling pathways with the same final bright state but different initial bright states are showing. (b) The interference between pathways will result in quantum beating in the FWM signals as shown in the yellow bracket.*

After distinguishing different pathways, the last important piece for the FWM spectroscopy is the design of the pulse sequence. Different pulse sequences can lead to measurements of different dynamics. Recall that all the FWM pathways described in this dissertation are R_4 terms, and the time-dependent emitted field can be expressed as

$$E_{Emit}(t_1, t_2) \propto iR_4(t_1, t_2) \propto e^{-t_1/T_2^{(b)}} e^{-t_2/T_2^{(d)}} \tag{1.51}$$

Here, $T_2^{(b)}$ and $T_2^{(d)}$ are the dephasing times of the initially bright state and dark state involved in the pathway, respectively. t_1 represents the delay between first NIR and XUV pulse, while t_2 represents the delay between two NIR pulses. In Equation (1.51), we neglect the oscillating terms as they are too fast to be captured by the detectors. Since detectors are square-law detectors, the time-dependent FWM signals can be expressed as

$$I_{FWM}(t_1, t_2) \propto E_{Emit}(t_1, t_2)^2 \propto e^{-t_1/T_1^{(b)}} e^{-t_2/T_1^{(d)}} \tag{1.52}$$

Here, $T_1^{(b)}$ and $T_1^{(d)}$ are the population lifetimes of the initially bright state and dark state involved in the pathway, respectively. We use Equation (1.17) to relate T_1 and T_2. Equation (1.52) suggests two of the simplest pulse sequences in the FWM spectroscopy: bright state scan and dark state scan. They are both illustrated in Figure 1.16.

In a bright state scan, two NIR pulses are time-coincident with a delay t_1 with respect to the XUV pulse. By recording the FWM signals as a function of t_1, the population lifetime of a bright state can be obtained. Alternatively, in the dark state scan, the first NIR pulse is time-coincident with XUV pulse, while the second NIR pulse is delayed by t_2. By recording the FWM signals as a function of t_2, the population lifetime of a dark state can be obtained.

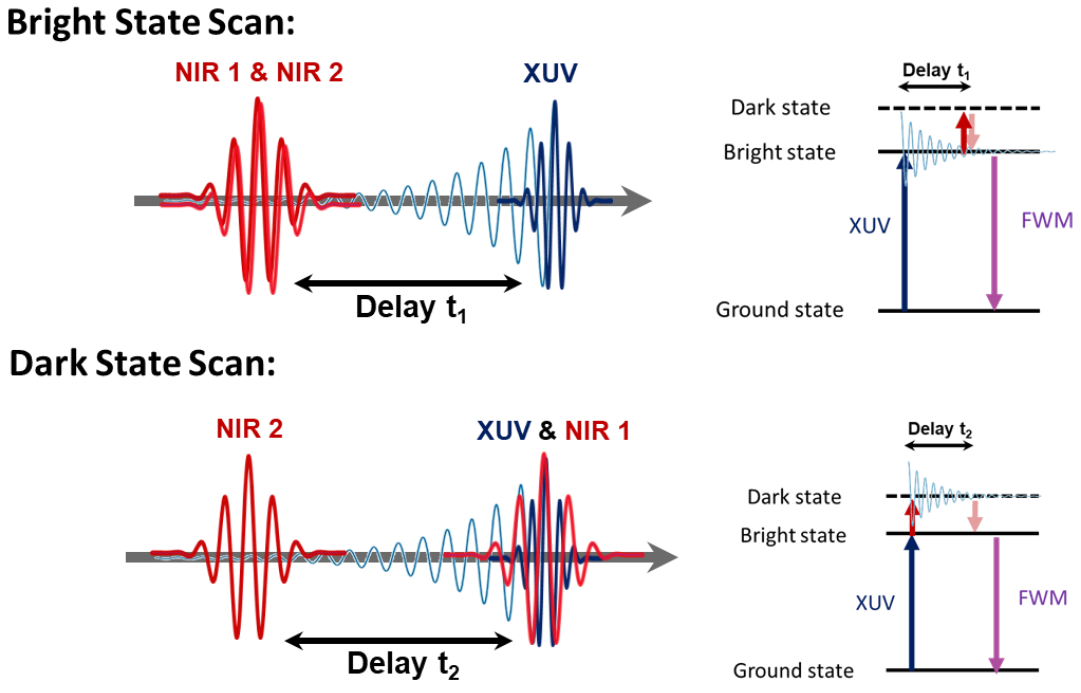

Figure 1.16 ***Pulse sequence of two different scans.*** *In bright state scan, two NIR pulses are time-coincident with a delay t_1 with respect to the XUV pulse. In the dark state scan, NIR2 pulse is delayed by t_2 with respect to time-coincident XUV and NIR1 pulses.*

1.3 Outlook

The mission of this project is to develop nonlinear spectroscopy in the XUV or even X-ray region. This was firstly approached by our table-top attosecond FWM spectroscopy. Prior to 2020, several FWM experiments had been conducted to monitor electronic and vibronic coherences [6,7], determine the vibrational structure of molecules [8,9], and measure the autoionization lifetime in an atom [11]. Other applications such as transient grating, multidimensional spectroscopy, and heterodyne detection had also been demonstrated [10,12,13]. The work detailed in this dissertation has taken the applications of attosecond FWM spectroscopy one step further.

In Chapter 3, the first experiment to investigate the ultrafast decaying states in a molecule is performed with attosecond FWM spectroscopy, revealing an intriguing picture of the coupled nuclear– electronic dynamics in O_2 inner valence excited states. In Chapter 4, FWM is further applied to CO_2 to produce meaningful measurements of ultrafast dynamics in polyatomic systems. In Chapter 5, coherent wave packet dynamics is studied in Ar, highlighting the role of non-resonant NIR interactions in attosecond FWM spectroscopy. With implementation a new, more powerful laser system, the attosecond FWM spectroscopy apparatus has been reconstructed and now has the ability to produce XUV flux at higher photon energy. In Chapter 6, some preliminary data in Xe demonstrate the first measurements of Auger decay in the core-excited state with the new apparatus.

The short-term future goal for the project is to generate HHG pulses in the soft X-ray region, specifically carbon K-edge around 300 eV. Proper modification of the experimental apparatus needed for this purpose is described in Chapter 6. Attosecond FWM spectroscopy at carbon K-edge will permit the work on core-excited states of chemically and biologically significant organic molecules. Ultimately, the method of attosecond FWM spectroscopy will pave the way for future studies and applications of nonlinear spectroscopy in XUV and soft x-ray regions, leading to an ambitious goal of multidimensional spectroscopy with multiple attosecond XUV and/or SXR light pulses.

Chapter 2: Experimental Apparatus

2.1 Overview

A general scheme of the attosecond FWM apparatus is illustrated in Figure 2.1. In brief, the output a commercial Ti:Sapphire femtosecond laser system is spectrally broadened through self-phase modulation (SPM) in a hollow core fiber and recompressed using a set of chirped mirrors to generate few-cycle NIR pulses. The few-cycle NIR pulses are split, and part of the beam is used to drive HHG to produce attosecond XUV pulses in the homebuilt vacuum chambers. The other part of the NIR pulses is further split into two different arms. Both arms are delayed before recombining and intersecting with XUV pulses at the target sample cell in a noncollinear crossbeam geometry. The interaction between the three beams generates nonlinear FWM signals in the XUV region, which are detected by a XUV spectrometer consisting of a grating and CCD camera. The attosecond FWM apparatus can be divided into three major components: few-cycle NIR pulses, homebuilt vacuum chambers, and nonlinear FWM signal generation. Each of them will be discussed in detail in separate sections.

The apparatus in this project was redesigned in 2021 to accommodate the installation of a new high-power laser system. The apparatus prior to that is referred to as the "old apparatus" and the newly built apparatus is referred to as the "new apparatus" for the rest of this chapter. While most of the experiments detailed in this dissertation, including those in Chapters 3, 4, and 5, were performed with the old apparatus, that instrument has already been thoroughly described in other dissertations [44,45]. On the other hand, the new apparatus has not been extensively detailed before and the objective of this chapter is to provide a guide to the new apparatus for future successors to this project. The actual layouts of both old apparatus and new apparatus are illustrated in Figure 2.2.

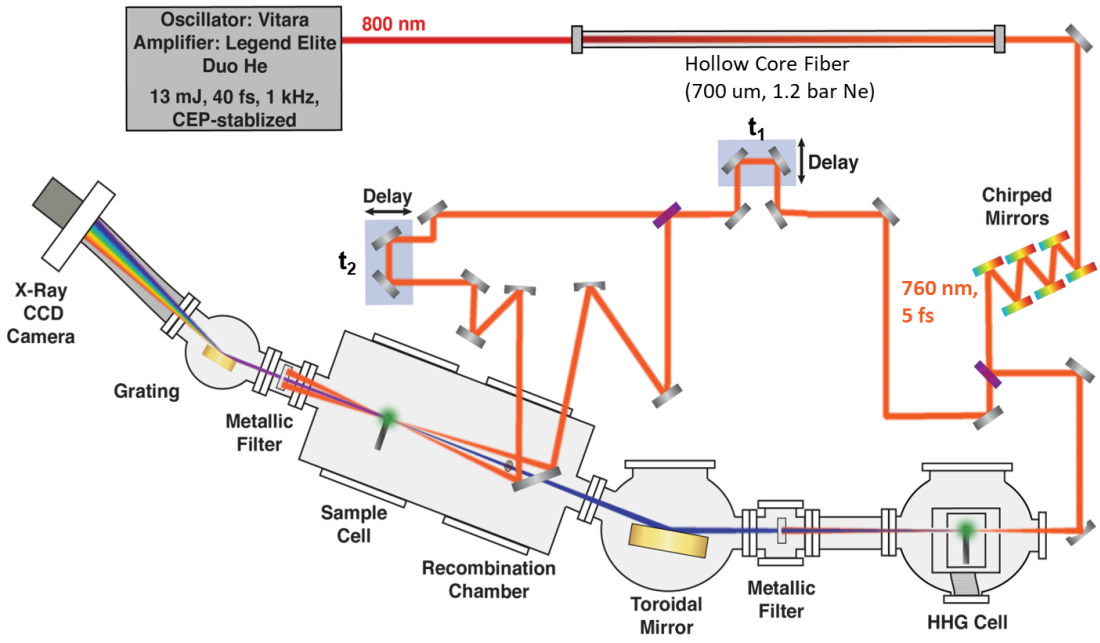

Figure 2.1 ***Scheme of the new attosecond FWM apparatus.*** *The detailed description is provided in the main text.*

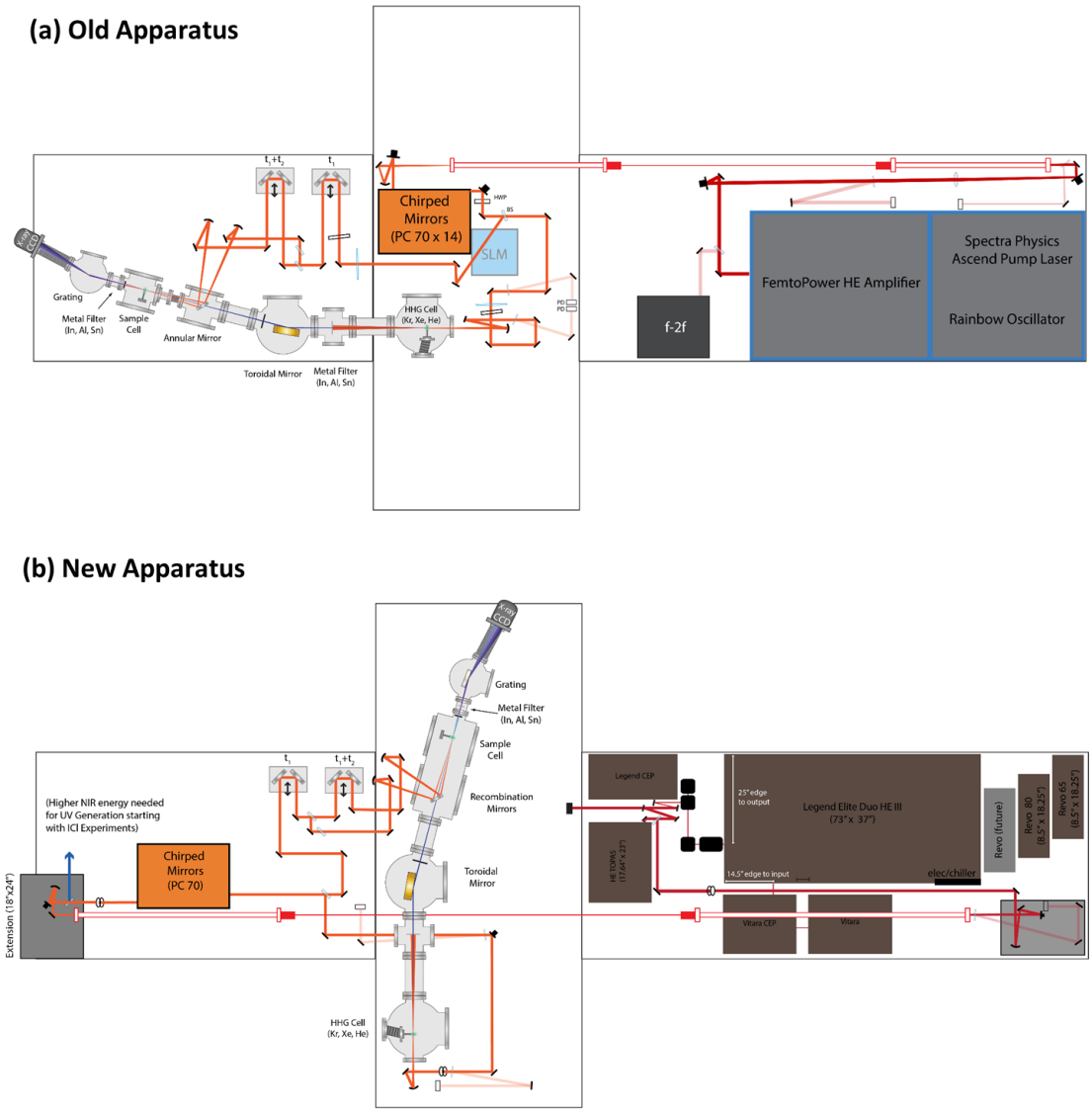

Figure 2.2 ***Actual layouts of the experimental apparatuses.*** *(a) old apparatus (b) new apparatus. The major differences between the two are discussed in Table 2.1*

There are three major differences between old apparatus and new apparatus: laser system, HHG Chamber, and recombination chamber. The detailed comparison is shown in Table 2.1. All the changes incorporated into the new apparatus are aimed to favor the FWM experiments at higher photon energy.

Apparatus	**Laser System**	**HHG Chamber**	**Recombination Chamber**
Old apparatus	**FemtoPower** 2 mJ, 22 fs, 1 khz	12” Chamber with 2000 l/s turbo	Separate from sample chamber
New apparatus	**Legend Elite Duo HE+** 13 mJ, 40 fs, 1 khz	16” Chamber with 3000 l/s turbo	Integrate with sample chamber

Table 2.1 ***Comparison between old apparatus and new apparatus.***

2.2 Generating Few-Cycle NIR Pulses

2.2.1 Background

Few-cycle NIR Pulses are needed to generate IAPs, as described in Chapter 1, and achieve better temporal resolution. To generate few-cycle NIR pulses, the intrinsic relationship between the pulse duration and spectral bandwidth needs to be considered. An ideal Gaussian pulse can be expressed in either the time domain or frequency domain as:

$$E(t) = E_0 e^{-2ln2(\frac{t}{\tau})^2} e^{i(\omega_0 t + \phi(t))} \tag{2.1}$$

$$E(\omega) = A_0 e^{-2ln2(\frac{\omega-\omega_0}{\Delta\omega})^2} e^{i\phi(\omega)} \tag{2.2}$$

where E_0 and A_0 are peak heights in the time domain and frequency domain, respectively, τ is the pulse duration, $\Delta\omega$ is the spectral bandwidth, ω_0 is the carrier frequency, and $\phi(t)$ and $\phi(\omega)$ are the phase of the field in the time domain and frequency domain, respectively. Since the expression of the field in the time domain and frequency domain are the Fourier transform of each other, the uncertainty relationship between τ and $\Delta\omega$ is obtained:

$$\tau(as) * \Delta\omega(eV) \geq \hbar(4ln2) = 1825 \tag{2.3}$$

Thus, to generate NIR pulses with a pulse duration shorter than 5 fs, as typically used in the experiments in this dissertation, a minimum spectral bandwidth of 0.4 eV is needed. This bandwidth exceeds the usual output bandwidth of a commercial laser system. As a result, proper spectral broadening is essential firstly to generate few-cycle NIR pulses.

In Equation (2.3), if the equal sign is satisfied, the pulse is considered a transform-limited pulse. To achieve transform-limited, control of the frequency domain phase $\phi(\omega)$ is needed. $\phi(\omega)$ is often expressed in the Taylor expansion form [46]:

$$\phi(\omega) = \phi_0 + \frac{\partial\phi}{\partial\omega}\Big|_{\omega_0}(\omega-\omega_0) + \frac{1}{2}\frac{\partial^2\phi}{\partial\omega^2}\Big|_{\omega_0}(\omega-\omega_0)^2 + \frac{1}{6}\frac{\partial^3\phi}{\partial\omega^3}\Big|_{\omega_0}(\omega-\omega_0)^3 + \cdots \tag{2.4}$$

Here, the zeroth order phase ϕ_0 corresponds to the CEP and is irrelevant to the pulse envelope itself. The coefficients of each order are referred to as nth-order dispersions. The first-order dispersion $\frac{\partial\phi}{\partial\omega}$, also known as group delay, describes the delay of the pulse envelope itself but has no effect on the shape of pulse envelope. The second-order dispersion $\frac{\partial^2\phi}{\partial\omega^2}$, also known as group delay dispersion (GDD), introduces a frequency-dependent delay in the pulse, or chirp. A pulse is said to be positively chirped if the frequency of the pulse increases over time. The pulse duration will be longer than the transform limit with non-zero GDD, but the pulse shape retains its symmetry. The third-order dispersion (TOD) $\frac{\partial^3\phi}{\partial\omega^3}$ can not only elongate the pulse duration but also lead to asymmetric distortion of a pulse, forming satellite pulses. The effects of different order dispersions on the pulses are illustrated in Figure 2.3.

As depicted in Figure 2.3, to generate short pulses, it is crucial to minimize GDD, TOD and higher order terms. With combining appropriate materials, GDD and TOD are minimized in the experiments performed in this dissertation. Details will be discussed in a later section.

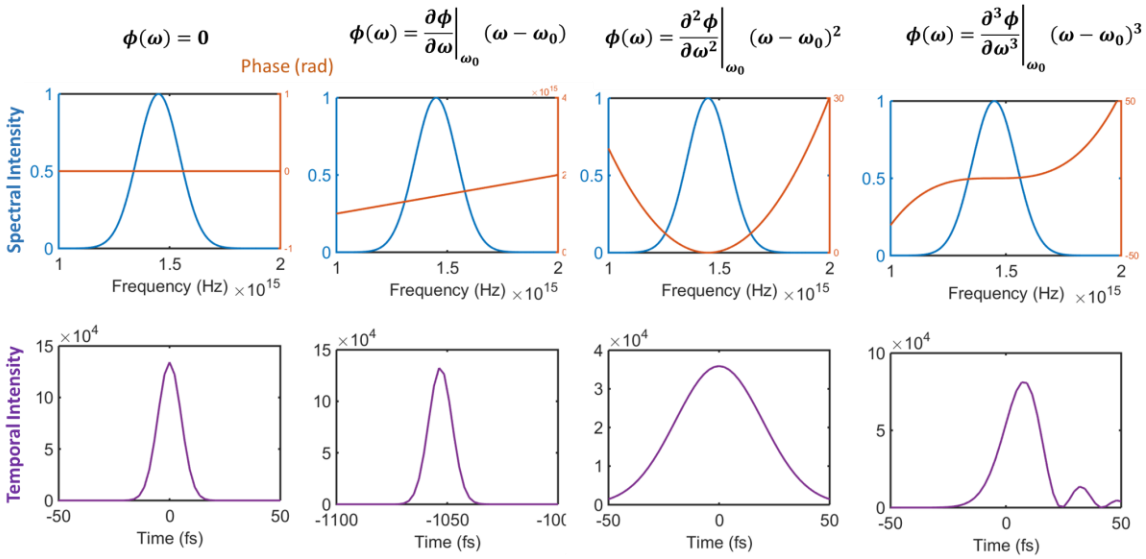

Figure 2.3 ***Effect of the dispersion on the pulse shape.*** *The zeroth order phase and first order dispersion have no effect on the pulse shape. The GDD elongate the pulse but keep it symmetry. The TOD distort the pulse, introducing satellite pulses.*

Overall, to generate few-cycle NIR pulses, the output of the commercial Ti:Sapphire femtosecond laser system needs to be initially broadened to achieve a short transform-limited pulse duration. This can be accomplished through the SPM process with a hollow core fiber filled with nonlinear gas medium. Subsequently, the pulse dispersion needs to be minimized to compress the pulse. This is achieved through a combination of a set of chirped mirrors, fused silica wedges, and an Ammonium Dihydrogen Phosphate (ADP) crystal. In the next few subsections, the laser system, hollow core fiber, and pulse compression will be discussed separately.

2.2.2 Ultrafast Laser System

A layout of the laser system in the new apparatus is shown in Figure 2.4. This laser system consists of four laser units: a Ti:Sapphire oscillator (Vitara-T), two Nd:YLF pump lasers (Revolution-65 and Revolution-80), and a two stage Ti:Sapphire chirped pulse amplifier (Legend Elite Duo HE+). There two additional CEP units to stabilize the CEP of both Vitara-T and Legend Elite Duo HE+. The specification of the laser units is shown in table 2.2. Notably, the breadboard size of Legend Elite Duo HE+ in this lab is larger than the normal version to provide extra space for a potential future upgrade, the addition of an extra amplification step. There is also a reserved space on the optical table for a potential third Revolution pump laser for that purpose as well.

Laser	Type Of laser	Wavelength (nm)	Power	Pulse Energy	Pulse Duration	Repetition Rate
Revolution-65 Pump Laser	Nd:YLF	527	38 W	38 mJ	150 ns	1 kHz
Revolution-80 Pump Laser	Nd:YLF	527	45 W	45 mJ	150 ns	1 kHz
Vitara-T	Ti:Sapphire	740-860	660 mW	5 nJ	<12 fs	80 MHz
Legend Elite Duo HE+	Ti:Sapphire	775-825	13 W	13 mJ	<40 fs	1 kHz

Table 2.2 ***Specification of various laser units in the new apparatus.***

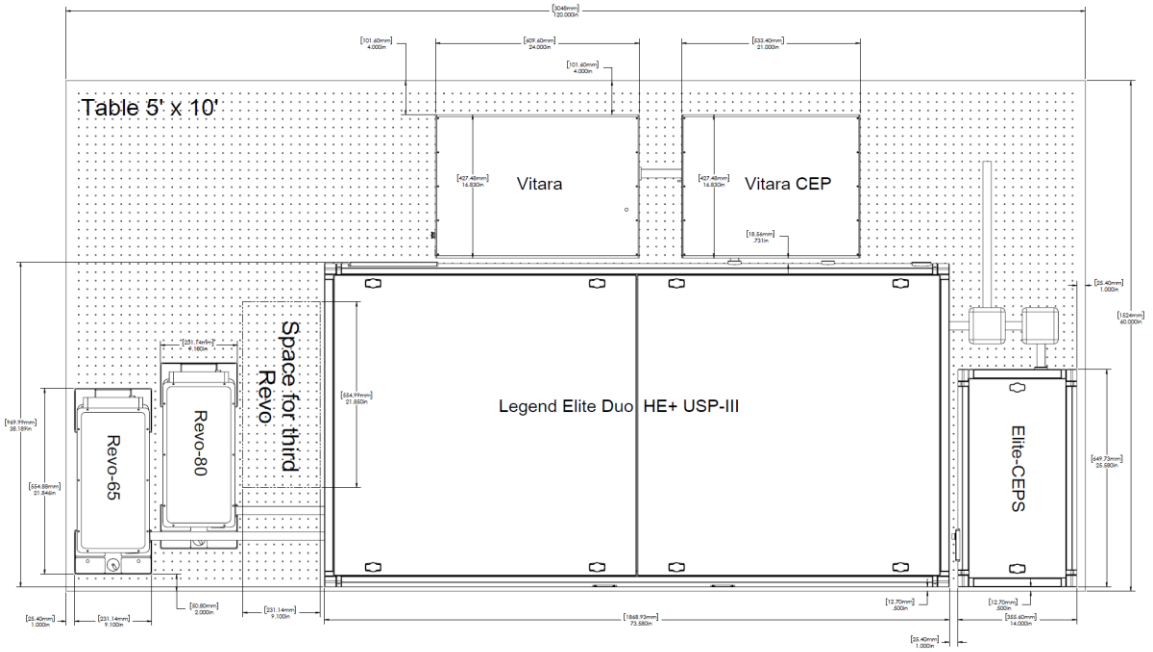

Figure 2.4 ***Layout of the ultrafast laser system in the new apparatus.*** *The laser system consists of several units, which is described in the main text.*

For operation, the Vitara-T produces a CEP-stabilized mode-locked 800 nm laser pulse with 100 nm bandwidth and 600-660 mw power at 80 MHz repetition rate and serves as a seeded pulse for the Legend Elite Duo HE+. There are two stages of amplification in the Legend Elite Duo HE+. The first stage is a regenerative amplifier (RGA), which is pumped by ~32 W output of the Revolution-65, to bring the power of the seed beam up to ~8 W. The second stage is a single pass amplifier (SPA), which is pumped by ~37 W output of the Revolution-80, yielding ~17 W uncompressed light. After passing through the compressor gratings, the resulting output is a 35-40 fs pulse, 12-13 W average power at a 1 kHz repetition rate with approximately 40 nm bandwidth. The power fluctuation of the system is usually around 0.1~0.2% after an hour of warm up.

Unlike the laser system in the old apparatus, the new system is quite stable over time and no daily alignment is needed. Some tweaks on the cavity mirrors, especially in the RGA, may be needed once a while if the build-up profile is not optimal. Figure 2.5 shows an example of an optimal build-up profile where the last two round trips of amplification are roughly equal intensity. If the build-up profile cannot be recovered with the alignment, one should check if the window for the crystal chamber is damaged and replace it. A picture of a damaged window is included in Figure 2.6 (a). The transmission for the Pockel cells may decay over time as well, so if needed the power of the Revolution-65 can be increased over time to compensate for the loss.

If the build-up profile appears satisfactory, but the power of the Legend Elite Duo HE+ is low, adjustments to the SPA cavity mirrors can be considered. However, the alignment of the SPA rarely shifts significantly, and in most cases, the low laser power is attributed to the contamination built on the compressor gratings as shown in Figure 2.6 (b).

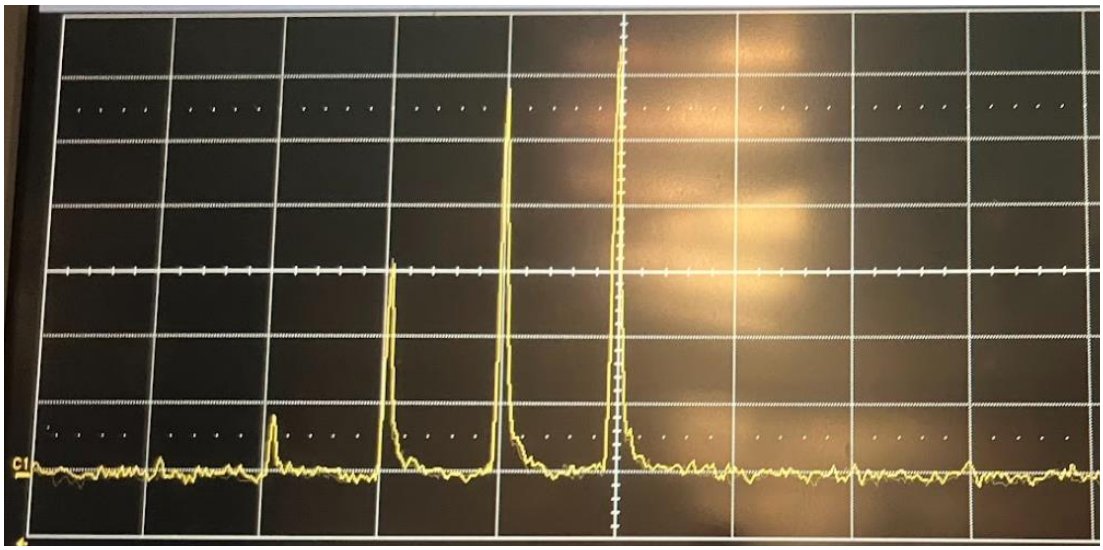

Figure 2.5 ***Optimal build-up profile for RGA.*** *The intensity of the last two round trips should be almost the same.*

With such high laser power on the compressor gratings, combined with contamination, burn spots can occur. It is advised to clean the gratings periodically to increase their lifetime. This can be done by running them under a flow of distilled water and then blowing them with clean N_2 gas to dry. However, even with the cleaning process, the quality of the grating still decays gradually and often needs to be replaced, as much as once a year.

Another critical aspect of laser system maintenance involves the air gas filter in the environmental control unit (ECU). The Ti:Sapphire crystals are cooled to -10 ˚C and sealed in a crystal chamber with a flow of clean dry air. The air flow passes through two filters in the ECU as shown in Figure 2.7 (a). The first filter consists solely of Drierite, which adsorbs water vapor, while the second filter contains both Drierite and molecular sieve to further purify the gas flow. It is essential to replace the first filter approximately every two months, before all the Drierite turns purple. During the replacement process, the flow rate must be carefully monitored by measuring the output voltage of a sensor located on the back side of the ECU, and it should be maintained at around 2.5 V. Failure to do so may lead to ice and water condensation in the crystal chamber, as shown in Figure 2.7 (b). This will severely deteriorate the output of laser beam.

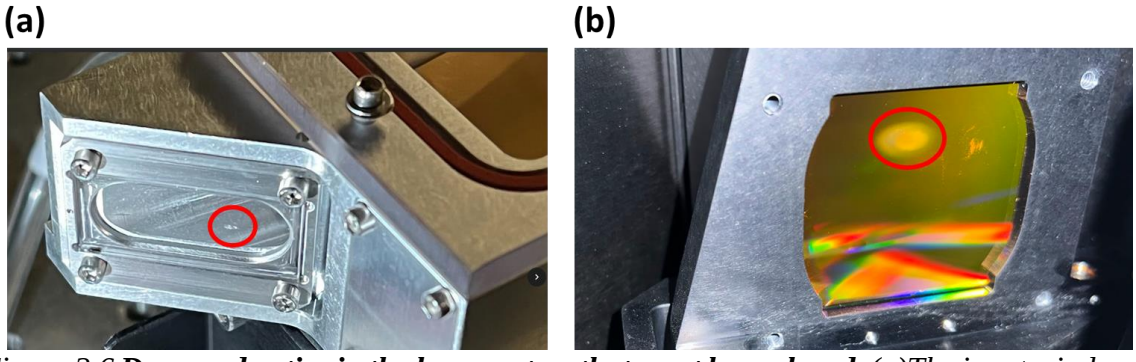

Figure 2.6 ***Damaged optics in the laser system that must be replaced.*** *(a)The input window of the RGA crystal chamber (b) the compressor grating.*

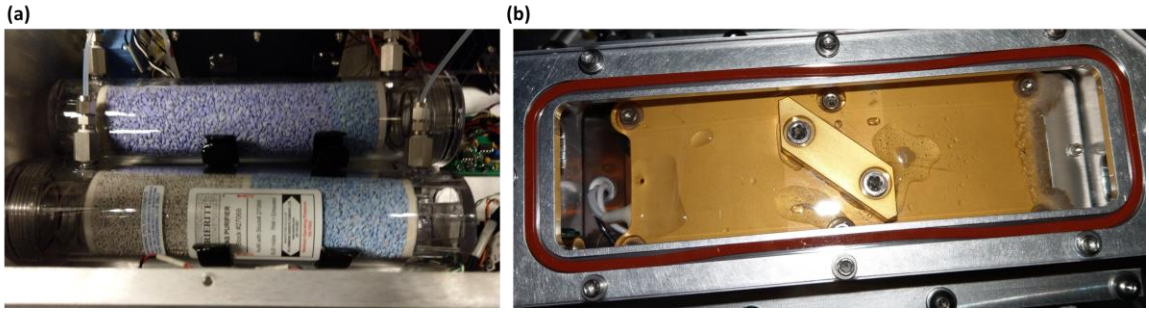

Figure 2.7 ***Maintenance of dry air flow.*** *(a)There are two dry air filters in the ECU. The upper one needs to be replaced before all the Drierite turns purple. (b) Failure to control the dry air will lead to condensations in the crystal chamber.*

2.2.3 Hollow Core Fiber

The output of the Legend Elite Duo HE+ is split, and part of the beam (~3.5-4 mJ) is directed and focused into a stretched hollow core fiber (Few-Cycle Inc.) filled with 1-1.5 bar of Neon gas. The hollow core fiber serves two purposes. Firstly, the laser pulses can undergo SPM process in the neon nonlinear medium to gain enough spectral bandwidth to support few-cycle pulses [46]. Secondly, the waveguide nature of hollow core fiber is utilized to clean the beam mode.

The parameters of the fiber used in both the old apparatus and new apparatus are shown in Table 2.3. The output power of the new apparatus is nearly 2.4 times that of the old apparatus. For the new apparatus, a flexible 3-meter-long fiber with an inner diameter of 700 μm is used. The fiber tips are secured into ceramic capsules and inserted into fiber mounts with protective metal rings, as shown in Figure 2.8. Due to spatial constraints in the lab, the fiber has to pass above the laser box of Vitara-T and under the vacuum chambers, as illustrated in Figure 2.8 (b). To accommodate this, extra metal blocks have been added to elevate the fiber mounts to a height of approximately 8.5 inches. Once the fiber is properly positioned in the fiber mounts, a scroll wheel in the exit mount is used to stretch the fiber, as shown in Figure 2.8 (c). To ensure precise alignment, four alignment pins in both entrance and exit mounts as well as a 2-D translational stage in the entrance mount are utilized to fix and determine the position and tilting of of the fiber, shown in Figure 2.8 (c) and (d). A total of 3.4 meters of vacuum tubes are installed before and after the entrance and exit mounts, connected to both vacuum pump and Ne gas cylinder to adjust the pressure in fiber from 0 to 45 psi of neon.

Apparatus	**Fiber Length (m)**	**Inner Diameter (μm)**	**Focusing optic**	**Input Power (W)**	**Output Power at Vacuum (W /T%)**	**Output Power with Neon Gas (W / T%)**
Old apparatus	2	450	Lens (f = 1.5 m)	1.7	1.2 (70%)	1.1 (65%)
New apparatus	3	700	Mirror (f = 2.5 m)	3.5	2.6 (75%)	2.5 (70%)

Table 2.3 ***Parameters of fiber setup in both old apparatus and new apparatus.***

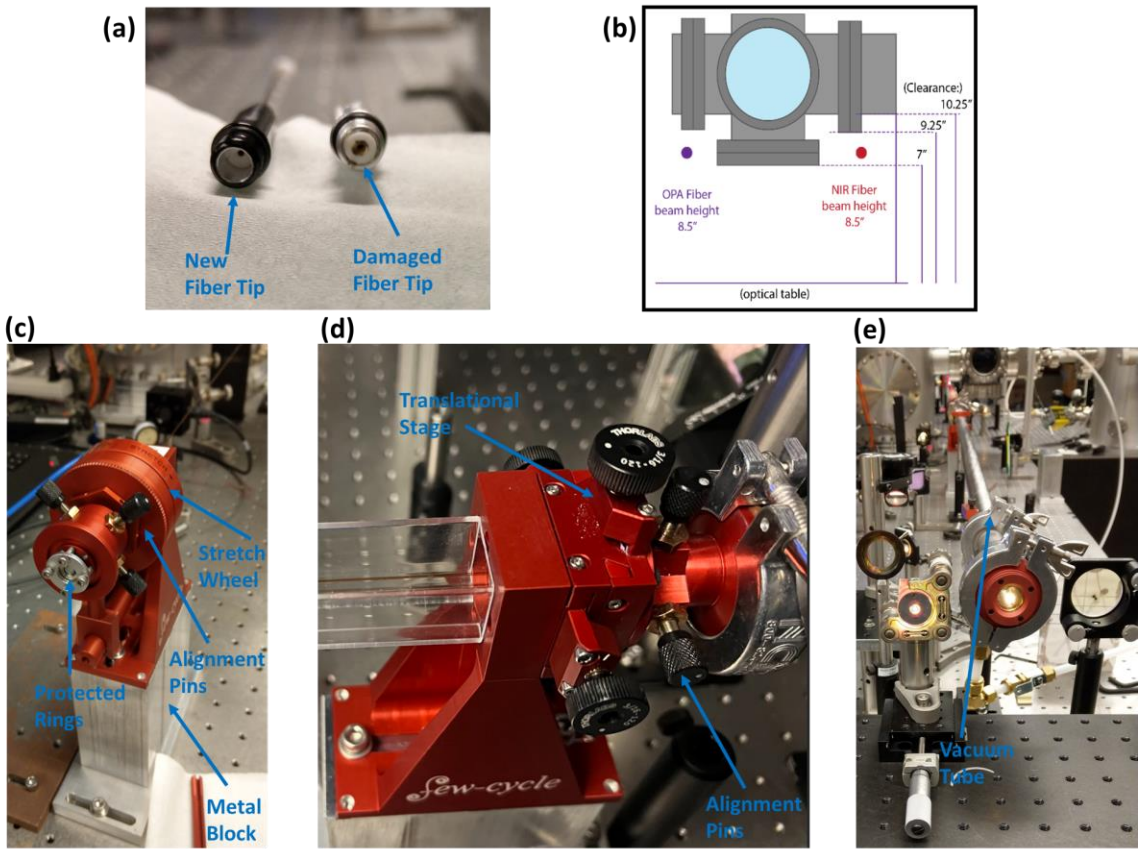

Figure 2.8 ***Assembly of Few-Cycle hollow core fiber system.*** *(a) Fiber tips with ceramic capsules. (b) A schematic illustration of the fiber height (c) Output fiber mount (d) input fiber mount (e) A fully assembled fiber with a vacuum tube.*

To align the fiber, the fiber itself and the vacuum tubes are first removed, and the laser beam is aligned through the apertures of the input and output fiber mounts. The laser beam is focused using an f=2.5m focusing mirror on a translational stage. As shown in Figure 2.9, The beam size at the fiber entrance is measured with a beam profiler and adjusted to be approximately 64% of the fiber diameter (~450 μm) to achieve maximum transmission [47].

Once this step is completed, the fiber and the vacuum tubes are reinstalled, and the translational stage, alignment pins, and the stretcher wheel of the fiber mounts, as those shown in Figure 2.8, are utilized to optimize the fiber's transmission under vacuum. The expected transmission of the fiber under vacuum should be around 75% at a 3.5W input.

Next, neon gas is introduced to the system. During this process, the gas line needs to be flushed several times to achieve the maximum transmission. The translational stage, alignment pins, and the stretch wheel of the fiber mounts are fine tweaked with changes in the neon gas pressure to attain the optimal fiber output.

There are several criteria for an optimal fiber output. Firstly, the transmission needs to be at least 65% to minimize power loss in the fiber. Secondly, the spectral range of the fiber needs to be broad enough to support few-cycle pulses, typically spanning from the blue end of about 550 nm to 950 nm, as shown in Figure 2.10 (a). Lastly, the beam mode needs to be symmetrical and concentrated at the center spot, as shown in Figure 2.10 (b).

Note that if the neon pressure is too high, the spectrum will be over broadened and white light can be observed, as shown in Figure 2.10 (c). This will be bad for the pulse compression in the next step as the chirped mirrors we used only support 500-1050 nm, and thus should be prevented. Typically, a neon gas pressure of about 1-1.5 bar is recommended for a 3.5 W input.

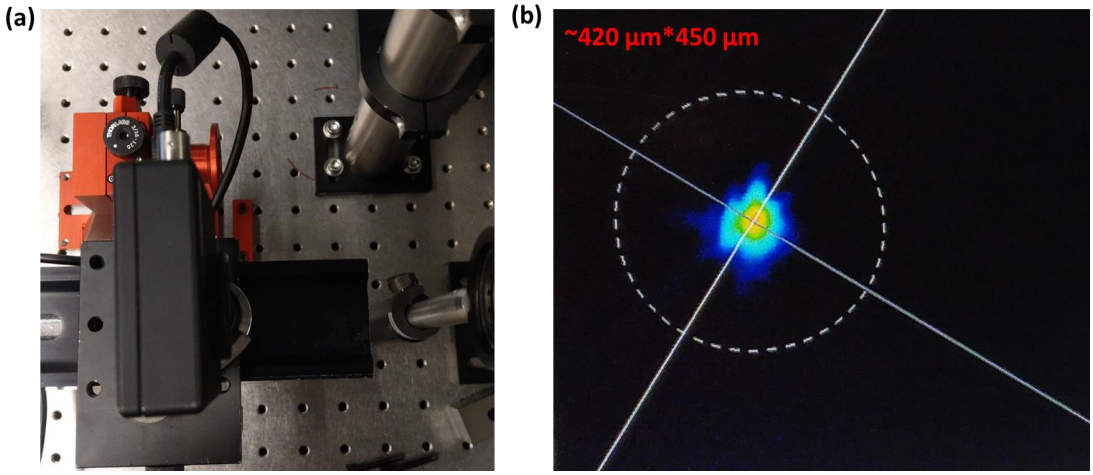

Figure 2.9 ***Beam profile measurement for the fiber input.*** *(a) A beam profiler is put at the entrance of the fiber to measure the beam profile (b) A measured beam profile of about 420 µm x 450 µm*

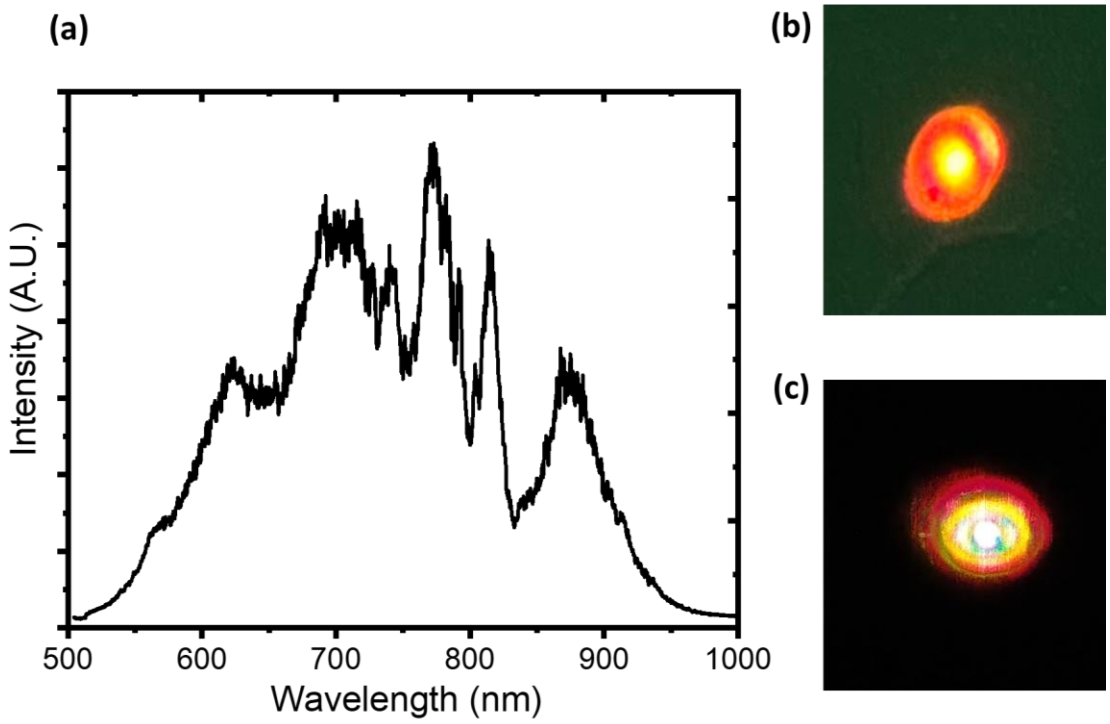

Figure 2.10 ***Optimal condition for the fiber output.*** *(a) An idea fiber spectrum should span from 550 to 950 nm (b) An idea fiber is symmetry with intense center spot (c) An overly broadened mode is observed when the neon pressure is too high.*

2.2.4 Pulse Compression

While the SPM process in the hollow core fiber produces a broadened spectrum that supports few-cycle NIR pulses, the pulse also acquires a positive chirp as an intrinsic result of SPM [46]. Compensation of this dispersion is needed for achieving short pulses, as discussed before, which can be achieved by introducing negative GDD optics, such as prisms, gratings, or chirped mirrors. Chirped mirrors are used in this lab, and they are usually multi-layer mirrors that have different penetration depths for different wavelengths to provide negative GDD. In the new apparatus, eight pairs of double angle chirped mirrors (PC70, Ultrafast Innovations) are used to provide enough negative GDD to compensate the positive chirp introduced by hollow core fiber.

In practice, chirped mirrors are used to overcompensate the GDD to allow for fine-tuning of the dispersion by pairs of fused silica wedges. Meanwhile, as the hollow core fiber also introduces significant negative TOD, ammonium dihydrogen phosphate (ADP) is also added into the beam path to help reduce the amount of TOD [48]. Table 2.4 shows the GDD/mm and TOD/mm values for both fused silica and ADP. These values suggest that a combination of fused silica and ADP can compensate for any dispersion containing a TOD/GDD ratio from 0.76 to 1.91. Please note that ADP is a birefringent material, as shown in Table 2.4, and it should be used at its ordinary axis. In the new apparatus, 3 mm thickness of ADP is used together with a pair of fused silica wedges to compensate the dispersions. The quality of dispersion compensation, as well as the pulse structure, is measured by using a commercial dispersion scan device (D-Scan, Sphere Ultrafast Photonics). Figure 2.11 shows a d-scan result of an optimal pulse with only -2 fs^2 GDD and -15 fs^2 TOD, yielding a 3.89 fs pulse with 84% relative peak power. In daily operation, a pulse with <5 fs duration with at least 70% relative peak power is good enough for the FWM experiments.

Materials	**GDD/mm (fs^2/mm)**	**TOD/mm (fs^3/mm)**	**TOD/GDD Ratio**
Fused Silica	36.11	27.44	0.76
ADP	28.7 (O) 36.9 (E)	54.8 (O) 34.0 (E)	1.91 (O) 0.92 (E)

Table 2.4 ***Dispersion values for both fused silica and ADP.*** *The GDD and TOD values are given as per mm of the material. ADP consists of two different dispersion values depending on the optical axis used.*

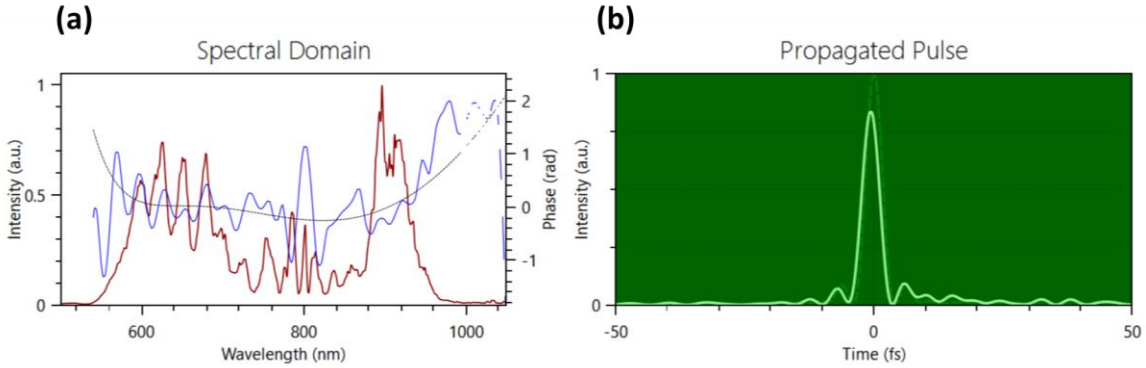

Figure 2.11 ***A D-scan result of 3.89 fs pulse.*** *(a) a measured NIR spectrum and its reconstructed phase (b) the reconstructed pulse shape*

2.3 Vacuum System

2.3.1 Overview

XUV spectroscopy is effectively operated under vacuum since XUV light is significantly absorbed by air. A schematic of the vacuum system in the new apparatus is illustrated in Figure 2.12. The vacuum system consists of five different chambers: the HHG chamber, filter chamber, toroidal chamber, main chamber, and spectrometer chamber. Three different turbopumps are used in this vacuum system to pump down the HHG chamber, main chamber, and spectrometer chamber, respectively. Information regarding the pumps and the ultimate pressure of the chambers is provided in Table 2.5. The pressures in the vacuum chambers are typically in the 10^{-7} to 10^{-8} Torr region. It should be noted that vibrational isolators (NEC Model VI-1) are installed beneath the turbopumps TMP-2203LMC and TMP-203LM, as shown in Figure 2.12, to reduce the effect of vibration produced by the pumps.

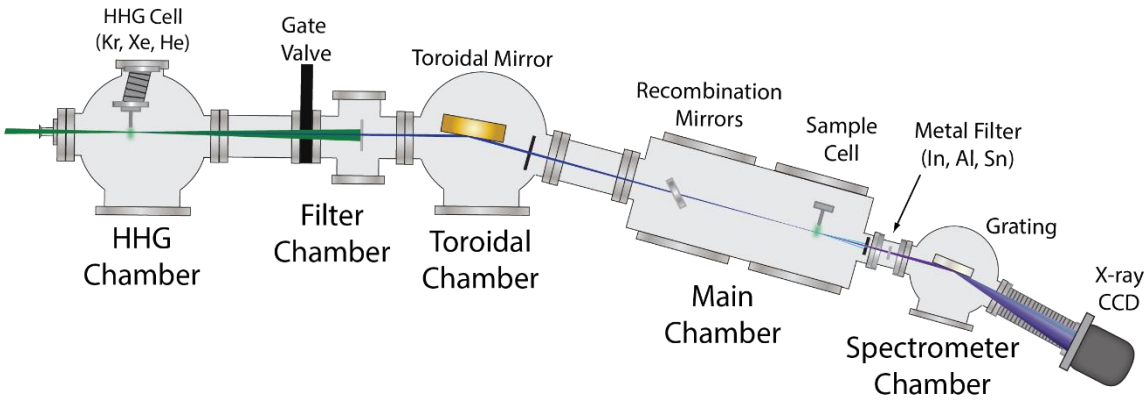

Figure 2.12 ***A schematic of the vacuum system.*** *Details are described in the main text.*

Chamber	**Turbo pump**	**Pumping Speed**	**Roughing pump**	**Pressure (Torr)**
HHG	Shimadzu TMP-3304LM	3200 L/s	nXDS-20iC (20 m^3/hr)	$2*10^{-8}$
Main	Shimadzu TMP-2203LMC	2050 L/s	nXDS-10iC (10 m^3/hr)	$2*10^{-7}$
Spectrometer	Shimadzu TMP-203LM	190 L/s	nXDS-10iC (10 m^3/hr)	$4*10^{-7}$

Table 2.5 ***Different pumps used in the vacuum system.*** *Basically, two big turbo pumps with 3200l/s and 2050l/s are used to pump down the HHG and main chamber, respectively. A small turbo pump with 190 l/s is used to support the pumping on a smaller spectrometer chamber.*

To perform experiments, few-cycle NIR pulses enter the chamber from the HHG side and are focused into a HHG cell flowing with rare gas to produce attosecond XUV pulses through HHG process. A metallic filter in the filter chamber removes the co-propagating NIR pulses and selects a specific XUV spectral region before the XUV pulses

enter the toroidal chamber. The XUV pulse is then focused into a sample gas cell in the main chamber by a gold-coated toroidal mirror (f = 50 cm, ARW). Meanwhile, two additional NIR pulses enter the main chamber from a side port and are reflected by recombination mirrors to interact with the XUV pulse in a noncollinear geometry at the position of the sample cell. After the interaction area, a second metallic filter, located in a gate valve between the target and spectrometer chambers, removes the remaining NIR pulses. The transmitted XUV pulse, along with FWM signals, then enters the spectrometer chamber and is dispersed by an aberration corrected flat-field grating (Hitachi). The dispersed pulses are subsequently detected by an X-ray CCD camera (Pixis XO 400B, Princeton Instruments). Detailed discussions of each important component of the vacuum system, including HHG, metallic filter, sample delivery, and spectrometer chamber, are provided in the following sections.

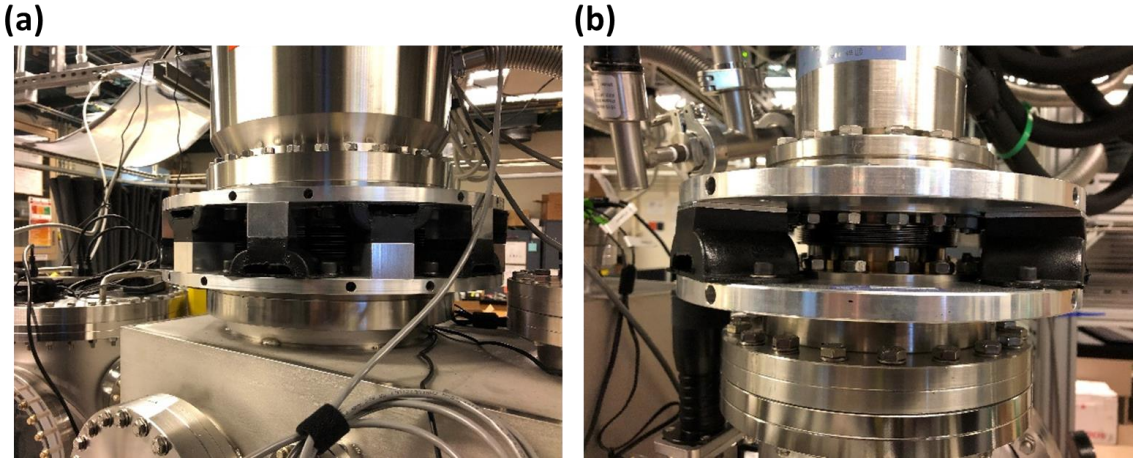

Figure 2.13 ***Vibrational isolators installed beneath the turbo pump.*** *(a) the TMP-2203LMC turbo pump on the main chamber (b) the TMP-203LM turbo pump on the spectrometer chamber.*

2.3.2 High Harmonic Generation in the HHG Chamber

The theoretical description of HHG has already been provided in Chapter 1. In this section, the practical conditions and daily operation of HHG generation are described.

To perform HHG, a concave mirror (f = 45 cm) located outside of the vacuum apparatus focuses the NIR pulses, with a pulse energy of ~700 μJ, through a 1 mm AR-coated fused silica window into a 1 mm diameter gas flow cell with 300 μm diameter entrance and exit holes. A 3-D translational stage outside the chamber is utilized to adjust the x, y, z position of the HHG cell, which is shown in Figure 2.14. Different rare gases are used for generating XUV pulses at different photon energies. The experiments described in this dissertation cover a range of 15-70 eV and the gases used in different energy regions are shown in Table 2.6.

Photon Energy	15-25 eV	25-45 eV	45-70 eV
Gas	Xenon	Krypton	Argon

Table 2.6 ***Gas choice for generating XUV pulse at different photon energy.***

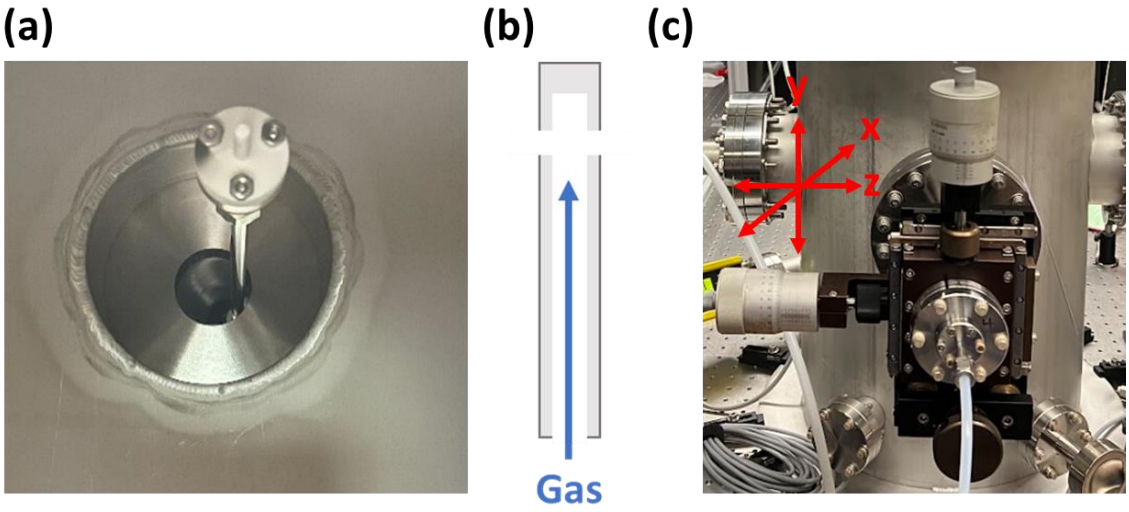

Figure 2.14 ***HHG gas flow cell.*** *(a) a picture of HHG cell in the chamber (b) the schematic of the gas cell (c) a 3D translational stage outside the chamber is used to control the x, y, z motion of the HHG cell in the chamber.*

For the alignment process, first, the translational stage is utilized to move the gas flow cell out of the beam path in the y direction, and the NIR driver is aligned through the toroidal mirror and grating. Once that is completed, the cell is moved back to the beam path and the rare gas is introduced to generate the XUV pulse. Pointing of the NIR beam can be fine-tuned while walking the x, y position of the gas cell to optimize the XUV pulse flux. Afterwards, the z-direction position of the cell, corresponding to the focusing condition, as well as the gas pressure and dispersion compression conditions, are adjusted to achieve the best shape of the high harmonic structure on a camera image. Since the characterization of the attosecond pulse is not available in the current setup, the harmonic structure is used as a gauge to determine if the XUV pulse is close to an IAP or not. An IAP should yield a more continuous spectrum rather than the discrete harmonic as shown in figure 2.15. If the XUV flux is not ideal, re-tuning of the hollow core fiber may be needed.

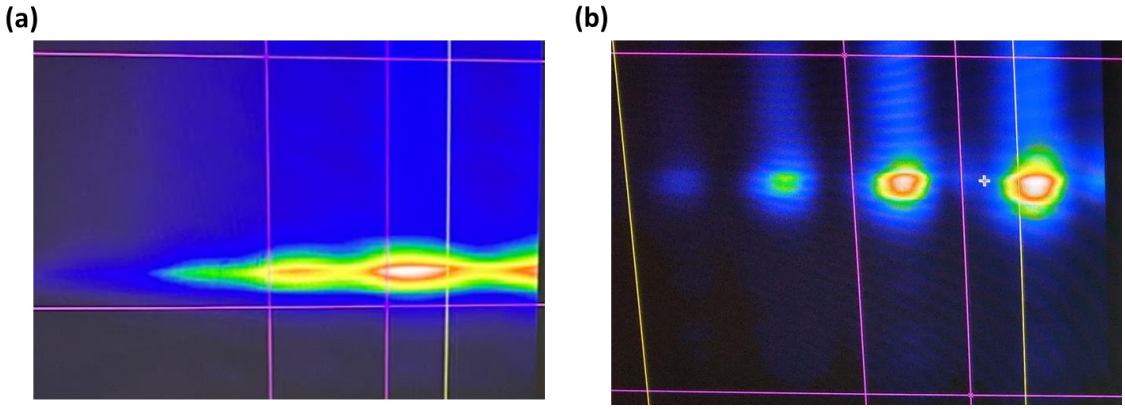

Figure 2.15 ***Camera images of the XUV pulse generated through HHG.*** *The horizontal axis in the image is related to photon energy while the vertical axis represents the beam divergence (a) a continuum spectral represents an IAP (b) the discrete harmonic structure mostly comes from attosecond pulse train.*

2.3.3 *Metallic Foil Filter*

After the HHG process, it is essential to remove the co-propagating NIR driving field before entering the target cell to avoid any nonlinear signals generated from the XUV pulse and its copropagating NIR pulse. This is accomplished by inserting a thin metallic foil into the beam path. The thin metallic foil not only eliminates the NIR photons but also only allows for part of the XUV bandwidth to be transmitted. The transmission as a function of XUV photon energy of two metallic filters used in this lab, In and Al, are plotted in Figure 2.16. The Al filter is usually the best option for photon energies ranging from 17 to 70 eV, while In may be used for experiments with photon energies <17 eV. It's worth noting that the transmission of the Al_2O_3 is also plotted in the Figure 2.16 and it's nearly zero for the entire spectral region. As a result, the filters should be kept under vacuum even when not in use to prevent the oxidization. A small vacuum chamber backed by a roughing pump (Edward, nXDS-10iC) is used to store the spare filters at a pressure of about 10^{-2} Torr.

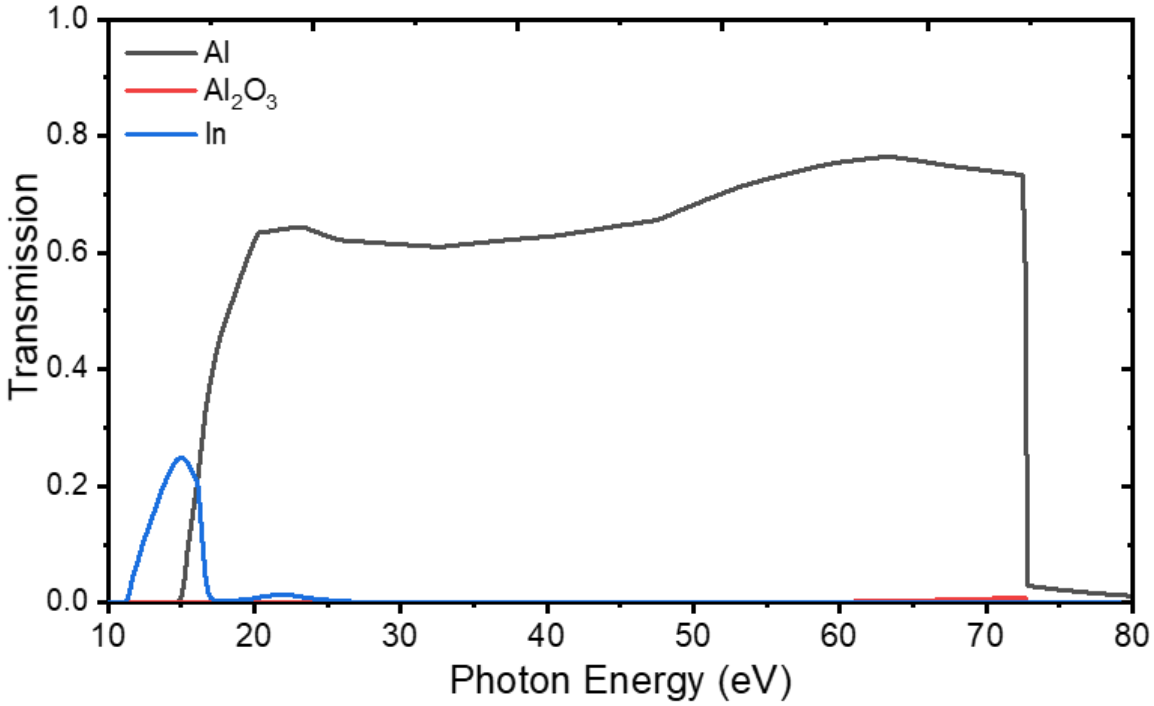

Figure 2.16 ***Transmission of Al, Al_2O_3, and In as a function of XUV photon energy.*** *It is assumed the thickness of the filter is 0.2 μm in this plot.*

2.3.4 *Sample Delivery*

As mentioned earlier, after passing through the filter, the XUV pulses are focused by an Au-coated (f = 50 cm) toroidal mirror to a sample cell located 1 m away using a 2f-2f focusing geometry. All the experiments in this dissertation involve gas-phase samples, and the same design of the gas flow cell as the HHG cell is used for the sample cell, as shown in Figure 2.17. The sample cell has its own 3D translational stage. During the optimization of the HHG process, the sample cell is moved out of the beam path to avoid any artificial alignment constraints. Once the HHG is optimized, the sample cell is carefully

adjusted in the x and y directions using the translational stage to find the position that allows for the maximum transmission of the XUV pulses.

While it was not entirely successful, an attempt was made to introduce the vapor of solid or liquid samples, such as I_2 or ICl. In this case, the sample is placed in a glass sample reservoir outside the vacuum chamber. Heating tapes are used to raise the sample's temperature, generating sufficient vapor pressure. As shown in Figure 2.17, the heating tapes are wrapped around the entire gas line, starting from the glass sample reservoir all the way to the sample gas flow cell, and all parts are covered with aluminum foil to prevent heat loss. To prevent sample condensation in the gas line, a temperature gradient is established, with higher temperatures closer to the gas flow cell. This setup successfully delivered the ICl sample, which only required heating to 40 °C. However, it failed to deliver the I_2 sample, which required a much higher temperature of 80 °C. Specifically, the limited thermal conductivity within the vacuum resulted in a lower-than-expected temperature in the gas flow cell, leading to sample condensation and potential clogging in the gas flow cell.

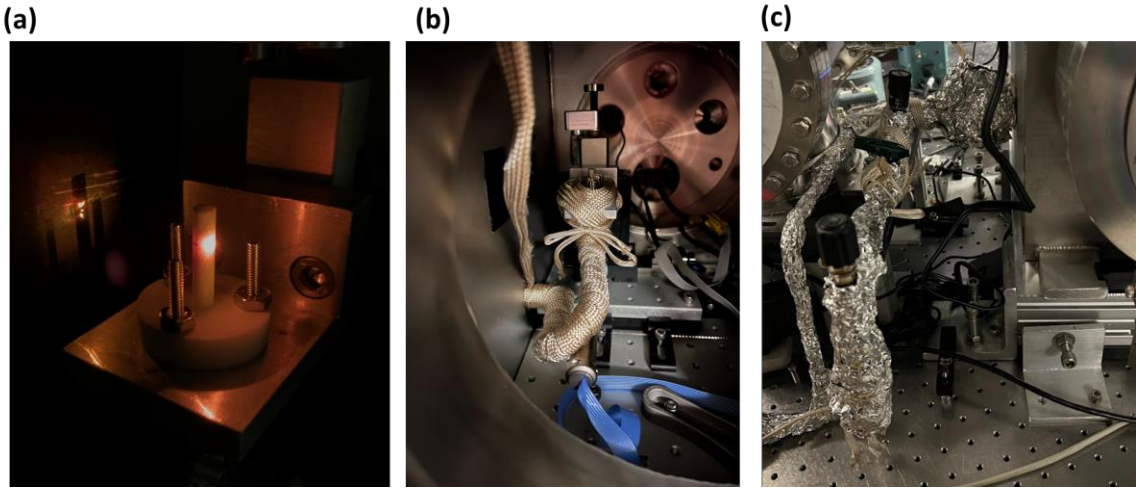

Figure 2.17 ***Sample Delivery.*** *(a) A gas flow cell is used to deliver the gas sample into the vacuum chamber (b) The heating tape was applied to the gas line inside the chamber (c) The heating tape was applied to the gas line outside the chamber, starting from a glass sample reservoir.*

2.3.5 XUV Spectrometer

After the passing the interaction area, the spectra for both the XUV pulse and FWM signals are measured to obtain the information of the sample. This is accomplished in the spectrometer chamber using gold-coated aberration-corrected concave gratings (Hitachi) to disperse the light, which is then detected by a CCD camera (Pixis IO 400B, Princeton Instruments). Table 2.7 presents detailed parameters of the two different gratings used in the experiments described in this dissertation: 001-0639 for lower XUV photon energy and 001-0640 for higher XUV photon energy.

The CCD camera consists of 20 μm x 20 μm detector chips, in a two-dimensional rectangular array of 1340 x 400 pixels. The camera is mounted so that the axis of the 1340 pixels, later referred to as horizonal axis, corresponds to the dispersed axis from the grating,

which is thus related to XUV photon energy. The other axis, later referred to as vertical axis, provides the spatial information and is usually expressed as the emission angle with respect to the wave vector of the XUV pulses. In the FWM experiments, due to the noncollinear geometry between XUV and NIR pulses, the FWM emission will occur at an angle with respect to the XUV pulse and be recorded at different vertical positions on the camera. The CCD camera mount is designed to allow the movement of the camera in two dimensions, enabling the adjustment of the detection window for different photon energies and emission angles region, as shown in Figure 2.18. An application of spatial masking of the signals will be discussed in the later section.

Grating	Grooves per mm	Blaze Wavelength (nm)	Wavelength Range (nm)	Photon Energy Range (eV)
001-0639	600	31	22-124	10-56
001-0640	1200	16	11-62	20-112

Table 2.7 ***Parameters of fiber setup in both old apparatus and new apparatus.***

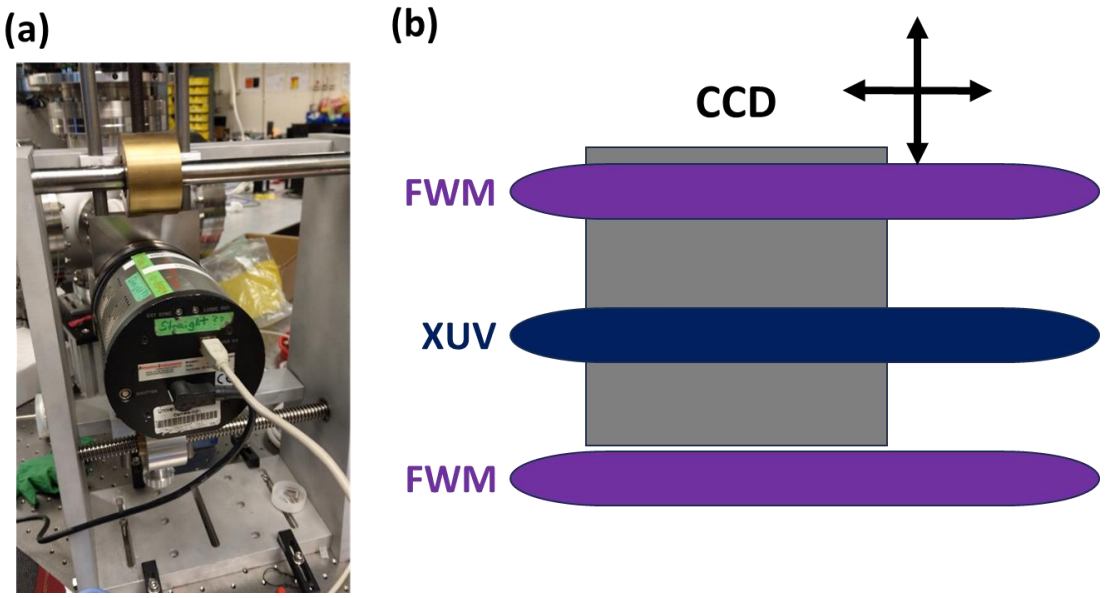

Figure 2.18 ***CCD Camera Mount*** *(a) The CCD is mount is a home-built mount that allows for the movement of the camera in 2D (b) Movement of the camera will allow for detection of the signals at different region.*

2.4 Nonlinear FWM Signal Generation

2.4.1 Interferometer

To perform time-domain measurements of nonlinear spectroscopy, precise timing control between multiple pulses is required. This is accomplished by using interferometers. As depicted in Figure 2.1, the few-cycle NIR pulses generated after hollow core fiber and chirped mirrors are firstly split into two different arms: the inner arm and the outer arm. The inner arm is directed towards the HHG chamber to act as the driving field for the HHG process, generating XUV pulses. Meanwhile, the outer arm is first delayed by t_1 with

respect to the inner arm, or XUV pulses, by a piezoelectronic stage (P-622 with E509 controller, Physik Instrumente). Subsequently, it is further split into two arms: the upper arm and the lower arm. The lower arm is delayed by another t_2 with respect to the upper arm, controlled by a second piezoelectronic stage. Both arms are then focused by focusing mirrors with a focal length of 1 m and enter the main chamber through a side port. There are two recombination mirrors in the chamber and each of them reflects one arm to intersect with the XUV pulses at a certain crossing angle. The interaction between the three pulses and the sample produces nonlinear FWM signals.

The temporal delay between the pulses is determined by the path length difference between the pulses controlled by the piezoelectronic stage, and they are related by the speed of light:

$$\Delta t = \frac{\Delta x}{c} \tag{2.5}$$

where Δt is the temporal delay, Δx is the path length difference, and c is speed of the light. Most of the experiments discussed in this dissertation have a step size of 1 fs delay, corresponding to a path length difference of 300 nm. Since the path through delay stage is round-trip, the delayed stage only moves 150 nm for that.

2.4.2 Crossbeam Geometry

Besides the temporal information, beam geometry as well as its phase matching conditions are other important experimental parameters, as they can be utilized to isolate different pathways of third-order polarization signals, as discussed in Chapter 1. In all the experiments detailed in this dissertation, the crossbeam geometry is used, and its schematic is illustrated in Figure 2.19 (a). In this geometry, two NIR pulses intersect with XUV pulses at angles of θ_{NIR1} and θ_{NIR2}, respectively. The phase matching condition for this beam geometry is shown in Figure 2.19 (b). Basically, the generated FWM emissions will be at an angle ϕ_{FWM} with respect to the XUV wavevector. In the experiments, θ_{NIR1} and θ_{NIR2} are small, typically around 1°, and small-angle approximations can be applied to relate ϕ_{FWM}, and θ_{NIR1} and θ_{NIR2} under the phase matching condition [14]:

$$\phi_{FWM} = \frac{E_{NIR1}\theta_{NIR1} + E_{NIR2}\theta_{NIR2}}{E_{FWM}} \tag{2.6}$$

where E_{NIR1}, E_{NIR2}, and E_{FWM} are the photon energies of NIR1, NIR2, and FWM signals, respectively. Except for the O_2 experiment detailed in Chapter 3, in most of the experiments, two NIR pulses have some same photon energy as well as crossing angle. In that case, Equation (2.6) can be simplified as

$$\phi_{FWM} = \frac{2 * E_{NIR}\theta_{NIR}}{E_{FWM}} \tag{2.7}$$

For experiments with NIR crossing angles of 1°, the FWM angle is about 2 mrad for an XUV photon energy around 25 eV. However, it becomes less than 1 mrad when the XUV photon energy exceeds 50 eV. As the divergence of the XUV pulses generated in the current setup is typically around 2 mrad. The FWM angle needs to be at least 1 mrad to be isolated from the interference of XUV pulses, as illustrated in Figure 2.20. This can be achieved by increasing the NIR crossing angle or by increasing the photon energy of the probe beam. The FWM emission angle as a function of XUV photon energy is plotted in Figure 2.20 with several probing conditions.

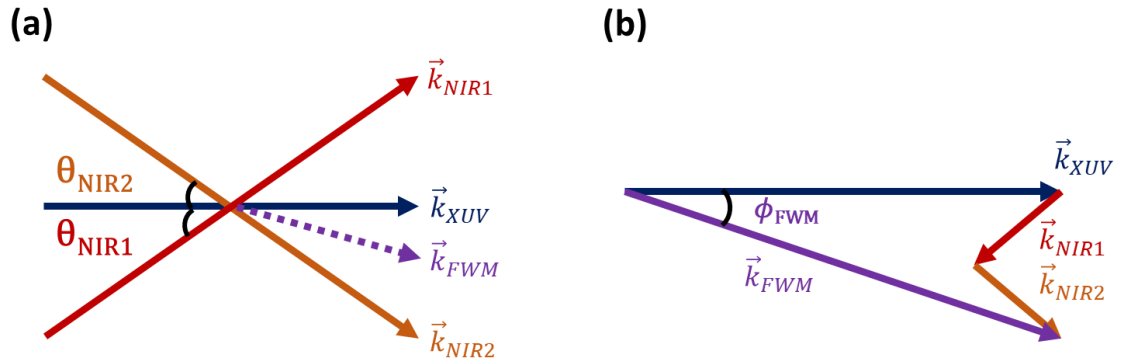

Figure 2.19 ***Noncollinear Beam geometry*** *(a) A schematic of the crossbeam geometry used in the experiments (b) The phase matching diagram of the corresponding beam geometry.*

Two modifications have been made to the new apparatus to enhance the accessibility of higher NIR crossing angles. Firstly, the side port of the main chamber is modified to include a dual-window flange as shown in Figure 2.21. With this change, the two NIR arms can enter the main chamber from different windows and thus increase the spatial separation between the two beams. The other modification involves using two separate mirrors for recombination, which can be adjusted in height to achieve different NIR crossing angles, as shown in Figure 2.22. Currently, the two mirrors are positioned 0.58 inches away from each other, allowing the NIR crossing angle of 2°.

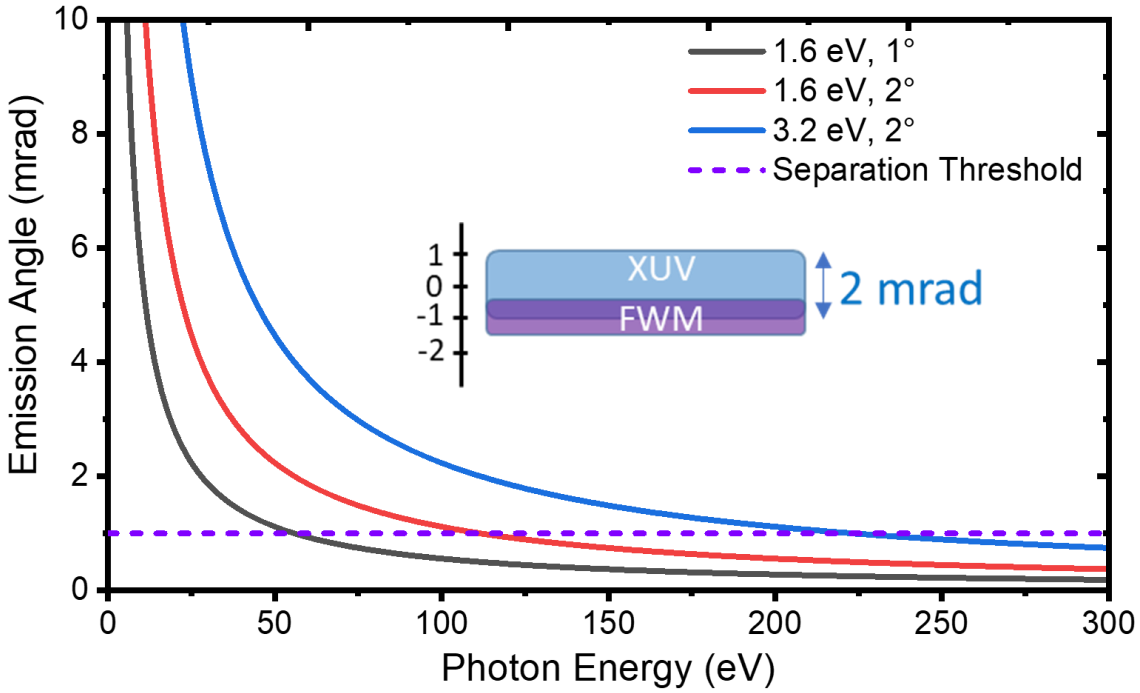

Figure 2.20 ***Consideration of FWM Emission Angle.*** *The FWM emission as a function of XUV photon energy is plotted at three different conditions. A horizontal dashed line represents the minimum angle required to separate the FWM signals with XUV pulse.*

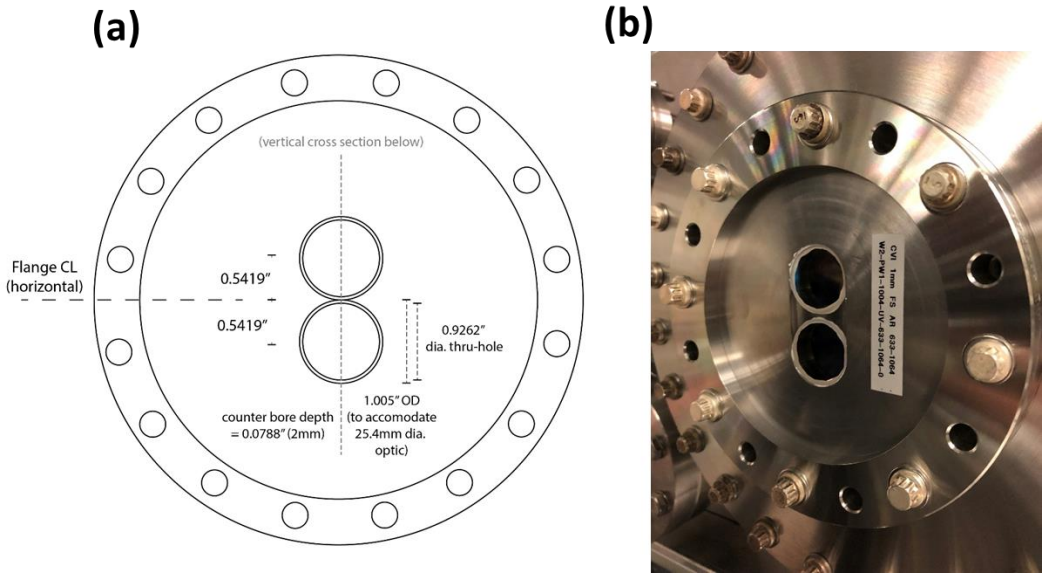

Figure 2.21 ***New Dual-Window Flange implemented on the main chamber.*** *(a) A schematic of the flange design (b) Two AR coated windows are glues on the flange.*

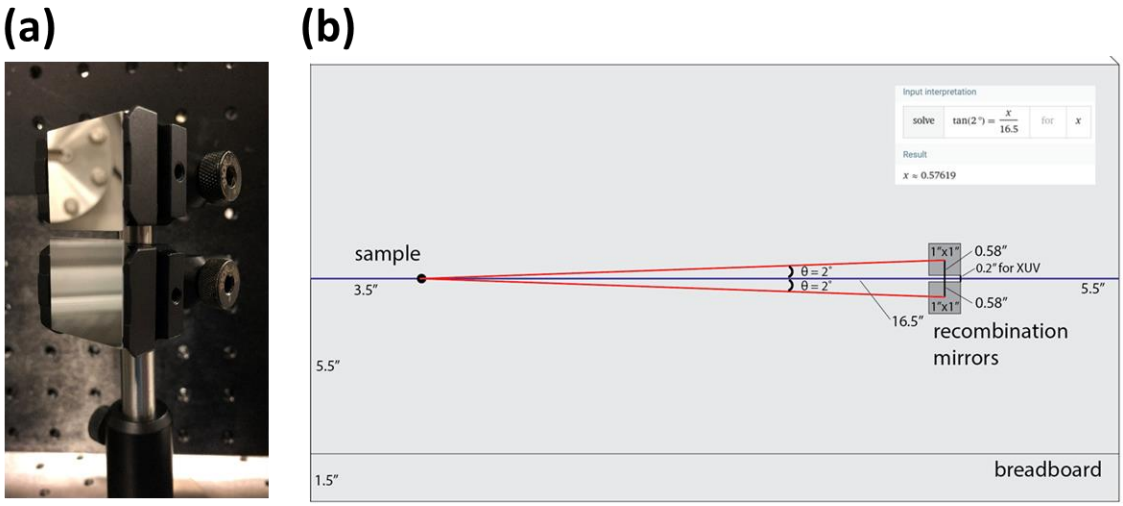

Figure 2.22 ***New Design for the Recombination windows.*** *(a) Two separated square mirrors with adjustable height are used for the recombination. (b) With two mirrors separated by 0.58 inches, a NIR crossing angle of 2° can be achieved.*

2.4.3 Temporal and Spatial Overlap Determination

To ensure meaningful time domain measurements in nonlinear spectroscopy, it is crucial to determine the temporal overlap of each pulse, which represents the time zero for each time delay. Additionally, achieving spatial overlap is essential to generate a stronger intensity of the nonlinear signal. To determine the overlap for the three pulses, a pickup mirror is inserted into the main chamber, reflecting all the NIR arms to a fast photodiode. The NIR pulse of the inner arm is used as a reference for the XUV pulse. The fast photodiode has a temporal resolution of 100 ps, effectively reducing the delay between all three pulses to less than 150 ps, equivalent to a path length of less than 1 inch.

Next, a BBO crystal is positioned at the focal point of the three pulses, as shown in

Figure 2.23 (a). Initial adjustments for spatial overlap are made by aligning all three beams to the same spot on the BBO crystal. The delay stage is then scanned to find second harmonic generation (SHG) signals appearing at a wavevector between any two incident pulses, indicating the overlap. Subsequently, beam pointing and the delay stage are fine-tuned to optimize the SHG signal, ensuring the best spatial and temporal overlap. As there are two delay stages, the first stage has to be scanned first to optimize SHG signal between upper arm and inner arm to ensure t_1=0. The second stage is then scanned for the best SHG signal between lower arm and inner arm to ensure t_2=0. A picture when all three pulses are overlapped is shown in Figure 2.23 (b).

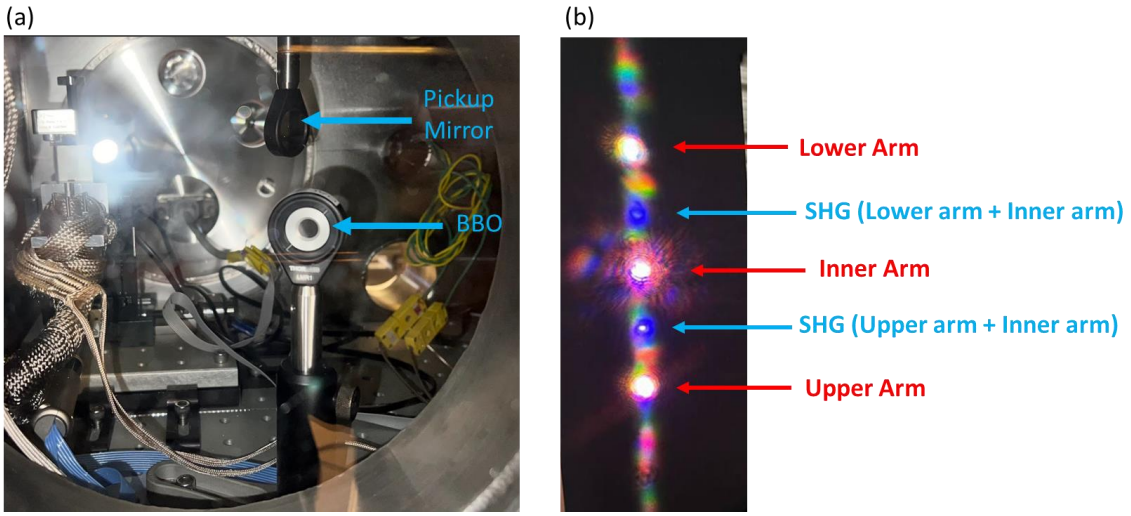

Figure 2.23 ***Temporal and Spatial Overlap Determination.*** *(a) A pickup mirror is inserted to reflect the all the pulses on a BBO crystal. (b) A picture when all three pulses are in overlap.*

2.5 Method to Reduce Background Signal

Generally, the FWM signal is weak due to the low flux in the XUV pulse and the low efficiency of the third-order process. Enhancing the FWM signal often requires a stronger light source, which may not be feasible. However, several methods have been employed to significantly reduce the background signal that suppresses the FWM signal, thereby improving the data quality. In this section, we introduce two of the most important methods to reduce the background.

2.5.1 Reducing NIR Background

After the interaction region, the NIR pulses from outer arms need to be removed to prevent background signals on the CCD camera. This is usually achieved by inserting a second metallic filter located in a gate valve between the target and spectrometer chambers. However, even with low transmission of the metallic filter, the intensity of the NIR transmitted light is still comparable to the weak transmitted FWM signals, which significantly obscures the ability to detect the FWM feature. To address this, a slit made by matte black Al foil is implemented to further reduce the background from NIR pulses as shown in Figure. 2.24. A comparison of camera images with and without the slit is also shown in Figure 2.24. The camera image with the slit is much cleaner and the FWM feature above the axis can be clearly seen.

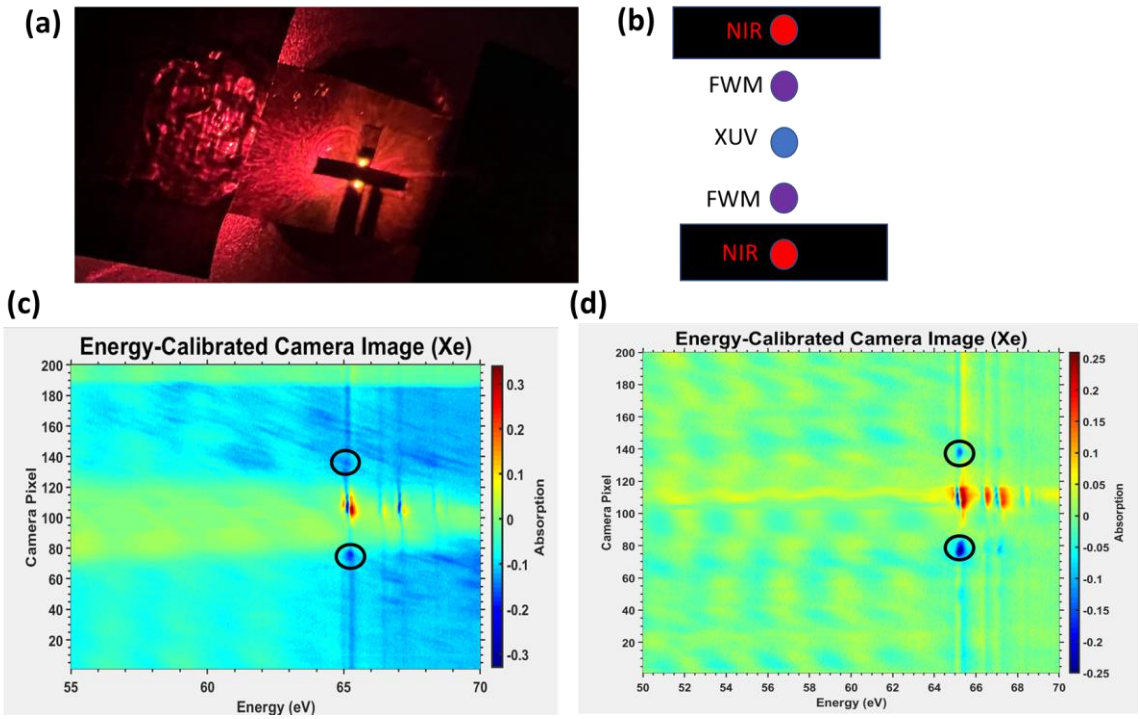

Figure 2.24 ***Reducing NIR background with a slit.*** *(a) NIR from outer arms are absorbed by matte black Al foil. (b) A schematic for how the slit work (c) A camera image without the slit, the FWM signal is obscured by the NIR scattering background (d) A camera image with the slit, the FWM feature is clearly shown.*

2.5.2 Spatial Masking of Signals

Due to the limitations of the dynamic range, strong features from the XUV can saturate at the exposure times necessary to observe FWM signals. When saturation occurs, excess charge can flow into other pixels, causing a phenomenon known as blooming. This results in a vertical line in the camera image, introducing artificial background signals that obscure the FWM signals, as shown in Figure 2.25 (a). To reduce this background signal, the CCD camera is vertically translated, creating a detection window that only captures the FWM signals. By eliminating the blooming background, the FWM feature becomes cleaner and more distinguishable, as shown in Figure 2.25 (b).

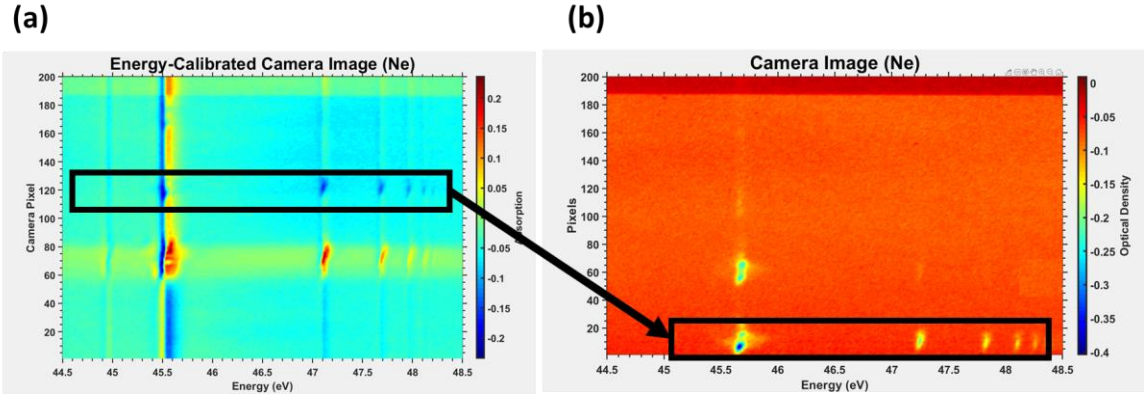

Figure 2.25 ***Spatial masking of signals.*** *(a) A camera image that captures both XUV and FWM signals. (b) A camera image that only captures FWM signals*

Chapter 3: Coupled nuclear–electronic decay dynamics of O_2 inner valence excited states revealed by attosecond XUV wave-mixing spectroscopy

*The content and figures of this chapter are reprinted or adapted with permission from Y.-C. Lin, A.P. Fidler, A. Sandhu, R. R. Lucchese, C. W. McCurdy, S.R. Leone, D.M. Neumark, Faraday discussions **228**, 537 (2021).*

3.1 Abstract

Multiple Rydberg series converging to the O_2^+ $c\ ^4\Sigma_u^-$ state, accessed by 20-25 eV extreme ultraviolet (XUV) light, serve as important model systems for the competition between nuclear dissociation and electronic autoionization. The dynamics of the lowest member of these series, the $3s\sigma_g$ state around 21 eV, has been challenging to study owing to its ultra-short lifetime (< 10 fs). Here, we apply transient wave-mixing spectroscopy with an attosecond XUV pulse to investigate the decay dynamics of this electronic state. Lifetimes of 5.8±0.5 fs and 4.5±0.7 fs at 95% confidence intervals are obtained for v=0 and v=1 vibrational levels of the *3s* Rydberg state, respectively. A theoretical treatment of predissociation and electronic autoionization finds that these lifetimes are dominated by electronic autoionization. The strong dependence of the electronic autoionization rate on the internuclear distance because of two ionic decay channels that cross the *3s* Rydberg state results in the different lifetimes of the two vibrational levels. The calculated lifetimes are highly sensitive to the location of the *3s* potential with respect to the decay channels; by slight adjustment of the location, values of 6.2 and 5.0 fs are obtained computationally for the v=0 and v=1 levels, respectively, in good agreement with experiment. Overall, an intriguing picture of the coupled nuclear-electronic dynamics is revealed by attosecond XUV wave-mixing spectroscopy, indicating that the decay dynamics are not a simple competition between isolated autoionization and predissociation processes.

3.2 Introduction

The competition between autoionization and predissociation in highly excited molecular electronic states is of great interest to the scientific community as it addresses the coupling between electronic and nuclear degrees of freedom in a fundamental way[49-55]. Studies on such systems provide insights into the potential energy surfaces of these states, along with the electron correlation and non-adiabatic effects that drive their decay dynamics. Until recently, these dynamics have been inferred from frequency-domain measurements, such as linewidths in absorption cross sections from synchrotron or electron scattering experiments [53,56-60]. However, the advent of ultrafast light sources in the XUV region of the spectrum has enabled direct measurements of excited state lifetimes through novel spectroscopic techniques, thereby opening new windows into the decay mechanisms of these states [61-64]. In this Chapter, we employ the recently developed method of attosecond XUV wave-mixing spectroscopy [7-13] to very short-lived (<10 fs)

Rydberg states of O_2 and, in conjunction with state-of-the-art theory, unravel the interplay between autoionization and predissociation with vibrational state-specificity.

The Rydberg series converging to the O_2^+ $c\ ^4\Sigma_u^-$ state represent a good model to study such competing decay dynamics and have thus been extensively investigated during the past few decades [56-80]. The interaction of O_2 with 20-25 eV extreme ultraviolet (XUV) photons excites an inner shell $2\sigma_u$ electron to the Rydberg states comprising these series. There are two such series observed in the XUV absorption spectrum, denoted as $2\sigma_u^{-1}nl\sigma_g(l = 0,2)$, here abbreviated as *ns* and *nd* Rydberg series [63,65]. As shown in Figure 3.1(a), these Rydberg states lie above several ionic states. They can thus undergo electronic autoionization through the rearrangement of their electronic structure, in which electron correlation couples states with different molecular orbital occupancies. Moreover, as shown in Figure 3.1(b), the Rydberg and ionic states have shallow wells that support a small number of vibrational levels and can undergo predissociation via tunneling.

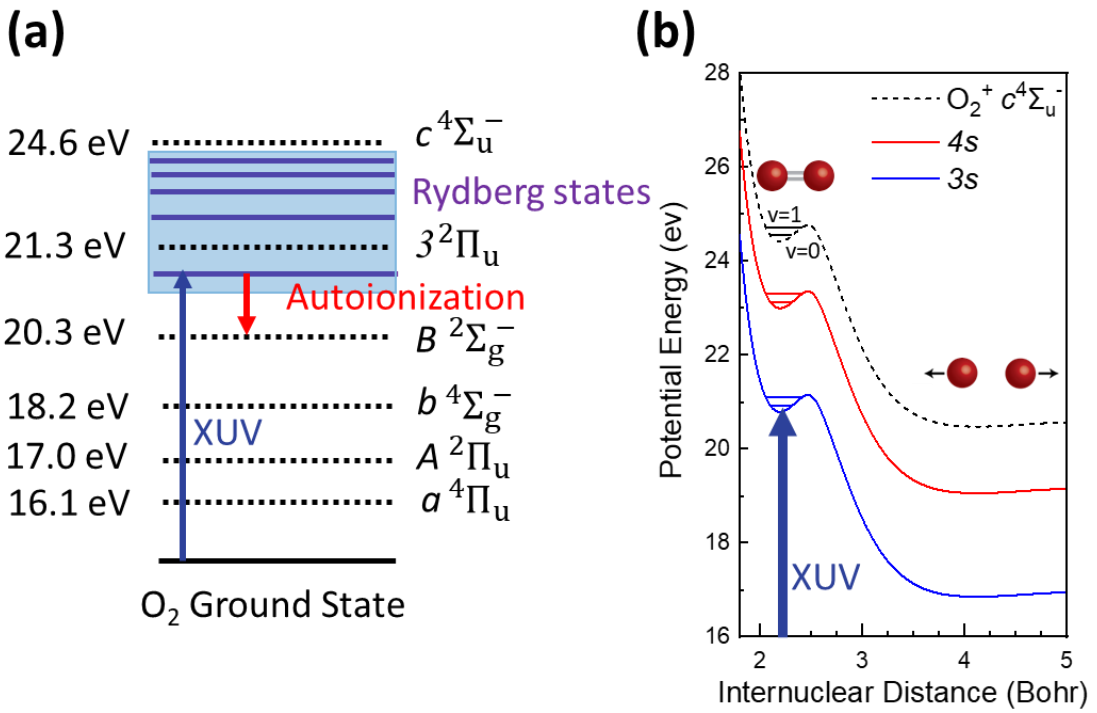

Figure 3.1 (a) Energy level diagram of O_2^+ states and Rydberg states converging to O_2^+ $c\ ^4\Sigma_u^-$ state. Dash lines are the ionic state while solid lines are neutral Rydberg states. The values of ionization potentials are from Ref [72]. The Rydberg states are energetically above several ionic states, to which they can autoionize. (b) Schematic potential energy curves of O_2^+ $c\ ^4\Sigma_u^-$ state and its 3s and 4s Rydberg states.

Direct lifetime measurements can give insight into competing pathways when linewidth measurements are not easy to deconvolve due to spectral congestion and overlap. For two competing parallel pathways, the observed decay rate (inverse lifetime) is the sum of the decay rates of each channel as shown in Equation (3.1)

$$\frac{1}{\tau^{(nl,\mathrm{v})}} = \frac{1}{\tau_a^{(nl,\mathrm{v})}} + \frac{1}{\tau_d^{(nl,\mathrm{v})}} \tag{3.1}$$

where *nl* specifies the electronic quantum numbers of the Rydberg electron, v is the vibrational quantum number of the *nl* state, and $\tau^{(nl,\mathrm{v})}$, $\tau_a^{(nl,\mathrm{v})}$, and $\tau_d^{(nl,\mathrm{v})}$ are the overall, autoionization, and predissociation lifetimes, respectively. This equation (when multiplied by $\hbar$) is simply the assertion that the partial widths of a metastable state in scattering or photoionization add up to the total width, which is usually true to a good approximation [81].

In the ion-core approximation, an electron in a Rydberg orbital is a spectator to nuclear motion, and the potential energy curves of the Rydberg states are approximately parallel to the ionic state to which they converge as shown in Figure 3.1(b) [53,57-59,63,75-77,79,82]. Therefore, both the vibrational structure and predissociation dynamics of Rydberg states are similar to those of the corresponding ionic state. The predissociation lifetimes are then largely independent of the principal quantum number of the Rydberg state, while depending strongly on the vibrational level. On the other hand, electronic autoionization is known to vary significantly within a Rydberg series, but its rate has generally been assumed to be independent of vibrational quantum number for this system [59,62,78]. With these assumptions, Equation (3.1) could be approximated as

$$\frac{1}{\tau^{(nl,\mathrm{v})}} \approx \frac{1}{\tau_a^{(nl)}} + \frac{1}{\tau_d^{(\mathrm{v})}} \tag{3.2}$$

Equation (3.2) has been invoked frequently to explain the lifetime behavior of the Rydberg series converging to the O_2^+ $c\ ^4\Sigma_u^-$ state [59,61-64,77,78]. Three different vibrational levels of the O_2^+ $c\ ^4\Sigma_u^-$ state have been observed by photoelectron spectroscopy, namely v=0, v=1, and v=2 [72]. The v=2 level is slightly above the barrier of the predissociation potential. The relative Franck-Condon factors are 1: 042: 0.015 for v=0, v=1 and v=2, respectively [72], and the v=2 level has yet to be observed in the neutral Rydberg series. The predissociation lifetime (τ_d) has been measured and calculated to be ~11 ps [53,62,78] and ~65 fs [57-59,61,79] for the v=0 and v=1 levels, respectively, in the O_2^+ $c\ ^4\Sigma_u^-$ state, and predissociation is thought to be similar and dominant in the decay of higher *n* Rydberg states [53,57,59]. Autoionization, on the other hand, becomes a competing and even dominant channel for the lower *n* Rydberg states. For example, autoionization lifetimes (τ_a) of ~90 fs and ~180 fs were measured for *4d*/*5s* and *5d*/*6s* Rydberg states with pump-probe photoionization spectroscopy [62,64].

Equation (3.2) implies that nuclear and electronic motion are independent. i.e., vibrational excitation does not change the electronic autoionization lifetime. Thus, lifetime differences among vibrational levels in the same electronic state were previously attributed to differing predissociation rates [59,77]. However, recent studies of core-excited states suggest that the rate of Auger decay in diatomic molecule can be strongly bond-distance dependent and thus different vibrational states can give different Auger decay lifetimes [29,83,84]. Such phenomena should be observed in electronic autoionization if there is a strong coupling between electronic and nuclear motion. The lowest member in the Rydberg series, namely the *3s* Rydberg state, is a good candidate for this investigation as several ionic potentials cross near its equilibrium geometry [64]. However, in contrast to the higher *n* Rydberg states, which have been studied extensively [61-64], there are no previous direct time-domain measurements of the lifetime of the *3s* Rydberg state due to its ultra-short lifetime. Frequency domain measurements coupled with theory suggest linewidths of 145

meV and 154 meV for the v=0 and v=1 levels of the *3s* Rydberg state [59,78], respectively, corresponding to lower bounds on the lifetimes of 4.5 fs and 4.3 fs, respectively.

Recent advances in pulse compression techniques and high harmonic generation (HHG) [42,43,85] allow one to generate few-femtosecond near-infrared (NIR) pulses and attosecond XUV pulses at well-controlled time delays. This development has enabled several different kinds of pump-probe experiments, such as attosecond transient absorption (ATA), which have been used to investigate dynamics ranging from tens of femtoseconds to sub-fs. While ATA is now used in many laboratories [29,63,86-93], the resulting spectra are often complicated by spectral effects produced when pulses overlap such as the AC stark effect and strong-field line shape control [87,88]. These effects are interesting in their own right but make it difficult to extract lifetime information when the pulse duration is similar to the lifetime of interest. To disentangle this complexity, we recently developed attosecond non-collinear wave-mixing spectroscopy with one attosecond XUV pulse and two non-collinear few-femtosecond NIR pulses [7-13]. The advantage of the technique is that it spatially isolates the nonlinear response from the combined linear and nonlinear response of ATA and yields a background-free homodyne measurement that can be more cleanly interpreted than ATA. It has been used to probe the electronic and vibrational structure in atoms and molecules [7-9], and we utilized it recently to measure autoionization lifetimes in Kr [11].

In this Chapter, we report the first application of attosecond XUV wave-mixing spectroscopy to the fast-decaying dynamics in a molecule, specifically the O_2 *3s* Rydberg state. Spatially isolated wave-mixing signals are observed from this Rydberg state and the transient behavior of these signals is measured. The few-femtosecond resolution of the technique allows for direct lifetime measurements in the *3s* Rydberg state. The lifetimes for the v=0 and v=1 vibrational levels of the *3s* Rydberg state are obtained to be 5.8±0.5 fs and 4.5±0.7 fs, respectively. To explore the basis for the difference in these lifetimes, we perform *ab initio* electron-ion scattering calculations at multiple fixed internuclear distances and use the results in numerical calculations of the coupled nuclear and electronic dynamics. This theoretical description allows the details of vibrational motion to determine the effects of the varying electronic autoionization probability at each internuclear distance. The results from both experimental and theoretical work provide significant insights into the decay dynamics of the O_2 *3s* Rydberg state, indicating a subtle interplay between electronic autoionization rate and nuclear dynamics that drives the observed lifetimes.

3.3 Method

3.3.1 Experimental Setup

The experimental apparatus for attosecond non-collinear wave-mixing spectroscopy with attosecond XUV pulses has been described previously [11-13] and is shown in Figure 3.2. Briefly, a commercial Ti-sapphire laser system (Femtopower HE, Femtolasers) is used to produce 2 mJ, 22 fs NIR pulses at a 1 kHz repetition rate, which are then spectrally broadened in a 2 m long stretched hollow core fiber of 500 μm inner diameter filled with 2 bar of neon gas. Seven pairs of double-angle chirped mirrors (PC70, Ultrafast Innovations) followed by a 2 mm thick ammonium dihydrogen phosphate (ADP) crystal are used to temporally compress the pulses [48]. The resulting 5 fs broadband pulses are centered at 760 nm (~1.63 eV) with 600 μJ/ pulse. These pulses then impinge on a 25:75 beam splitter.

The majority of the pulse is transmitted and focused into a vacuum apparatus (10^{-6} Torr) by a concave silver mirror (f = 50 cm). It passes through a 1 mm path length gas cell with flowing xenon gas at approximately 5 Torr for high harmonic generation to produce attosecond pulses in the XUV region. The co-propagating NIR pulses are filtered out by a 0.15 μm thick Al foil. The transmitted XUV pulses are refocused by a gold-coated toroidal mirror (f = 50 cm) into a 1 mm path length target gas cell filled with O_2 (10 Torr backing pressure) passing through pinholes drilled for the entrance and exit of the wave mixing beams.

The reflected pulse from the 25:75 beam splitter is delayed relative to the XUV pulse using a piezoelectric stage (P-622 with E509 controller, Physik Instrumente (PI)) and further split into two separate arms with a 50:50 beam splitter. The two separate beams are each focused by concave silver mirrors (f = 1 m) and directed to reflect vertically above and below the hole of an annular mirror. Eventually, these two beams cross the XUV pulses in the target gas cell at angles of approximately 18 mrad (1.0º) and 13 mrad (0.75º) for the lower (NIR 1) and upper arms (NIR 2), respectively, to generate wave-mixing signals at different angles as shown in Figure 3.2(b). The angles of the two beams are purposely set to be different based on phase matching considerations, as will be discussed in Section 3.4.2 The combined NIR intensity is about 10^{13} W/cm^2 in this experiment. Temporal and spatial overlap between the XUV and both NIR arms is determined by transient absorption signal with helium gas. A 0.15 μm thick Al foil is placed after the target gas cell to filter out the two NIR pulses. The transmitted XUV pulse and wave-mixing signal are dispersed by a gold-coated flat field concave grating (001-0639, Hitachi) and recorded by a 1340 × 400 pixel X-ray CCD camera (Pixis XO 400B, Princeton Instruments); the long horizontal axis represents the frequency of light dispersed by the grating and the vertical axis measures the emission angle of the light.

In the transient wave-mixing experiment, the two NIR pulses are set to be time-coincident at the overlap region, and we only change the relative delay between the XUV pulse and two coincident NIR pulses with the piezoelectric stage as shown in Figure 3.2 (c). Positive delays indicate that the XUV pulse arrives at the sample earlier than the NIR pulses and vice versa for negative delays. To measure the lifetimes of the O_2 *3s* Rydberg states, delays between -10 fs to 50 fs are scanned with 1 fs steps. At each delay time, signals are accumulated for 30,000 laser pulses.

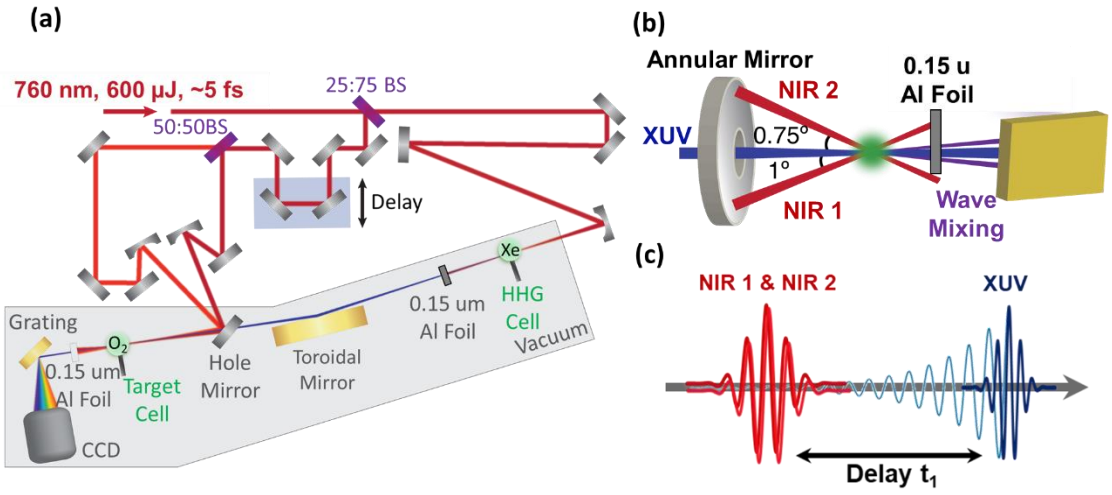

Figure 3.2 (a) Schematic of the experimental apparatus after NIR pulse compression (b) Interaction region of the three pulses. The NIR beams at angles of 1 °and 0.75 °with respect to the XUV beam are labeled NIR 1 and NIR 2, respectively. (c) Pulse sequence used to collect transient wave-mixing signals. Two time-coincident NIR pulses are delayed relative to the XUV pulse. The faint blue signal depicts the decay of the O_2 polarization that is probed by the NIR pulses through wave mixing.

3.3.2 Theoretical Methods

Theoretical results in this Chapter are supported by Dr. Robert R. Lucchese and Dr. C. William McCurdy in the AMOS program at LBNL. In the first step to describe the effect of vibrational motion on electronic autoionization of the O_2 *3s* Rydberg state, photoionization calculations are performed very similar to those reported previously [64] over a range of internuclear distances. We employed the multichannel Schwinger variational method [94,95] which is described further in several earlier applications to a variety of systems including O_2 [96-98] .

In these calculations, the final-state fixed-energy photoelectron wave functions are represented on a single center expanded grid that can be extended far enough to describe a number of Rydberg states below each ionization threshold. The full *N*-electron ionized state is represented as a close-coupling expansion containing a sum of the products of (*N* - 1)-electron ion state wave functions times one-electron photoelectron wave functions. The ion channels used in the close coupling calculation included $X\ ^2\Pi_g$, $a\ ^4\Pi_u$, $A\ ^2\Pi_u$, $b\ ^4\Sigma_g^-$, $B\ ^2\Sigma_g^-$,$1\ ^4\Pi_g$, $3\ ^2\Pi_u$, and $c\ ^4\Sigma_u^-$ states. At each internuclear distance R, a set of orbitals was computed with an aug-cc-pVTZ basis [99,100] using MOLPRO [101] with a complete-active-space-self-consistent field (CASSCF) description of the ground state keeping the $1\sigma_g$ and $1\sigma_u$ core orbitals doubly occupied. The various *N* - 1 electron ion states were then obtained from a complete active space configuration interaction calculation using the orbitals from the ground state CASSCF calculation.

These photoionization calculations produced detailed cross sections with autoionization features corresponding to members of the various Rydberg series converging to the thresholds for producing differing ion states, like those in previous studies using these methods [64,98]. Those cross sections vary strongly with internuclear

distance, as the various nearby thresholds, and their associated Rydberg series, pass through the energy of the *3s* Rydberg state studied here, as indicated in Figure 3.3.

The *3s* Rydberg state was fit with a Fano profile at eighteen different internuclear distances between 2.1 and 2.6 Bohr, which is the range of vibrational motion in the well and the barrier that binds the v=0 and v=1 vibrational levels of the *3s* Rydberg state. These fits produce both the width and the position of the autoionizing *3s* Rydberg state relative to the threshold of the O_2^+ $c\ ^4\Sigma_u^-$ state as a function of the internuclear distance. These data are the basis of the second phase of this calculation, which is the description of the nuclear dynamics. To obtain the best ion-state potential for the nuclear dynamics, the potential energy of the O_2^+ $c\ ^4\Sigma_u^-$ state was computed from a multireference configuration interaction (MRCI) calculation using MOLPRO. The valence orbitals for the reference space were obtained from a state-averaged CASSCF including the lowest two $^4\Sigma_u^-$ states and the lowest two $^4\Delta_u$ states, which are the four lowest quartet A_u states in the D_{2h} point group used in MOLPRO. The position of the autoionizing state relative to this ion-state potential provides the potential curve, $E_{res}(R)$, and the width $\Gamma(R)$, of the *3s* Rydberg state, which are the basis of the next step in the calculation.

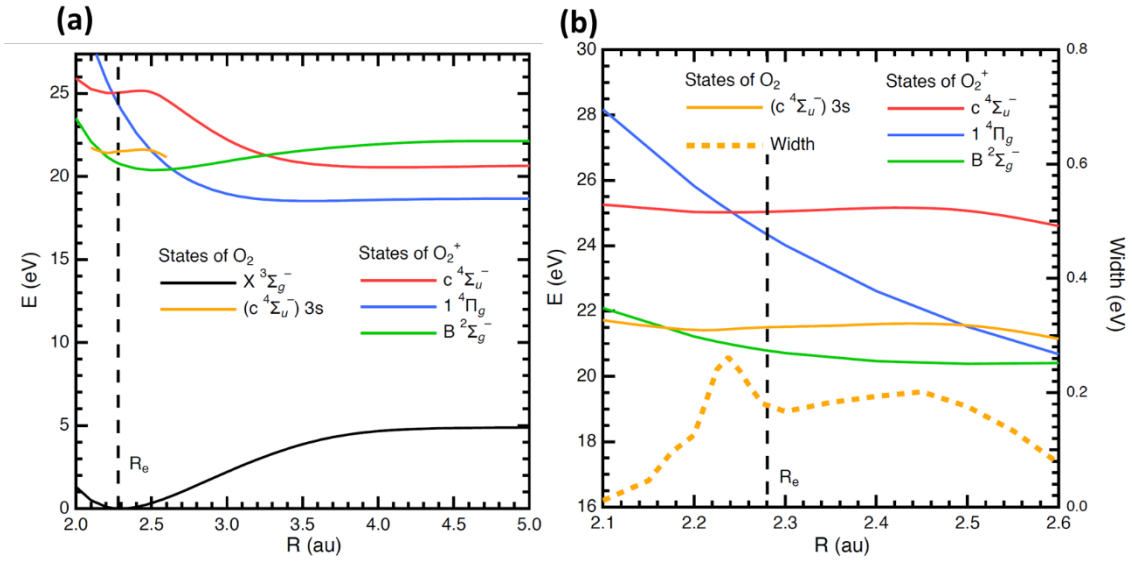

Figure 3.3 (a) Ground state potential curve of O_2 and some potential curves of the O_2^+ ion from MRCI calculations, plotted together with the real part of the energy of the 3s Rydberg autoionizing state from the multichannel Schwinger calculations. (b) Magnification of the range of R over which the scattering calculations were performed also showing width of the 3s Rydberg state and the thresholds for ionization leading to the $1\ ^4\Pi_g$ and $B\ ^2\Sigma_g^-$ states of O_2^+ that cross it.

We then make use of the well-established local complex potential mode [102,103] for nuclear motion on the potential surfaces of metastable electronic states that has been used extensively in such problems, including for polyatomic molecules with multiple vibrational degrees of freedom [104]. In this approach, we solve the radial Schrödinger equation for vibrational motion with a potential whose real and imaginary parts are determined by the energy and width of the metastable electronic state, in this case the *3s* Rydberg state,

$$\left[-\frac{\hbar^2}{2\mu}\frac{d^2}{dR^2} + E_{res}(R) - i\Gamma(R)/2\right]\psi_{\mathrm{v}}(R) = E_{\mathrm{v}}\psi_{\mathrm{v}}(R) \tag{3.3}$$

where μ is the reduced mass and $E_{res}(R)$ and $\Gamma(R)$ are the position and width of the metastable electronic state, respectively, as functions of internuclear distance.

Here the overall lifetimes of the vibrational levels, $\psi_{\mathrm{v}}(R)$, are of interest, and they arise from two effects, tunneling through the barrier indicated in Figure 1 and electronic autoionization. To calculate them directly we apply another venerable computational method, the method of exterior complex scaling (ECS) [105], to Equation (3.3). The real and imaginary parts of the potential are represented with a spline interpolation and append a long range $-\alpha/R^4$ dependence to the real part beyond 5 Bohr while setting the imaginary part to zero beyond that radius. Then for values of $R > R_0$ with $R_0 = 5$ Bohr, we make the exterior complex scaling transformation on the radial coordinate of Eq. Equation (3.3),

$$R \rightarrow \begin{cases} R & if\ R \le R_0 \\ R_0 + (R - R_0)e^{i\theta} & if\ R > R_0 \end{cases} \tag{3.4}$$

This transformation rotates the continuous part of the spectrum of eigenvalues of the Hamiltonian in Equation (3.3) into the lower complex plane and exposes the complex resonance energies as discrete eigenvalues corresponding to the now square-integrable resonance wave functions, $\psi_v(R)$. The energies, E_v, appear as isolated complex eigenvalues.

$$E_v = E_v^{real} - i\Gamma_v/2 \tag{3.5}$$

The lifetime of the metastable vibrational level is given by $\tau = \hbar/\Gamma_v$. This calculation yields lifetimes that are sensitive to the details of the vibrational wave function and how it samples the *R*-dependent electronic autoionization probability described by the local complex potential, thus describing the dynamical coupling between the nuclear motion and electronic autoionization.

The ECS calculation is implemented using the grid-based discrete variable representation using methods described at length previously [106] and used many times in ECS calculations of the complex energies of both electronic and vibrational metastable states [107-110]. In these grid-based calculations, it is a simple matter to converge the complex resonance eigenvalues so that they have no dependence on the complex scaling angle θ to many significant figures and thus represent the essentially exact solution of Equation (3.3) given the local complex potential $E_{res}(R) - i\Gamma(R)/2$. The results of these calculations and their bearing on the interpretation of the lifetimes measured for the v=0 and v=1 levels of the *3s* Rydberg state will be discussed below in Section 3.4.3.

3.4 Results

3.4.1 Camera Image and Spatial Isolation of Wave-Mixing Emission Signals

A camera image with all three pulses temporally and spatially overlapping in the O_2 gas cell is shown in Figure 3.4(a). The light impinging on the camera is spectrally dispersed in the horizontal direction by the XUV grating, while the angular displacement in the vertical direction arises from the non-collinear wave-mixing geometry used in the experiment.

The data are presented as absorbance

$$A = -log_{10}(\frac{I}{I_0}) \tag{3.6}$$

where I is the intensity of light read on the CCD camera with NIR and XUV pulses, and I_0 is a reference signal with the XUV pulse only. Positive (red) features in the image indicate absorption while negative (blue) features indicate XUV emission in the presence of NIR pulses. There are two clear regions of signals produced at different emission angles. The region around 0 mrad, which is the direction of the XUV pulse wavevector, corresponds to transient absorption of O_2. It mostly mimics the depletion feature of static XUV absorption of O_2 at this energy region. A double-hump absorption feature is seen at the center of the peaks at 20.85 eV and 21.05 eV, representing the absorption of v=0 and v=1 levels of the *3s* Rydberg state, respectively. Complex asymmetric Fano absorption features around 23 eV arise from the v=0 and v=1 levels of the *3d* and *4s* states, and the features from 23.5 eV to 24.6 eV (the IP to the $c\ ^4\Sigma_u^-$ state) are from the absorption of *4d*, *5s*, and higher *n* Rydberg states.

Off-axis pure emission regions center around 2.4 mrad for the *3s* Rydberg state and around 1.8 mrad for higher *n* Rydberg states. These are spatially-isolated wave-mixing signals generated by one XUV photon plus two NIR photons. The angle is different for the *3s* Rydberg state and higher *n* Rydberg states due to phase matching and a slight tilt of the camera.

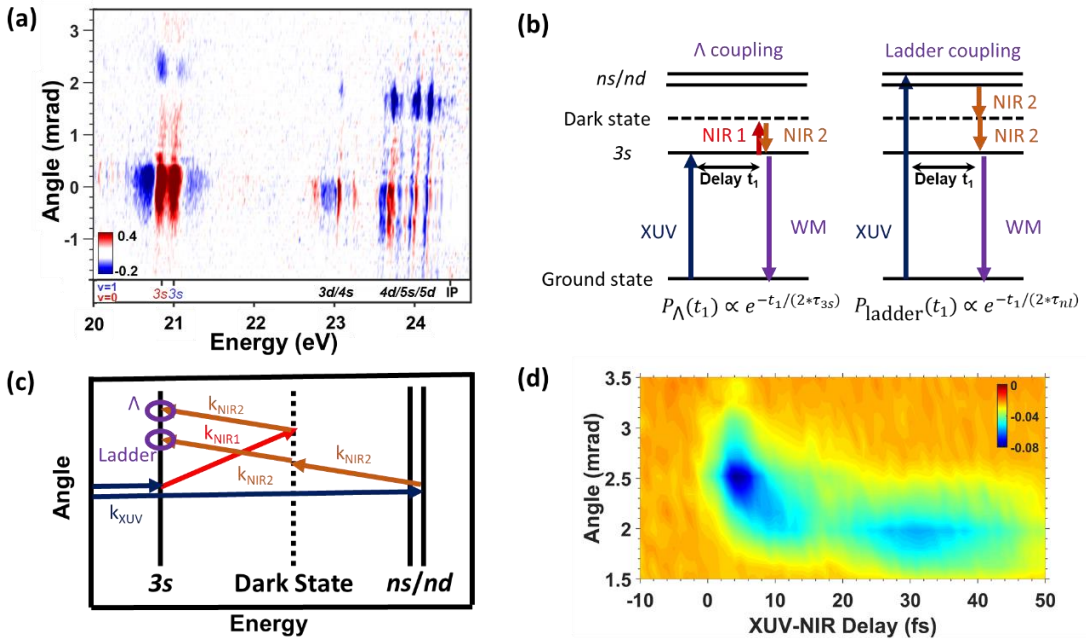

Figure 3.4 (a) Camera image at the overlap of all three pulses. Positive (red) features represent absorption while negative (blue) features represent emission. Spatially-isolated wave-mixing signals are observed around 1.5~2.8 mrad. (b) Two possible pathways to generate wave-mixing (WM) signals from the 3s state. (c) Phase matching conditions and the emission angles of Λ-type coupling and ladder-type coupling (d) Angle-dependent transient wave-mixing signals of v=0 level (20.85 eV) of the 3s Rydberg state. The component around 2.5 mrad corresponds to Λ-type coupling from 3s Rydberg state itself while the component around 2.0 mrad corresponds to ladder-type coupling from higher n Rydberg states.

The wave mixing signals can be generated through the pathways shown in Figure 3.4(b). Briefly, an XUV photon excites the O_2 into its optically allowed (bright) Rydberg states. One NIR photon can couple the Rydberg states to dark states that are not accessible from the ground state, but that are allowed from the bright Rydberg states. The second NIR photon then interacts with the dark states to create a new polarization involving different or the same bright states.

There are two possible pathways to generate wave-mixing emission from the *3s* Rydberg state as shown in Figure 3.4(b), namely Λ-type coupling from the *3s* Rydberg state and ladder-type coupling from higher *ns*/*nd* Rydberg states. The two pathways carry different transient information reflecting the dynamics of the *3s* and the higher *ns*/*nd* states, but the emission frequencies are the same (i.e. from the *3s* state), so frequency dispersion alone is insufficient to separate the signals. To isolate the dynamics from a particular wave-mixing pathway, separation of the signals is needed [10]. Here, we take advantage of phase matching conditions and use the emission angle of the wave-mixing signals to spatially separate these two pathways, as discussed in the next section.

3.4.2 Angle-dependent Transient Wave-Mixing Signals and Lifetime Measurement of 3s Rydberg state

Phase matching requires that the wavevector of the wave-mixing signal is the sum or difference of the wavevectors of XUV and NIR. The corresponding wavevector is ($k_{FWM} = k_{XUV} + k_{NIR1} - k_{NIR2}$) for Λ-type coupling and ($k_{FWM} = k_{XUV} - k_{NIR2} - k_{NIR2}$) for ladder type coupling. The emission angle of the wave-mixing signals due to the phase-matching constraint can be approximately calculated with the following expressions:

$$\varphi_{\Lambda} \approx \frac{E_{NIR1}\theta_{NIR1}+E_{NIR2}\theta_{NIR2}}{E_{WM}} \tag{3.7}$$

$$\varphi_{\text{ladder}} \approx \frac{2*E_{NIR2}\theta_{NIR2}}{E_{WM}} \tag{3.8}$$

where φ_{Λ} and φ_{ladder} are the emission angles for Λ-type and ladder-type coupling, respectively, E_{NIR1} and E_{NIR2} are the photon energies of the corresponding NIR pulses, θ_{NIR1} and θ_{NIR2} are the crossing angles of the corresponding NIR pulses with the XUV pulse, and E_{WM} is the energy of the emitted wave-mixed photon. The photon energies of both NIR pulses are approximately 1.63 eV, as the center wavelength of the NIR pulses is around 760 nm. Since both pathways emit photons from the *3s* Rydberg states, E_{WM} is 20.85 eV for the v=0 state and 21.05 eV for the v=1 state. The NIR angles are 18 mrad and 13 mrad for NIR 1 and NIR 2, respectively, as described in the experimental setup.

Using Equation (3.7) and (3.8), the emission angles of wave-mixing signals of v=0 level of the *3s* Rydberg state are calculated to be 2.42 mrad and 2.03 mrad for Λ-type coupling and ladder-type coupling, respectively. As shown in Figure 3.4(c), the two pathways should be spatially separable. To verify this, we measure the angle-dependent transient wave-mixing spectrum around 20.85 eV, the energy of the *3s* v=0 level, and the result is shown in Figure 3.4(d). In the transient signal, there are two distinct components at two different emission angles, one around 2.5 mrad and the other around 2 mrad. Based on the calculated emission angles, the signals around 2.5 mrad are assigned as Λ-type coupling, which carries information on the *3s* Rydberg state itself, while the component around 2 mrad is from the ladder-type coupling which carries information on higher *ns*/*nd* Rydberg states. As shown in Figure 3.4(d), the component around 2.5 mrad is very short-

lived while the component around 2.0 mrad is longer-lived. These observations support the assignments because the higher *ns*/*nd* states are known to be longer-lived than the *3s* state [59,61,62].

We can measure lifetimes of the *3s* Rydberg state in O_2 by integrating the component around 2.5 mrad to get transient intensities for both v=0 and v=1 levels as shown in Figure 3.5. The results are then fitted with the convolution of an instrument response function with an exponential decay. Lifetimes of 5.8±0.5 fs and 4.5±0.7 fs are found for the v=0 and v=1 levels of the *3s* Rydberg state, respectively, at 95% confidence intervals. The error bars are calculated based on the fitting results on four different data sets. Based on these confidence intervals, the lifetimes of the two vibrational levels differ significantly.

The measured lifetimes reflect electronic autoionization and predissociation as shown in Equation (3.1). To explain the difference in the two lifetimes, we need to ascertain the contribution of each decay channel to the overall lifetime of the two vibrational states. Invoking the ion-core approximation, one can use the predissociation lifetime for the v=0 state of the O_2^+ $c\ ^4\Sigma_u^-$ state, 11 ps [62], together with an electronic autoionization lifetime of 5.8 fs, to reproduce the 5.8 fs observed lifetime for that state. However, using the value of the electronic autoionization lifetime and the ion core predissociation lifetime of the v=1 state, 65 fs [61], in Equation (3.2) we obtain an expected total lifetime of 5.3 fs, which is just outside the error bars for the experimental value. This suggests that nuclear motion and electronic autoionization are not completely independent. To explore this question, we performed extensive *ab initio* calculations to determine how the electronic autoionization lifetime can be affected by nuclear motion.

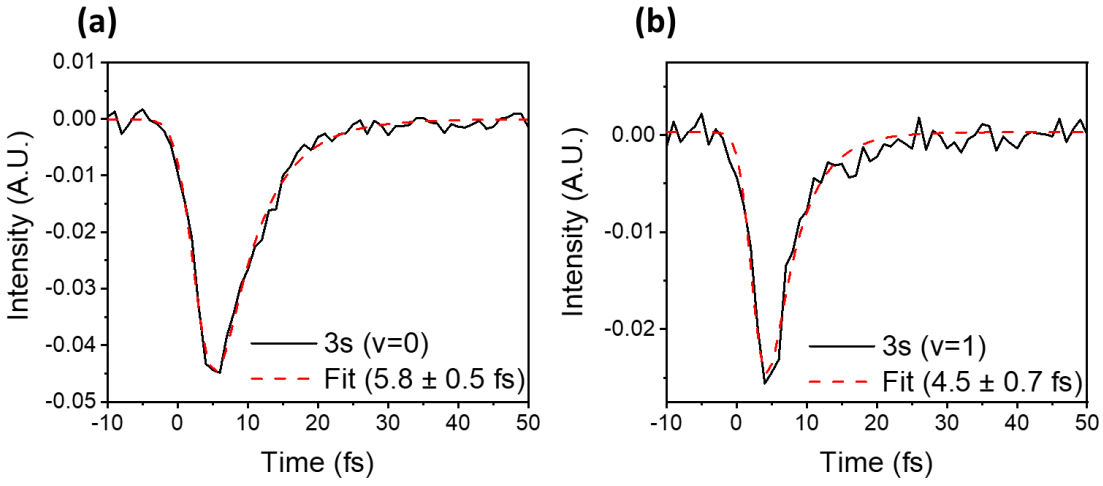

Figure 3.5 Transient wave-mixing signals integrated around 2.5 mrad emission angle on the camera image for the (a) v=0 (20.85 eV) and (b) v=1 levels (21.05 eV) of the 3s Rydberg state. The black solid line is the raw data while the red dash line is the fitted curve.

3.4.3 Coupled Vibrational and Autoionization Dynamics and Total Lifetimes of 3s Rydberg Vibrational States

The lifetimes of the v=0 and v=1 vibrational levels of the *3s* Rydberg state arise from a competition between electronic autoionization and tunneling predissociation. It is

instructive to first calculate the tunneling lifetimes of these states in the parent $c\ ^4\Sigma_u^-$ state of the cation using the MRCI potential curve shown in Figure 3.3 by employing the grid-based ECS numerical methods described in 3.3.2. Tunneling lifetimes of 16.7 ps and 110 fs are obtained for the v=0 and v=1 levels, respectively. These lifetimes are notoriously difficult to calculate using *ab initio* methods, because, as explained by Tanaka and Yoshimine [67], they depend sensitively on the details of the shallow well that arises from an avoided crossing with other $^4\Sigma_u^-$ states. By treating motion on the coupled adiabatic potentials whose avoided crossing creates the barrier shown in Figure 3.1, Demekhin *et al*. [77] calculated lifetimes of 12.2 ps and 67.7 fs for these two vibrational levels, in reasonable agreement with our *ab initio* values. Experimental measurements of the tunneling lifetime of the v=0 level vary from 0.27 ps [57] to 12 ps from the photoelectron spectroscopy and time-of-flight measurements of Codling *et al.* [111]. The lifetime of the v=1 level of the O_2^+ $c\ ^4\Sigma_u^-$ state in our calculations is in reasonably good agreement with the values of 67 and 100 fs from the measurements of Evans *et al.* [57] and Codling *et al* [111], respectively.

The coupled vibrational and autoionization dynamics on the *3s* Rydberg state potential that lead to the observed lifetimes of the v=0 and v=1 levels of that state are summarized in Figure 3.6. The Fano profiles of the autoionizing feature corresponding to the *3s* state in the photoionization calculations give both the electronic autoionization width at each internuclear distance and the position of the resonance relative to its parent ionic $c\ ^4\Sigma_u^-$ state. That potential curve, shown in Figure 3.6(a) almost parallels the parent ion curve, but not quite, in part because the *3s* resonant state is perturbed when two ionic potential energy curves, which are the energetic thresholds for autoionization to produce those ion states, intersect it at different values of *R* in the well that binds the two vibrational levels. Those two ionic states are the $1\ ^4\Pi_g$ and $B\ ^2\Sigma_g^-$ states that are dominated by the configurations $1\sigma_g^2 1\sigma_u^2 2\sigma_g^2 2\sigma_u^2 3\sigma_g^2 1\pi_u^2 1\pi_g^3$ and $1\sigma_g^2 1\sigma_u^2 2\sigma_g^2 2\sigma_u^2 3\sigma_g^1 1\pi_u^4 1\pi_g^2$, respectively. Faint undulations and an alteration of the depth of the well change the tunneling lifetimes in the absence of autoionization. We calculate tunneling lifetimes to be 63.0 ps and 170 fs for the v=0 and v=1 levels of the *3s* Rydberg state, respectively. They are thus somewhat different from the tunneling lifetimes calculated by the same means for the parent ion state, but the differences are not surprising if we keep in mind the semiclassical picture that tunneling probabilities depend exponentially on small changes in the potential [112].

More striking in both Figures 3.3 and 3.6 is the strong structure in the width of the *3s* Rydberg Fano resonance feature as a function of internuclear distance. As each of the two thresholds (the $1\ ^4\Pi_g$ and $B\ ^2\Sigma_g^-$ states of O_2^+) shown in Figure 3.3 pass through the *3s* state with increasing internuclear distance, an autoionization decay channel opens, and the competition between the changing decay pathways alters the total ionization width. How the variation in the total electronic autoionization width affects the vibrational states depends on the structure of the vibrational wave functions in this critical region. Those wave functions are also shown in Figure 3.6, and their extension to large R outside the tunneling barrier is an indication of the tunneling probability. The fits to the calculated width shown in Figures 3.3 and 3.6 are extended outside the well, but none of the calculated results depend (to five significant figures) on the width outside the well. Inside the well the story is very different.

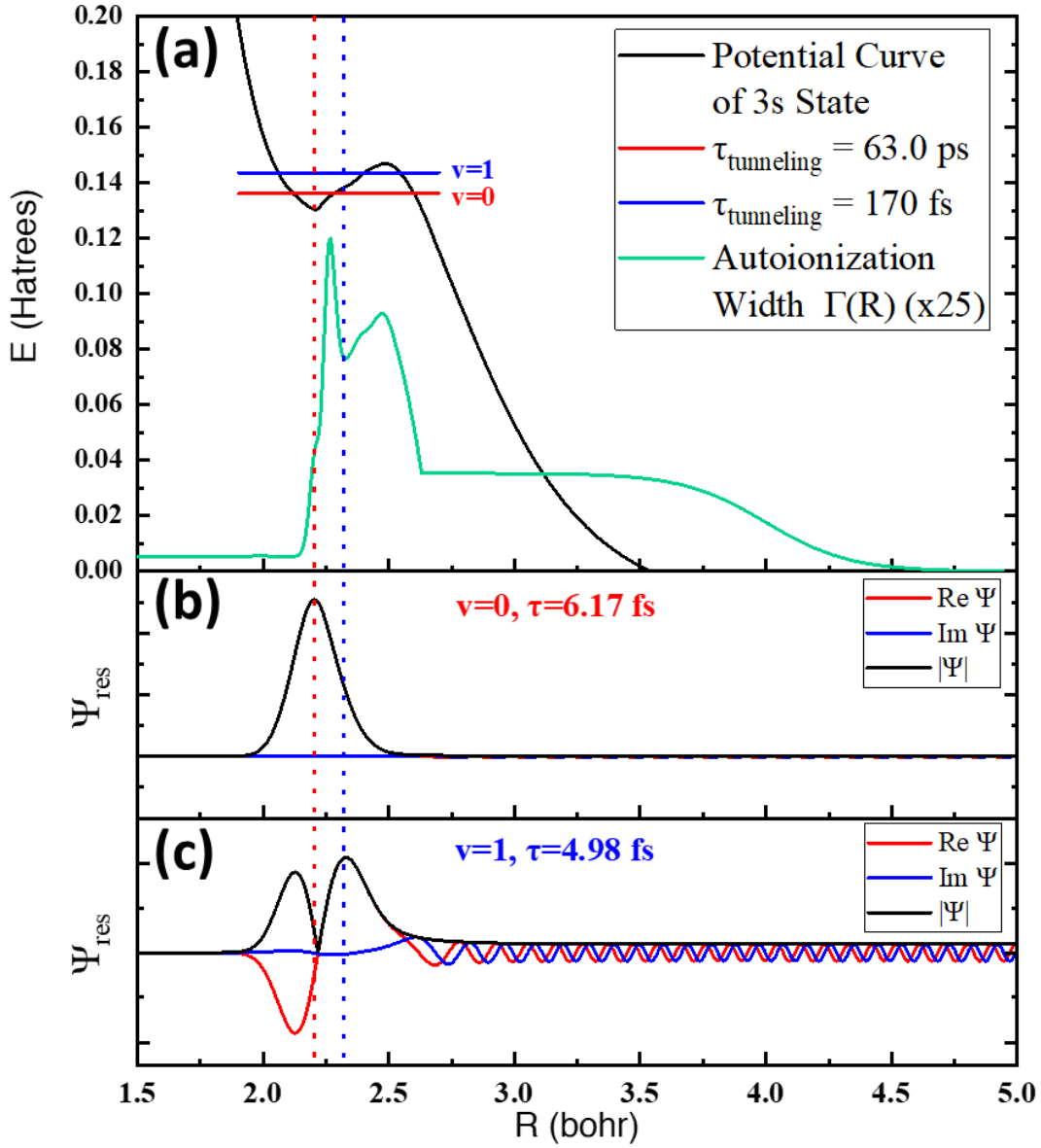

Figure 3.6 Vibrational dynamics on the calculated 3s Rydberg potential curve whose imaginary part is given by the R-dependent electronic autoionization width in the local complex potential, $E_{res}(R) - i\Gamma(R)/2$. (a) Potential curve $E_{res}(R)$, width $\Gamma(R)$, and location of tunneling vibrational levels, (b) the v=0 vibrational wave function, and (c) the v=1 vibrational wave function showing tunneling into the dissociative region of the potential. Red and blue vertical dash lines mark the location of the maxima in the absolute value of the vibrational wave functions of v=0 and v=1, respectively.

3.5 Discussion

The initial calculation of the lifetimes of the states using this local complex potential gave lifetimes of 4.67 and 4.93 fs for the v=0 and v=1 levels of the *3s* Rydberg state, respectively, retaining several significant figures, giving the opposite trend from the experimental values of 5.8 and 4.5 fs. However, the calculated lifetimes are dramatically sensitive to the details of the electronic autoionization width appearing in Equation (3.3) as the imaginary part of the local complex potential. Shifting the width curve to larger values of R by only 0.03 Bohr (hardly the width of the line in Figure 3.6 produces lifetimes of 6.17 fs and 4.98 fs for the v=0 and v=1 levels, thereby reproducing the experimental trend of a shorter v=1 lifetime. Moreover, both values lie within the error bars of the experimental lifetimes.

The reason for this sensitivity to the variation of the electronic autoionization lifetime with internuclear distance is apparent in Figure 3.6. The wave functions of the two metastable vibrational states sample the variations in the autoionization probability quite differently. If we perform the computational experiment of shifting the calculated width function slightly to the right (to larger R by a few hundredths of a Bohr), the lifetime of the v=0 state increases quickly as the peak in $\Gamma(R)$ begins to move out of the range of R where the v=0 wave function is nonzero. The v=1 wave function extends over a larger range of R and its lifetime changes little for small shifts, but for larger shifts its lifetime increases more quickly. This computational test shows that the observed lifetime is extremely sensitive to the dependence of the autoionization probability on internuclear distance. This degree of sensitivity of the lifetimes of these metastable states makes their experimental observation a powerful test of all parts of their theoretical description.

It is important to note that neither of these two calculations can be reproduced with Equation (3.2) using the calculated tunneling lifetimes $\tau_d^{(\mathrm{v=0})}$= 63.0 ps and $\tau_d^{(\mathrm{v=1})}$= 170 fs for these states with any single value of the electronic autoionizing width $\tau_a^{(3s)}$, which suggests the simple picture of the assumption that the autoionization lifetime is independent of vibrational levels described by Equation (3.2) has broken down here. We can substitute the calculated overall and tunneling lifetimes into Equation (3.1) to find the autoionization lifetime at different vibrational levels as shown in Table 1. The autoionization lifetime decreases by about 20% from v=0 to v=1, which dominates most of the change in total lifetime.

These calculations are not of spectroscopic accuracy, of course, and we are unaware of any calculations of such accuracy for this difficult problem, either for the O_2^+ $c\ ^4\Sigma_u^-$ state or the Rydberg states converging to it. However, they do strongly suggest that the measurement of these lifetimes probes the dynamical coupling between internuclear separation and electronic autoionization, while the tunneling contribution to predissociation is a weak spectator to lifetime process. The combination of *ab initio* electronic structure and photoionization calculations and the experimental observations provide strong evidence that the electronic autoionization lifetime can change significantly with internuclear distance and thus different vibrational levels can have different autoionization lifetimes.

	Experimental	Theoretical		
	Lifetime	Lifetime	Autoionization	Predissociation
v=0	5.8±0.5 fs	6.17 fs	6.17 fs	63 ps
v=1	4.5±0.7 fs	4.98 fs	5.13 fs	170 fs
Difference	28.8±17.2 %	23.9%	20.0%	>100%

Table 3.1 Experimental and theoretical results on the lifetime of 3s Rydberg state.

3.6 Conclusions

We performed attosecond XUV wave-mixing spectroscopy on the short-lived *3s* Rydberg state, part of a series that converges to the O_2^+ $c\ ^4\Sigma_u^-$ state. The lifetimes of the v=0 and v=1 vibrational levels of the *3s* Rydberg state are measured to be 5.8±0.5 fs and 4.5±0.7 fs, respectively. Our time-domain measurements find that the lifetime of two different vibrational levels of the *3s* Rydberg state are significantly different from each other, and this difference cannot be explained by the change of the predissociation rate alone as proposed previously [59,78]. Instead, with the aid of the theoretical results described here, we find that more rapid electronic autoionization in the v=1 state contributes significantly to the decreased lifetime of this state. This effect is dramatically sensitive to the details of the dependence of the autoionization width on internuclear distance. The excellent agreement between experimental and calculated lifetimes provides strong evidence for this key theoretical result.

The work described herein is the first experiment performed with attosecond XUV wave-mixing spectroscopy to investigate the ultrafast decaying states in a molecule. We demonstrate the ability of attosecond XUV wave-mixing spectroscopy to probe dynamics on the few-fs timescale as well as the ability to probe the vibrationally resolved lifetimes in a molecule. Our theoretical calculations shed light on the interplay between the vibrational motion, tunneling, and the autoionization process which is strongly influenced by crossings with ionic states. This detailed understanding will lead to many possible applications of attosecond XUV wave-mixing spectroscopy in the future.

Chapter 4: State-Selective Probing of CO_2 Autoionizing Inner Valence Rydberg States with Attosecond Extreme Ultraviolet Four-Wave Mixing Spectroscopy

*The content and figures of this chapter are reprinted or adapted with permission from A. P. Fidler, Y.-C. Lin, J. D. Gaynor, C. W. McCurdy, S.R. Leone, R. R. Lucchese, D.M. Neumark, Phy. Rev. A **106**, 063525 (2022).*

4.1 Abstract

Nonlinear spectroscopies can disentangle spectra that are congested due to inhomogeneous broadening. In conjunction with theoretical calculations, attosecond extreme ultraviolet (XUV) four-wave mixing (FWM) spectroscopy is utilized here to probe the dynamics of autoionizing, inner valence excited Rydberg states of the polyatomic molecule, CO_2. This tabletop nonlinear technique employs a short attosecond XUV pulse train and two noncollinear, few-cycle near infrared pulses to generate background-free XUV wave-mixing signals. FWM emission is observed from the n = 5 – 7 states of the Henning sharp $nd\sigma_g$ Rydberg series that converges to the ionic $\tilde{B}\ ^2\Sigma_u^+$ state. However, these transient emission signals decay with lifetimes of 33 ± 6 fs, 53 ± 2 fs, and 94 ± 2 fs, respectively, which calculations show are consistent with the lifetimes of the short-lived n = 6 – 8 members of the $ns\sigma_g$ character Henning diffuse Rydberg series. The oscillator strengths of transitions between states involved in all possible resonant FWM processes are calculated, verifying that the nonlinear spectra are dominated by pathways described by an initial excitation to the diffuse $ns\sigma_g$ Rydberg series and emission from the sharp $nd\sigma_g$ Rydberg series. The results substantiate not only that attosecond XUV FWM spectroscopy produces rigorous and meaningful measurements of ultrafast dynamics in polyatomic systems, but also that nonlinear spectroscopic techniques are versatile tools to selectively probe dynamics that are otherwise difficult to access.

4.2 Introduction

Nonlinear spectroscopies are exceptionally powerful tools that can elucidate complex structure and dynamics in chemical systems. In these techniques, multiple short coherent light pulses interact with matter to generate a higher order polarization response [24,113]. While linear spectroscopy has been effectively employed to provide energetic and structural information, the remarkable versatility of nonlinear methods originates from experimental control over the frequency, intensity, beam geometry, and sequence of each of the incoming pulses. These additional degrees of freedom allow for highly selective measurements in both the frequency and time domains, permitting diverse applications such as probing structure and dynamics in complex chemical systems [1-3], disentangling homogenous and inhomogeneous line widths [114], and modifying the spectral bandwidth of light sources [115,116]. The extension of nonlinear spectroscopies into the extreme ultraviolet (XUV) and x-ray spectral regions will enable experiments that investigate short-

lived and element-specific inner-valence and core-excited states with greater spatial and temporal resolution [30-33], further expanding the frontiers of these important techniques.

The development of high harmonic generation (HHG) [4,5] over the past three decades has resulted in accessible table-top coherent XUV sources with subfemtosecond pulse durations [117]. The extremely short time resolution of these attosecond light sources not only permits direct time-domain measurements of electronic dynamics in atomic [118-120], molecular [8,121,122], and solid-state systems [123-125], but also provides the foundation for tabletop versions of XUV nonlinear spectroscopy. A recently developed extension of these techniques [6,7], attosecond XUV four-wave mixing (FWM) spectroscopy, utilizes a short attosecond XUV pulse train produced by HHG and two noncollinear near-infrared (NIR) pulses to generate spatially-isolated third order polarization signals. These transient emission signals encode the evolution of excited states and represent background-free measurements of XUV-induced chemical dynamics [11,14,15]. This technique has already been applied to monitor electronic and vibronic coherences in multiple atomic and diatomic systems [6-8], facilitating the characterization of a previously inaccessible dark state in N_2 [9], the detection of light-induced states in He [13], and the implementation of a variant of XUV multidimensional spectroscopy in long-lived Rydberg states of Ar [10]. Moreover, attosecond wave-mixing experiments have revealed order-dependent emission delays in nonlinear signal generation [12] and measured ultrafast dynamics due to autoionization and Auger decay in atomic [11], diatomic [14], and solid-state systems [15]. Here, we extend attosecond XUV FWM spectroscopy to probe autoionization dynamics in a polyatomic system, the inner valence Rydberg states of carbon dioxide.

As a linear triatomic, centrosymmetric molecule composed of only second row elements, CO_2 is one of the simplest polyatomic systems. CO_2 attracts considerable interest from molecular spectroscopists and the broader scientific community as a well-known greenhouse gas with notable impacts on climate [126]. Of particular relevance to the current work, the electronic structure of CO_2 and its low-lying ionic states have been characterized by photoabsorption, photoionization, and photoelectron spectroscopy [127-135].The lowest four ionic states of CO_2 are the $\tilde{X}\ ^2\Pi_g$, $\tilde{A}\ ^2\Pi_u$, $\tilde{B}\ ^2\Sigma_u^+$, and $\tilde{C}\ ^2\Sigma_g^+$ states reached by ionization energies of 13.778 eV, 17.314 eV, 18.077 eV, and 19.394 eV, respectively. In our experiment, an XUV pulse predominantly excites CO_2 into neutral Rydberg states located between 17.3 – 18.1 eV. An energy level diagram depicting the XUV-excited states relevant to this experiment is provided in Figure 4.1. This spectral region of CO_2 contains contributions from the Henning diffuse and Henning sharp series, both of which converge to the ionic $\tilde{B}\ ^2\Sigma_u^+$ threshold, as well as the Tanaka-Ogawa series, which converges to the ionic $\tilde{A}\ ^2\Pi_u$ threshold [131,132,134]. The two Henning series dominate the photoabsorption spectrum as contributions from the Tanaka-Ogawa series are limited to members with both high n and ν_1 quantum numbers in the spectral region above the $\tilde{A}\ ^2\Pi_u$ limit examined here. Complementary experiments by Sandhu and co-workers probing the dynamics of the Tanaka-Ogawa series are currently underway .

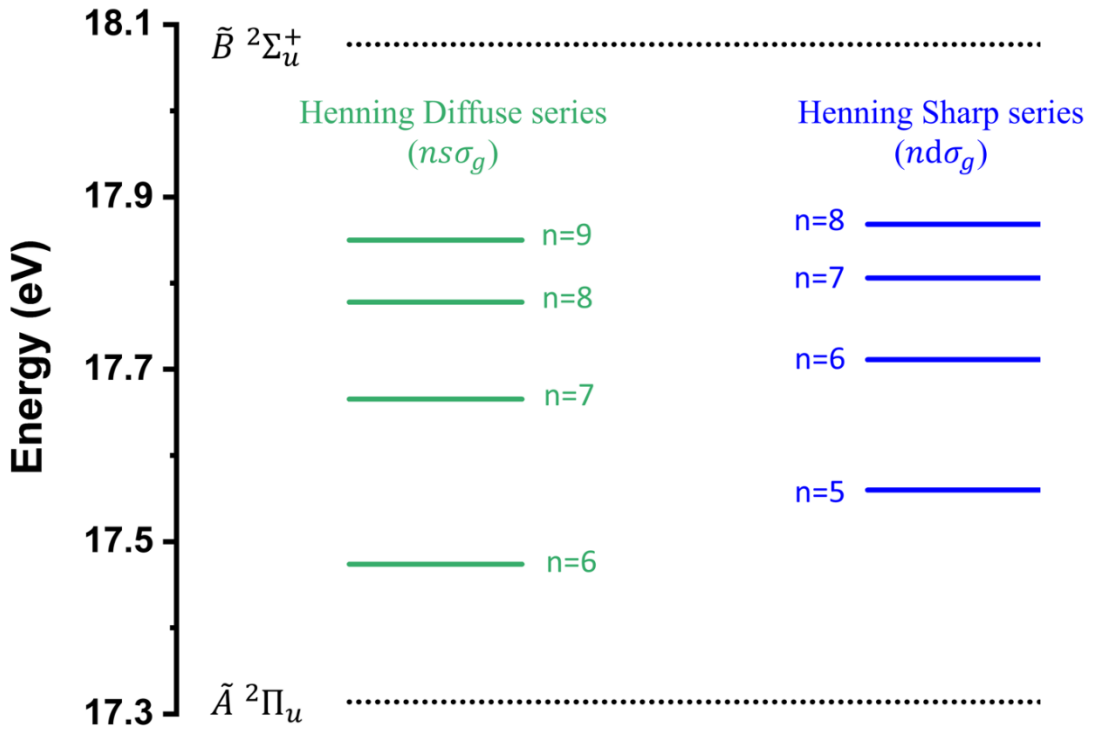

Figure 4.1 Energy level diagram of the Henning diffuse (green) and Henning sharp (blue) Rydberg series of CO_2 between 17.3-18.1 eV. Dotted lines represent ionic states while solid lines represent neutral Rydberg states. Both the $ns\sigma_g$ character Henning diffuse and $nd\sigma_g$ character Henning sharp series converge to the ionic $\tilde{B}\ ^2\Sigma_u^+$ state.

The Henning diffuse and Henning sharp series are assigned Rydberg electron characters of $ns\sigma_g$ and $nd\sigma_g$, respectively. While weak transitions to the $\nu_1 = 1$ symmetric stretch have been observed in the photoabsorption spectra, the $\nu_1 = 0$ transition dominates [127]. Photoionization quantum efficiency measurements provide insight into the channels relevant in the decay dynamics of these series [132]. For the Henning diffuse series, the photoionization quantum efficiency is close to unity, indicating that autoionization is the dominant decay pathway for this series. On the other hand, in the same work, the photoionization quantum efficiency of the Henning sharp series is notably less than unity, possibly reflecting competition between neutral predissociation and autoionization. While these photoionization measurements and the spectral linewidths of the states suggest that members of the Henning diffuse series decay more quickly than those of the Henning sharp series, more work is necessary to establish the lifetimes of these states.

In this joint experimental-theoretical work, we utilize attosecond FWM spectroscopy to investigate the ultrafast decay dynamics of autoionizing Rydberg states of CO_2. Spatially isolated FWM emission signals are primarily observed at energies associated with members of the Henning sharp series between 17.3 – 18.1 eV. However, transient measurements, supported by theoretical calculations of autoionization lifetimes, reveal that these emission signals report on the dynamics of members of the shorter-lived Henning diffuse series instead. Specifically, the experimentally measured decays of 33 $\pm$

6 fs, 53 ± 2 fs, and 94 ± 2 fs correspond well to the lifetimes of the n = 6 – 8 Henning diffuse states calculated here. The interpretation of this counterintuitive result is facilitated by calculating oscillator strengths for transitions between states that may participate in the various resonant wave-mixing schemes. These calculations indicate that, due to substantial ground-to-diffuse state and dark-to-sharp state oscillator strengths, wave-mixing pathways dominate that probe the Henning diffuse states but emit from members of the Henning sharp series, as observed experimentally. This attosecond XUV FWM experiment demonstrates that transient wave-mixing can be successfully utilized to monitor ultrafast decay in polyatomic molecules with high selectivity.

4.3 Methods

4.3.1 Experimental Methods

The experimental apparatus utilized to generate and measure XUV emission signals has been described previously [9,11,12,14,15] and is depicted in Figure 4.2 (a). Briefly, a commercial multipass Ti:Sapphire laser system (Femtopower HE, Femtolasers) produces 2 mJ of 22 fs NIR pulses with a central wavelength of 780 nm at a 1 kHz repetition rate. These pulses are spectrally broadened in a stretched 2 m long, 500 μm inner diameter hollow core fiber (Few-Cycle Inc.) statically filled with 2 bar of neon gas. The broadband fiber output is then temporally recompressed by seven pairs of double-angle chirped mirrors (PC70, Ultrafast Innovations) and a 2 mm thick ammonium dihydrogen phosphate (ADP) crystal [48], resulting in 600 μJ, 6 fs pulses with a spectral profile spanning from 550 – 950 nm (Figure 4.2 (b)). A 75:25 (T:R) beamsplitter divides the compressed NIR pulses into two arms. The transmitted portion of the beam is focused by a spherical silver mirror (f = 50 cm) through 300 μm holes drilled into a 1-mm pathlength cell contained within a vacuum chamber at 10^{-6} Torr. The interaction of the focused NIR driver (~10^{14} W cm^{-2}) with xenon gas flowing through the cell produces XUV harmonics via high harmonic generation (HHG). The pressure of xenon gas (~5 Torr) flowing through the cell and its position relative to the few-cycle NIR driver pulse focus are optimized to generate a train of 2 – 3 subfemtosecond XUV pulses with photon energies that cover the neutral Rydberg states of CO_2 located between 17.3 – 18.1 eV (Figure 4.2 (c)). A 0.15 μm thick Al foil (Lebow) filters out the co-propagating NIR driver before the transmitted XUV pulse train is focused by a gold-coated toroidal mirror (f = 50 cm, ARW Optical Corporation) through an annular mirror into a 1-mm pathlength target cell. Small 500 μm diameter holes drilled into the target cell permit the XUV light to interact with the CO_2 gas flowing continuously though the cell. At the target cell, the XUV beam has an estimated waist of ~20 μm and a peak intensity of the order of 10^8 – 10^{10} W cm^{-2} due to the low conversion efficiency of HHG [136].

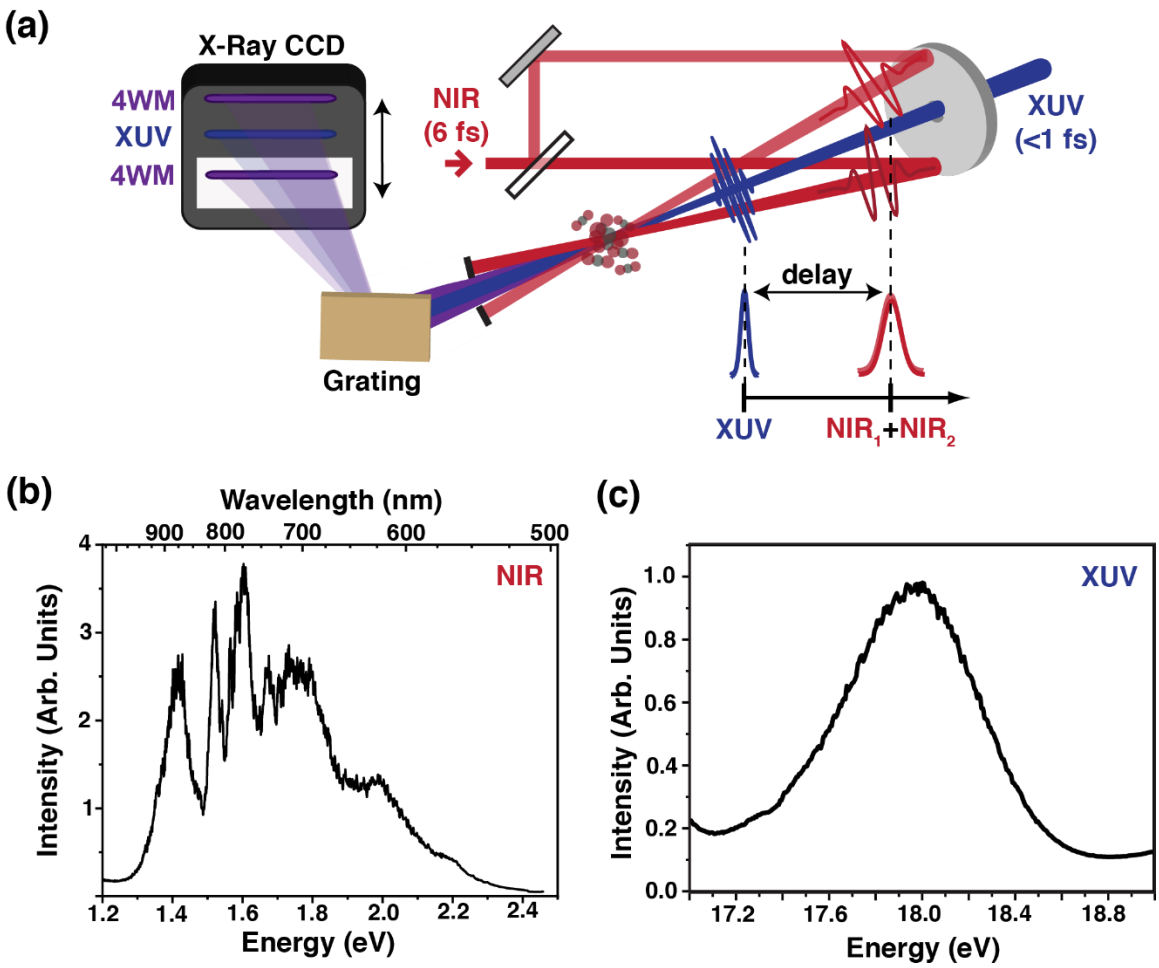

Figure 4.2 Attosecond extreme ultraviolet (XUV) four-wave mixing (FWM) spectroscopy. (a) Subfemtosecond XUV pulses at ~18 eV produced via high harmonic generation and two few-femtosecond (780 nm) NIR pulses are utilized to generate XUV wave-mixing emission signals from Rydberg states in gas-phase carbon dioxide. (b) Spectrum of NIR pulse. (c) Spectrum of XUV pulse.

The few-cycle NIR pulses reflected by the 75:25 beamsplitter are delayed relative to the XUV pulse train by a piezo-electric stage (P-622 with E509 controller, Physik Instrumente (PI)) and then split into two distinct NIR arms by a 50:50 beamsplitter. Two spherical mirrors (f = 1 m) direct each of the split beams into the vacuum chamber to positions above and below a 3 mm hole in the annular mirror through which the XUV pulse train passes. The focused upper and lower NIR beams intersect with the XUV in the target cell at angles of approximately 18 mrad (1.0°). To ensure that the NIR pulses arrive at the target simultaneously, the pathlength of the lower NIR arm is adjusted with a second piezo-electric stage. Temporal and spatial overlap between the XUV and NIR arms is determined via second harmonic generation in a BBO crystal. Specifically, the Al foil that blocks the co-propagating NIR after HHG is removed and a mirror is inserted after the annular mirror, steering all three beams out of the vacuum chamber to a BBO crystal located at the focus of the NIR driver. At overlap, second harmonic signals emit at phase-matching angles

intermediate between each of the noncollinear NIR beams.

After passing through the target cell, the XUV harmonics and any generated nonlinear XUV emission signals transit through a slit that blocks the angled NIR beams. Residual NIR contamination is further attenuated by a second 0.15 μm Al filter before the transmitted XUV light is spectrally dispersed by a gold-coated flat-field grating (001-0639, Hitachi). An X-ray CCD camera (Pixis XO 400B, Princeton Instruments) records the target-attenuated harmonics and wave-mixing emission signals on a 1340 × 400 pixel array as a function of XUV photon energy and phase-matched divergence angle relative to the harmonic axis. The horizontal energy axis is calibrated by comparing wave-mixing emission from the $2s^2 2p^5 nl$ excitations of neon gas to atomic line transition data available from the National Institute of Standards and Technology (NIST). In these experiments, a homebuilt mount translates the camera vertically such that the harmonics no longer impinge on the CCD chip and only wave-mixing signals that emit at non-zero divergence angles are recorded. This spatial masking procedure is performed to reduce interference from artifacts induced by strong absorption features, allowing the weaker wave-mixing emission signals to be imaged cleanly.

CCD camera images are collected as a function of XUV-NIR delay, where positive delays are defined to indicate that the XUV pulse train precedes the time coincident NIR pulses. Three datasets are collected under different experimental conditions to establish the reproducibility of measured decay times. These conditions are summarized in Section 3.7.1. To enhance the relatively weak wave-mixing emission signals, all emission data are plotted in absorbance (A) (negative features):

$$A = -\log_{10}(I_{\text{NIR ON}}/I_{\text{NIR OFF}}) \tag{4.1}$$

where $I_{\text{NIR ON}}$ and $I_{\text{NIR OFF}}$ represent the signal collected by the CCD camera with all three beams impinging on the target and with both NIR pulses blocked by a mechanical shutter (Thorlabs), respectively. All subsequent data analysis was performed in Matlab.

4.3.2 Theoretical Methods

Theoretical results in this Chapter are supported by Dr. Robert R. Lucchese and Dr. C. William McCurdy in the AMOS program at LBNL. To explore the autoionization lifetimes of the Henning diffuse and Henning sharp Rydberg series in CO_2, we performed photoionization calculations very similar to those reported in Ref.[14] at the equilibrium geometry of the CO_2 molecule. We employed the multichannel Schwinger configuration interaction (MCSCI) variational method [94,95], which has been previously used to study the photoionization of CO_2 [137,138]. In these calculations, the final-state fixed-energy photoelectron wave functions were represented on a single-center expanded grid, with $l_{\max} = 100$, that terminated at $r_{\max} = 60$ Å, which was large enough to describe a number of Rydberg states below each ionization threshold. The full N-electron ionized state was represented as a close-coupling expansion containing a sum of the products of (N - 1)-electron ion state wave functions with one-electron photoelectron continuum wave functions. The ion channels used in the close coupling calculation included the four valence ion states, $\left(1\pi_g\right)^{-1}\ \tilde{X}\ ^2\Pi_g$, $(1\pi_u)^{-1}\ \tilde{A}\ ^2\Pi_u$, $(3\sigma_u)^{-1}\ \tilde{B}\ ^2\Sigma_u^+$, and $\left(4\sigma_g\right)^{-1}\ \tilde{C}\ ^2\Sigma_g^+$. The calculations were performed with the bond length $R_{\text{C-O}}$ = 1.1621 Å [139]. The bound state

orbitals were computed using an aug-cc-pVTZ basis [99,100] using MOLPRO [101] with a valence complete-active-space self-consistent field (VCASSCF) description of the ground state keeping the C(1s) and O(1s) core orbitals doubly occupied in all configuration state functions. In the photoionization calculation, the initial state was represented by a configuration interaction wave function with the three core orbitals doubly occupied and including up to quadrupole excitation into the weakly occupied orbitals from the VCASSCF calculation. The initial $^1\Sigma_g^+$ state used to compute the dipole matrix elements was then obtained using triple excitations into the weakly occupied orbitals. In the scattering calculations, the ionization potentials for the four ion states were adjusted to agree with experimental values of 13.78 eV, 17.31 eV, 18.08 eV, and 19.39 eV for the $\tilde{X}$, $\tilde{A}$, $\tilde{B}$, and $\tilde{C}$ states, respectively [130]. The resulting cross sections contained a number of autoionizing resonance structures, which were analyzed by fitting the line shapes to Fano profiles [36] to extract the position and the width of each autoionization resonance.

Additionally, we located the position of an optically dark autoionizing state of symmetry $^1\Sigma_g^+$ that cannot be reached by a one-photon transition from the ground state and has a computed energy that is 15.8 eV above the ground state. To assess the extent to which this state could contribute to the FWM process, we then computed the oscillator strengths for transitions from this state to the bright Rydberg autoionizing states and the oscillator strengths from the ground state to the same bright states. These oscillator strengths were obtained using a purely bound state calculation, which was performed with the same MCSCI code that was used in the scattering calculations. In these calculations, we extended the aug-cc-pVTZ basis set used in the main scattering calculations with a set of Rydberg-like Gaussian basis functions of Kaufmann *et al.* [140] as defined by Equation (18) of that paper. The added Gaussian functions had $l = 0$ with $n = 1.5, 2.0, \ldots, 6.0$, $l = 1$ with $n = 2.0, 2.5, \ldots, 4.0$, and $l = 2$ with $n = 2.5, 3.0, \ldots, 7.0$, where these 25 added functions all had σ symmetry.

4.4 Results

4.4.1 Spatially Isolated Wave-Mixing Emission in Carbon Dioxide

The XUV pulse train generates a coherence of autoionizing Rydberg states of carbon dioxide spanning 17.3 – 18.1 eV, including members of the Henning diffuse and Henning sharp series [132,134]. This coherence is probed by two time-coincident, noncollinear NIR pulses, resulting in transient wave-mixing signals that emit at a spatial location distinct from the XUV harmonics dictated by wavevector phase matching conditions (Figure. 4.3 (a)). For a FWM process requiring both NIR beams, the wave-mixing signals will emit at a divergence angle (ϕ_{div}) described by the following expression[9,11,15]:

$$\phi_{\text{div}} \approx \frac{\upsilon_{\text{NIR1}}\theta_{\text{NIR1}} + \upsilon_{\text{NIR2}}\theta_{\text{NIR2}}}{\upsilon_{\text{XUV}}} \tag{4.2}$$

where υ_{NIR1} and υ_{NIR2} are the frequencies of the NIR photons involved in the wave-mixing pathway, θ_{NIR1} and θ_{NIR2} are the crossing angles at which the NIR beams intersect the XUV in the target cell, and υ_{XUV} is the frequency of the initial XUV excitation. Multiple wave-mixing pathways composed of photons of different frequencies can emit at the same

energy, augmenting the angular divergence of the wave-mixing signals [14]. However, the intensity of emission is enhanced when each photon involved in the wave-mixing process is resonant with a transition in the medium [141,142], resulting in a preference for pathways mediated by one-photon, dipole forbidden (dark) states. Two NIR photons couple one photon, dipole allowed (bright) states via dark states, leading to the emission of XUV photons at the energies of the Rydberg states observed in the photoabsorption spectrum. Calculations described in Section 4.3.2 suggest that the viable intermediary dark states are located below the emitting state in energy, as depicted in Figure 4.3 (a).

A representative photon energy-calibrated CCD camera image taken at temporal overlap of all three pulses is shown in Figure 4.3 (b). The negative absorbance features (blue) observed in the camera image indicate the generation of new XUV light due to wave-mixing emission. The spatial dimension of the camera image is plotted as a function of the angle of divergence relative to the harmonics, which have been translated off of the CCD chip to minimize interreference from on-axis (0 mrad) signals. Note that wave-mixing pathways that incorporate two, time-coincident NIR pulses can emit at both negative and positive divergence angles, depending on the arbitrarily assigned NIR pulse order. Although discrete emission lines can be discerned as a function of photon energy, the wave-mixing features are broad in divergence angle. The angular divergence of these wave-mixing features (Figure 4.3 (b)) primarily reflects the angular spread of the incident XUV beam, but the divergence also may be broadened to lesser extent by additional FWM pathways that emit at similar energies.

In Figure 4.3 (c), a spectral trace of the wave-mixing emission shown in Figure 4.3 (b) is obtained by integrating over the negative absorbance features in the angular range of 2.7 – 5.8 mrad. The most prominent features arise at energies associated with members of the Henning sharp series with principal quantum numbers from $n = 5$ to $n = 8$. Weaker features mirroring these strong wave-mixing signals at slightly lower photon energies appear to emit at the energies of the Henning diffuse series. While emission from the lowest member of the Henning diffuse series ($n = 6$) can be distinguished from the nearby Henning sharp series feature ($n = 5$), the spectral resolution of the apparatus is insufficient to resolve the majority of adjacent Henning diffuse and sharp emission features, particularly as the states become more finely spaced in the approach to the ionization threshold (IP). Consequently, the wave-mixing emission features reported here exhibit broader spectral linewidths than would be expected for members of the Henning sharp series alone given previous synchrotron measurements [132].

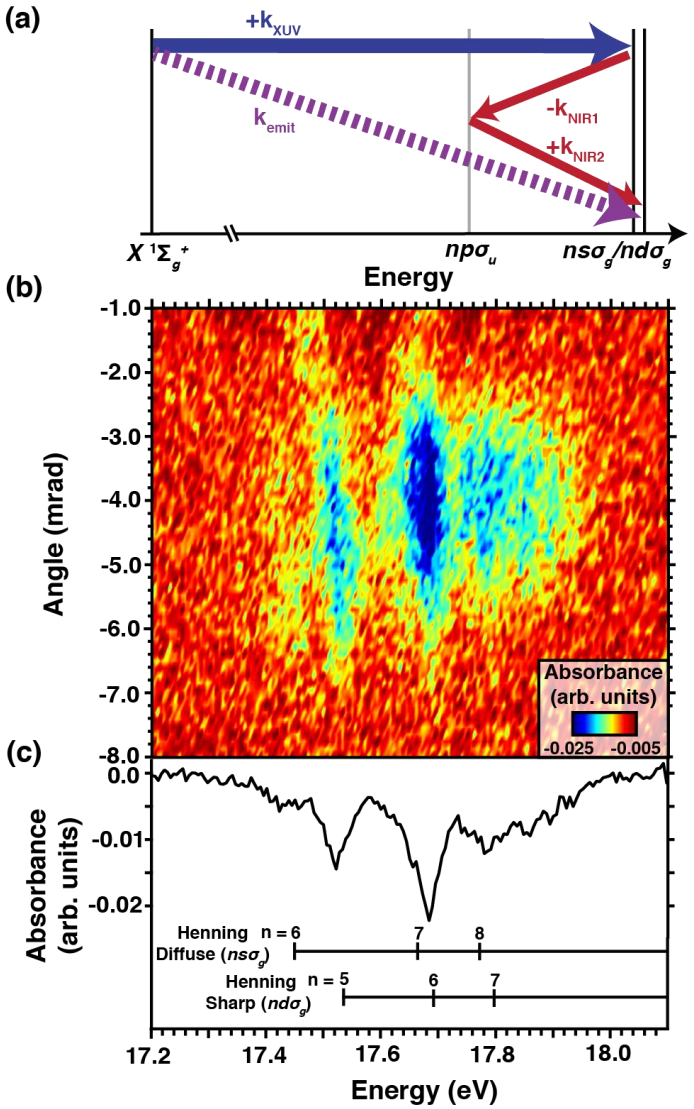

Figure 4.3 Background-free wave-mixing signals are detected by an X-ray CCD camera at spatial and temporal overlap of all three pulses. (a) A wavevector phase-matching diagram demonstrating the generation of spatially isolated four wave mixing signals (dashed, purple arrow) from an XUV pulse train (thick, blue arrow) and two NIR pulses (thin, red arrows). Not to scale. (b) An X-ray charge coupled device (CCD) image plotted as a function of photon energy and phase-matching divergence angle reveals multiple wave-mixing emission features (blue). (c). An angle-integrated trace taken from this camera image can be compared to literature photoabsorption spectra for spectral assignment. The observed emission features correspond primarily to Rydberg series that converge to the ionic $\tilde{B}\ ^2\Sigma_u^+$ limit, with the Henning sharp series representing the dominant contribution.

4.4.2 Ultrafast Dynamics of Autoionizing Rydberg States

The XUV-induced coherent superposition decays with the dephasing time, or polarization lifetime, of the constituent Rydberg states [11]. The temporal evolution of the XUV-induced Rydberg state coherence can be monitored by plotting angle-integrated wave-mixing signals as a function of the delay between the XUV and time coincident NIR pulses. Figure 4.4 provides a false color plot depicting the emission features in Figure 4.3 (c) as a function of both photon energy and XUV-NIR delay. As in the CCD camera image (Figure 4.3 (b)), wave-mixing signals appear as negative absorbance features at energies associated with Rydberg state resonances. These emission signals exhibit both appreciable decays and oscillations indicative of the XUV-induced coherence within the few hundred femtosecond time period investigated in this experiment. As in previous transient wave-mixing experiments the probed manifolds of autoionizing states [11], the duration of the wave-mixing signals increases with photon energy of emission state, reminiscent of the well-known $(n^*)^3$ trend for autoionizing state lifetimes [11,143].

To assess the timescales of the wave-mixing decays, the emission signals are integrated over a narrow energy window corresponding to the Henning sharp states and fit to a convolution of the instrumental response and an exponential decay using a least squares algorithm (Figure 4.5). The application of this fitting procedure to three different datasets (Section 3.7.2) yields decays of 33 ± 6 fs, 53 ± 2 fs, and 94 ± 2 fs for the features emitting from the $n = 5$, $n = 6$, and $n = 7$ members of the Henning sharp series, respectively. Integrating over smaller angular regions of Figure 4.3 (b) does not change the extracted decays appreciably. As expected, these time constants reflect the proportional increase in autoionizing state lifetime with $(n^*)^3$ [143]. However, these measured decays are not consistent with the calculated lifetimes of Henning sharp series, which will be shown in Section 4.4.3 to decay on timescales more than an order of magnitude longer than observed here. The decay of the wave-mixing emission instead corresponds to lifetimes of Henning diffuse series, as discussed further in the following sections.

Oscillations have been observed in similar XUV wave-mixing experiments investigating both atomic [10,11,13] and molecular systems [8,9]. Here, wave-mixing oscillations are most pronounced in the short-lived features emitting from lower lying members of the Henning sharp series. A Fourier transform taken along the delay axis of the transient wave-mixing spectrum shown in Figure 4.4 reveals frequency components at energies associated with wave-mixing emission (Figure 4.6 (a)). Although broad, the dominant frequency components in the Fourier spectra roughly correspond to energy differences between members of the Rydberg series that comprise the initial XUV-induced coherent superposition of states. The evolution of this coherence is probed by the time-coincident NIR pulses, which couple members of the coherence back to the Rydberg manifold via a resonant dark state, resulting in wave-mixing emission. The contribution of each member of the initial coherence to the emitted signal can be represented by a wave-mixing pathway. Multiple wave-mixing pathways can emit at the same energy, resulting in oscillations in the emission signal. As depicted in Figure 4.6 (b), the ~0.12 eV frequency feature obtained from the $n = 6$ Henning sharp emission signal appears to correspond to the energy difference between the $n = 7$ and $n = 8$ Henning diffuse states, both of which are members of the original XUV-induced coherence.

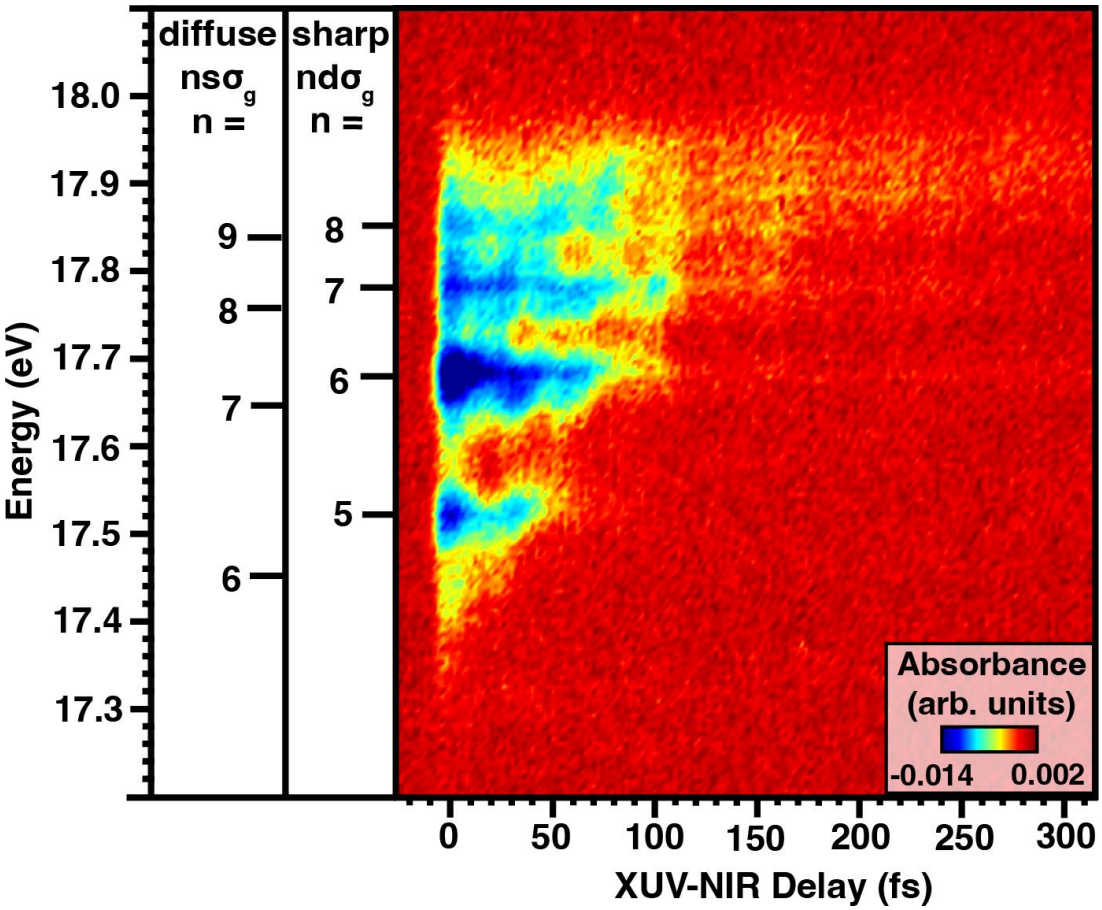

Figure 4.4 Wave-mixing signals are plotted as a function of photon energy and XUV-NIR delay, revealing both oscillatory features and emission state-dependent decays. State assignments are provided to the left of the figure. The decay times associated with the wave-mixing signals emitting from the Henning sharp series lengthen with increasing principal quantum number.

Note that wave-mixing pathways utilizing a Henning diffuse ($ns\sigma_u$) state cannot be distinguished from pathways involving the adjacent Henning sharp ($n'd\sigma_u$) state for the same interaction due the breadth of the Fourier features. Moreover, frequencies associated with coherences of adjacent $ns\sigma_u$ and $n'd\sigma_u$ states are expected to appear below 0.09 eV and thus cannot be positively identified. Unlike some previous measurements [11], unity slope lines are not apparent in the transformed spectrum, indicating that wave-mixing pathways composed of degenerate photons that couple the emitting state to itself do not dominate emission in this system.

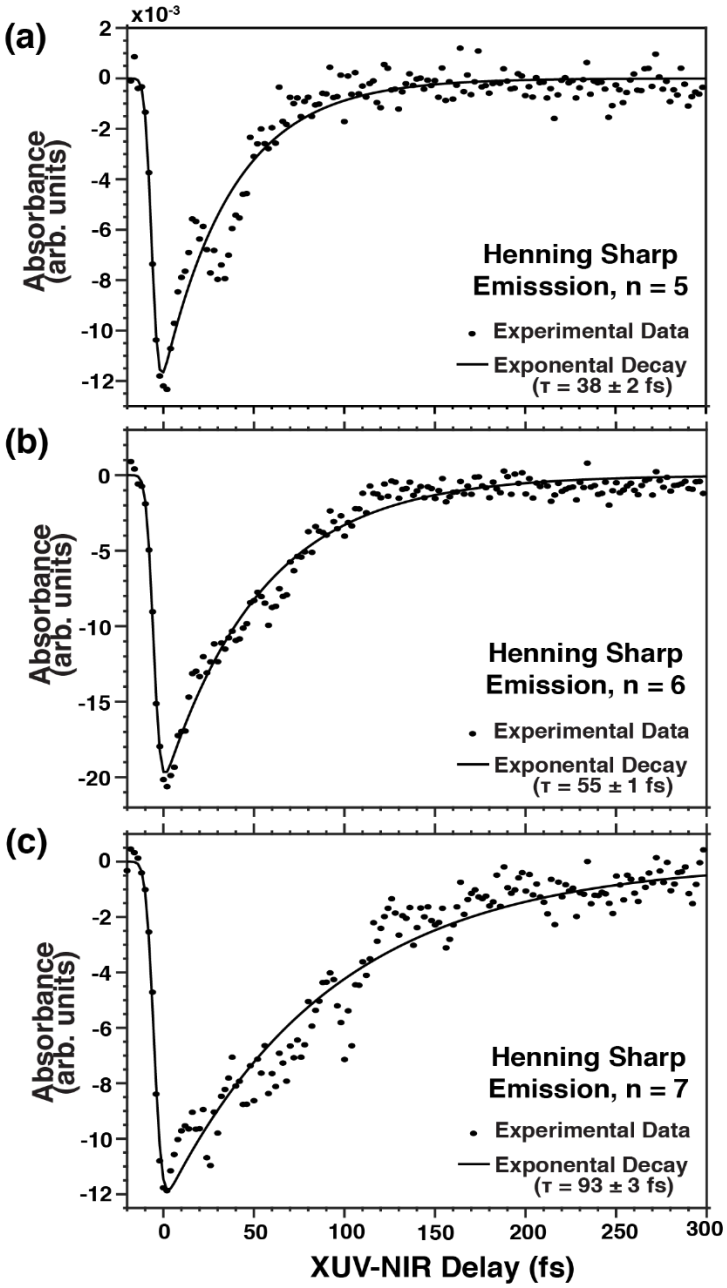

Figure 4.5 Wave-mixing signals exhibit emission state-dependent ultrafast decays. Lineouts taken at the energy positions of the Henning sharp a) n = 5 (17.50 – 17.53 eV), b) n = 6 (17.67 – 17.70 eV), and c) n = 7 (17.77 – 17.80 eV) states from a representative data set are fit with exponential decays, revealing decay constants that increase with principal quantum number. The dots in each of the panels represent measured experimental data while the solid lines are numerical fits. The time constants and error provided here correspond to the least squares fit of a single data set. The decay constants measured correspond with the lifetimes of the Henning diffuse states, not the sharp states from which they emit.

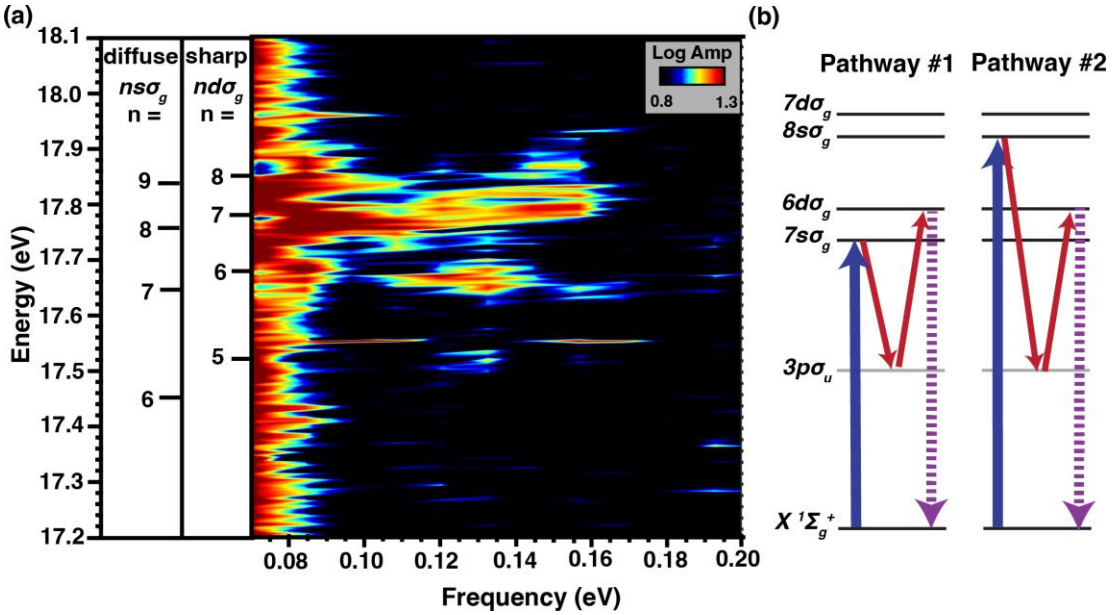

Figure 4.6 (a) Fourier analysis of the delay-dependent wave-mixing emission spectrum. State assignments are provided to the left of the spectrum. Broad frequency-domain features are observed at energies associated with the Henning sharp series. (b) Interference between wave-mixing pathways built on different Rydberg series members within the XUV bandwidth leads to oscillations with frequencies consistent with those measured in the Fourier transform in the wave-mixing emission spectrum. The NIR pulses are represented by thin, red arrows, while the XUV pulse and FWM emission are represented by thick blue and dashed purple arrows, respectively.

4.4.3 Theory Results

In the photon energy range interrogated directly by the FWM experiment, 17.5 eV to 17.9 eV above the ground state, the calculations of the photoionization cross sections found two series of Rydberg autoionizing resonances leading to the $\tilde{B}\ ^2\Sigma_u^+$ ionization threshold. The positions and widths extracted from the Fano profile analysis for these resonances are given in Table 4.1. The resonances in the diffuse $^1\Sigma_u^+[ns\sigma_u\ \tilde{B}\ ^2\Sigma_u^+]$ series and the sharp $^1\Sigma_u^+[nd\sigma_u\ \tilde{B}\ ^2\Sigma_u^+]$ series come in pairs with the diffuse state having quantum number *n* being very close to the sharp state with quantum number *n*-1 as is also seen in the synchrotron one-photon photoabsorption experiment [132]. In order to extract the Fano parameters for these resonances, we fit each pair of resonances independently of the other pairs. We then assumed that the fit of the Fano profile for a given pair had a common non-resonant background term, which was quadratic in the photon energy, and we further assumed that the contributions of the photoionization cross sections of the two resonances of a given pair were additive. The position and width of the $^1\Sigma_g^+[3p\sigma_u\tilde{B}\ ^2\Sigma_u^+]$ dark state is also given in Table 4.1. We can see that the lifetimes of these autoionizing Rydberg states are strongly affected by the orbital angular momentum, with the $d\sigma_g$ being much longer lived than the $s\sigma_g$ at approximately the same energy. The $p\sigma_u$ state has an intermediate lifetime, although the specific state given with $n = 3$ would be expected to have a shorter

lifetime than the corresponding $p\sigma_u$ states with higher values of *n* which have energies that are closer to the $s\sigma_g$ and $d\sigma_g$ states considered here.

The oscillator strengths computed using only the extended basis set calculation between the ground, diffuse, sharp, and dark states are given in Table 4.2. The main trend seen here is that the oscillator strengths for going from the ground state to the diffuse states are consistently larger than the transitions from the ground states to the sharp states at a similar energy. The transitions from the dark state to the sharp and diffuse states have the opposite trend, with the transitions to the sharp states being stronger than the corresponding transitions to the diffuse states.

	n	**Width (eV)**	**E (eV)**	**Calculated Lifetime (fs)**	**Experimental lifetime (fs)**
Diffuse	6	0.02064	17.4738	31.9	33 ± 6
$^1\Sigma_u^+[ns\sigma_u\tilde{B}\ ^2\Sigma_u^+]$	7	0.01128	17.6654	58.4	53 ± 2
	8	0.00760	17.7779	86.7	94 ± 2
Sharp	5	0.00177	17.5598	372.6	
$^1\Sigma_u^+[nd\sigma_u\tilde{B}\ ^2\Sigma_u^+]$	6	0.00045	17.7110	1457.5	
	7	0.00019	17.8059	3378.5	
Dark					
$^1\Sigma_g^+[np\sigma_u\tilde{B}\ ^2\Sigma_u^+]$	3	0.01210	15.7836	54.4	

Table 4.1 Calculations of linewidths and corresponding lifetimes of Henning diffuse and Henning sharp series for the n = 6 – 8 and n = 5 – 7 states, respectively, compared with experimentally measured lifetimes. Also, the computed data for the dark state is given.

	n	**E (eV)**	**XUV Oscillator Strength**	**NIR Resonant Energy (eV)**	**NIR Oscillator Strength to Dark State**
Diffuse	6	17.4738	0.020407	1.6738	0.000428
$^1\Sigma_u^+[ns\sigma_u\tilde{B}\ ^2\Sigma_u^+]$	7	17.6654	0.014138	1.8654	0.000007
	8	17.7779	0.009125	1.9779	0.00002
Sharp	5	17.5598	0.008243	1.7598	0.002355
$^1\Sigma_u^+[nd\sigma_u\tilde{B}\ ^2\Sigma_u^+]$	6	17.7110	0.001856	1.911	0.0001947
	7	17.8059	0.000745	2.0059	0.000044

Table 4.2 Calculations of the oscillator strength between ground states, Henning diffuse and sharp series, and the $^1\Sigma_g^+[3p\sigma_u\tilde{B}\ ^2\Sigma_u^+]$ *dark state located at 15.8 eV.*

4.5 Discussion

Attosecond XUV FWM experiments on autoionizing Rydberg states of the polyatomic molecule, CO_2, successfully generate wave-mixing emission signals that decay on ultrafast timescales. Although quantum beat oscillations indicative of the interference of multiple wave-mixing pathways are present in the emission features, traces taken on-resonance of members of the Henning sharp series can be readily fit with single exponential decays, leading to measured decays on timescales of ten of femtoseconds. As described for similar background-free FWM measurements on autoionizing states of krypton and oxygen, the observed decays are equivalent to the excited state lifetimes in the absence of dephasing from interactions with other degrees of freedom. Table 4.1 compares these experimentally measured lifetimes with calculated lifetimes of members of the Henning diffuse and Henning sharp series. The calculated lifetimes for the $n = 6 – 8$ states of the Henning diffuse series range from 30 – 90 fs while those for the $n = 5 – 7$ states of the Henning sharp series decay on timescales over an order of magnitude longer in duration. Given the results of the lifetime calculations (Table 4.1), the experimentally measured wave-mixing decays of 33 $\pm$ 6 fs, 53 $\pm$ 2 fs, and 94 $\pm$ 2 fs are consistent with the lifetimes of the Henning diffuse states, despite emission occurring at the energies of the Henning sharp series.

To rationalize the fact that lifetimes of the diffuse states appear in the emission of the sharp states, the FWM pathways participating in this experiment can be considered with diagrammatic perturbation theory, a method used to depict the evolution of a quantum system in response to multiple pulse interactions. A nonlinear process, FWM emission arises from the third-order polarization of the medium and is therefore described by three, perturbative light-matter interactions. As shown in Figure 4.7, a resonant FWM pathway can be initiated by an XUV photon that excites CO_2 from its ground state to either a Henning diffuse or Henning sharp state. Two NIR photons then couple the XUV-excited Rydberg state to itself or other states within the NIR bandwidth via a resonant dark state, generating a third order polarization response that results in the emission of a photon with the energy of the final state. As a result, four different types of pathways depending on the initial excitation and final emission states can be enumerated: diffuse-to-sharp pathways (Figure 4.7 (a)), diffuse-to-diffuse pathways (Figure 4.7 (b)), sharp-to-sharp pathways (Figure 4.7 (c)), and sharp-to-diffuse pathways (Figure 4.7 (d)). For transient measurements in which the two NIR pulses are delayed with respect to the XUV pulse, the dynamics measured will encode the lifetime of the state initially excited by the XUV photon, rather than the state from which the photon emits.

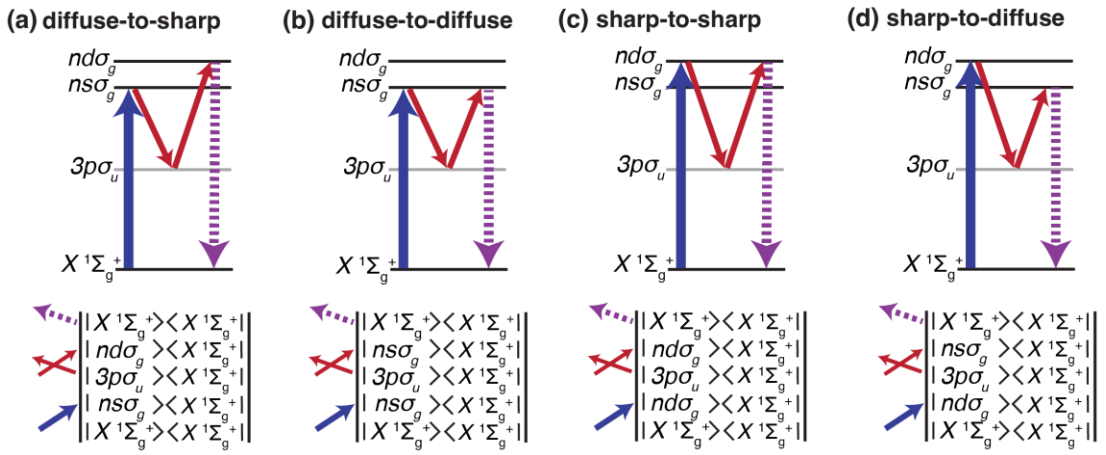

Figure 4.7 (a) Energy level and double-sided Feynman diagrams corresponding to FWM pathways composed of an XUV photon (thick, blue arrows), two NIR photons (thin, red arrows), and wave-mixing emission (dashed, purple arrows) that couple (a) Henning diffuse to sharp states, (b) Henning diffuse to diffuse states, (c) Henning sharp to sharp states, and (d) Henning sharp to diffuse states. In all the depicted pathways, the two NIR pulses are time coincident and are delayed relative to the initial XUV pulse.

Within the framework of perturbation theory, which may not be strictly applicable in attosecond wave-mixing experiments, the intensity of resonant FWM emission signals can be approximated by the oscillator strengths of each stepwise transition between states in the wave-mixing process, as well as the intensity of the XUV and NIR light utilized in each interaction. The FWM emission signal intensity has been shown to vary linearly with NIR intensity in previous work where only a single order of wave-mixing features was observed, validating the application of perturbation theory to these systems. Assuming that the intensity of the broadband light sources is relatively constant within the energy region of interest, the oscillator strengths of different transitions can be utilized to develop an expectation for the dominant FWM pathway. As shown in Table 4.2, the oscillator strengths calculated for the initial XUV excitation are about 2.5 – 10 times larger for the Henning diffuse states than for the sharp states, indicating that the XUV-induced coherent superposition being probed is dominated primarily by the short-lived diffuse states. In contrast, oscillator strengths calculated for NIR transitions between the bright states and the $^1\Sigma_g^+[3p\sigma_u\tilde{B}\ ^2\Sigma_u^+]$ dark state located at ~15.8 eV are about 5 – 20 times stronger for the Henning sharp series, favoring pathways that ultimately emit from these sharp states. As a result, the diffuse-to-sharp pathway depicted in Figure 4.7 (a) should represent the largest contribution to FWM emission, resulting in decays characteristic of the initial Henning diffuse state and emission from the final Henning sharp state. Although nonresonant interactions, higher-order processes, and strong field effects may also influence the intensity and temporal evolution of the emitted signals, we do not observe clear evidence of higher order processes in contrast to other FWM studies. Moreover, the pathways predicted to dominate by this perturbative approach are consistent with the experimental observations of lifetimes with timescales less than 100 fs emitting at the energies of the Henning sharp series.

As discussed above, measurement of the ultrafast lifetimes of the Henning diffuse states is a direct consequence of the resonance-enhanced nonlinear technique used to probe

these Rydberg state dynamics of CO_2. The transitions that comprise each interaction of the FWM scheme work in concert to regulate the emission intensity of individual pathways, selectively enhancing some emission signals relative to others. Favorable pathways are selected not only by the photoabsorption cross section of the state accessed by the XUV pulse, but also by additional NIR transitions between bright and dark states. Thus, attosecond XUV FWM spectroscopy permits the investigation of states that give rise to less prominent features or are obscured by spectral congestion in the linear absorption spectrum. For example, despite less-than-ideal spectral resolution, the oscillator strengths of the FWM interactions in CO_2 operate such that the short-lived, and therefore spectrally broad, Henning diffuse states emit primarily from spectrally narrow Henning sharp states without significant contamination from a long-lived emission component. Although incidental in this system, the results illustrate that, with careful consideration of intermediary dark states and transition oscillator strengths, attosecond XUV FWM spectroscopy coupled with theory can be successfully utilized to emphasize the dynamic signatures from otherwise poorly accessible states.

4.6 Conclusions

In this work, experiment and theory have combined to elucidate the complex nonlinear spectroscopy of short-lived, autoionizing Rydberg states located between 17.3 – 18.1 eV in the polyatomic greenhouse gas, CO_2. Experimentally, attosecond XUV FWM spectroscopy, a recently developed nonlinear technique that utilizes a noncollinear beam geometry between a short train of subfemtosecond XUV pulses and two few-cycle NIR pulses, generates background-free FWM signals in a complex spectral region dominated by the $ns\sigma_g$ character Henning diffuse and the $nd\sigma_g$ character Henning sharp Rydberg series. Transient FWM signals predominantly emit from the n = 5 – 7 members of the spectrally narrow Henning sharp series from 17.3 – 18.1 eV. Theoretical calculations indicate that the experimentally measured decays of 33 ± 6 fs, 53 ± 2 fs, and 94 ± 2 fs correspond to the lifetimes of the n = 6 – 8 states of the Henning diffuse series, respectively. Following identification of the $^1\Sigma_g^+[3p\sigma_u\tilde{B}\ ^2\Sigma_u^+]$ dark state as the best candidate to mediate the wave-mixing process, the oscillator strengths of transitions between all states potentially involved in resonant FWM pathways were calculated to rationalize the dominance of the Henning diffuse states in transient wave-mixing measurements. Large ground-to-diffuse state oscillator strengths combined with substantial oscillator strength transitions between the dark state and the Henning sharp states result in the selection of pathways characterized by an initial XUV excitation to Henning diffuse states, but emission from the Henning sharp states. Consistent with the reported experimental lifetimes, these pathways generate FWM signals that encode the lifetimes of the Henning diffuse states in the FWM emissions of the sharp states. This work broadly demonstrates that, with the correct set of coupling strengths, the properties of short-lived, spectrally broad features can be successfully measured using emission from more spectrally narrow resonances, reducing the impact of spectral congestion. Therefore, these results not only provide insights into the decay dynamics of autoionization states in a highly significant polyatomic molecule, but also illustrate a powerful application of experimental and theoretical attosecond XUV FWM analysis that can be utilized in more complex chemical systems.

4.7 Appendices

4.7.1 Appendix A: Experimental Parameters

A total of three datasets were collected up to five months apart to verify experimental findings. Table 4.3 summarizes the parameters utilized for each of the three datasets. For all experiments, one averaged CCD camera image of the signal with all three laser beams present ($I_{NIR\ ON}$) and one averaged image with the two NIR pulses absent ($I_{NIR\ OFF}$) were recorded for each delay. Both images are constructed from the same number of laser pulses per delay, which can be calculated using the following equation:

$$pulses\ per\ delay = exposure\ time\ (s) \times repetition\ rate\ (Hz) \times \#\ of\ images \tag{4.3}$$

where the repetition rate is 1000 Hz. The exposure time refers to the length of time the CCD camera collects photons to generate a single image, which is then averaged with other images taken at the same delay to generate the averaged image used for analysis. Values for the exposure time and the number of images can be found in Table 4.3. Several hours of stable signal are required to complete each dataset. Note that backing pressure refers to the pressure of CO_2 gas measured in the delivery lines before entering the vacuum chamber. All figures shown in the Chapter originate from dataset #3.

Dataset	Delay Range (fs)	Delay Step Size (fs)	Exposure Time (s)	# of Images	Pulses per Delay	Backing Pressure (Torr)
#1: 2/27/20	-15 – 255	1 fs: -15 – 67 fs 2 fs: 68 – 255 fs	1.5	10	15000	4
#2: 7/29/20	-14 – 146	1 fs	1.2	10	12000	9
#3: 7/30/20	-25 – 315	2 fs	1.2	15	18000	11

Table 4.3 The data collection parameters employed for the three experimental datasets examined in this work.

4.7.2 Appendix B: Fitting Results of Additional Dataset

Wave-mixing emission features at the energies of the Henning sharp $n = 5 – 7$ states observed in datasets #1 and #2 are fit to a convolution of the instrumental response and an exponential decay using a least squares algorithm in Figure 4.8. Similar fits for dataset #3 are provided in Figure 4.6 of this Chapter. The results of performing this fitting procedure on all datasets are summarized in Table 4.4. The reported decays represent the mean and standard deviation of the fits of the three datasets.

	#1: 2/27/20	**#2: 7/29/20**	**#3: 7/30/20**	**Average**
$n = 5$	35 ± 1 fs	26 ± 1 fs	38 ± 2 fs	33 ± 6 fs
$n = 6$	52 ± 1 fs	51 ± 2 fs	55 ± 1 fs	53 ± 2 fs
$n = 7$	96 ± 1 fs	94 ± 4 fs	93 ± 3 fs	94 ± 2 fs

Table 4.4 The experimentally measured wave-mixing decays are fit to a convolution of the instrumental response and an exponential decay.

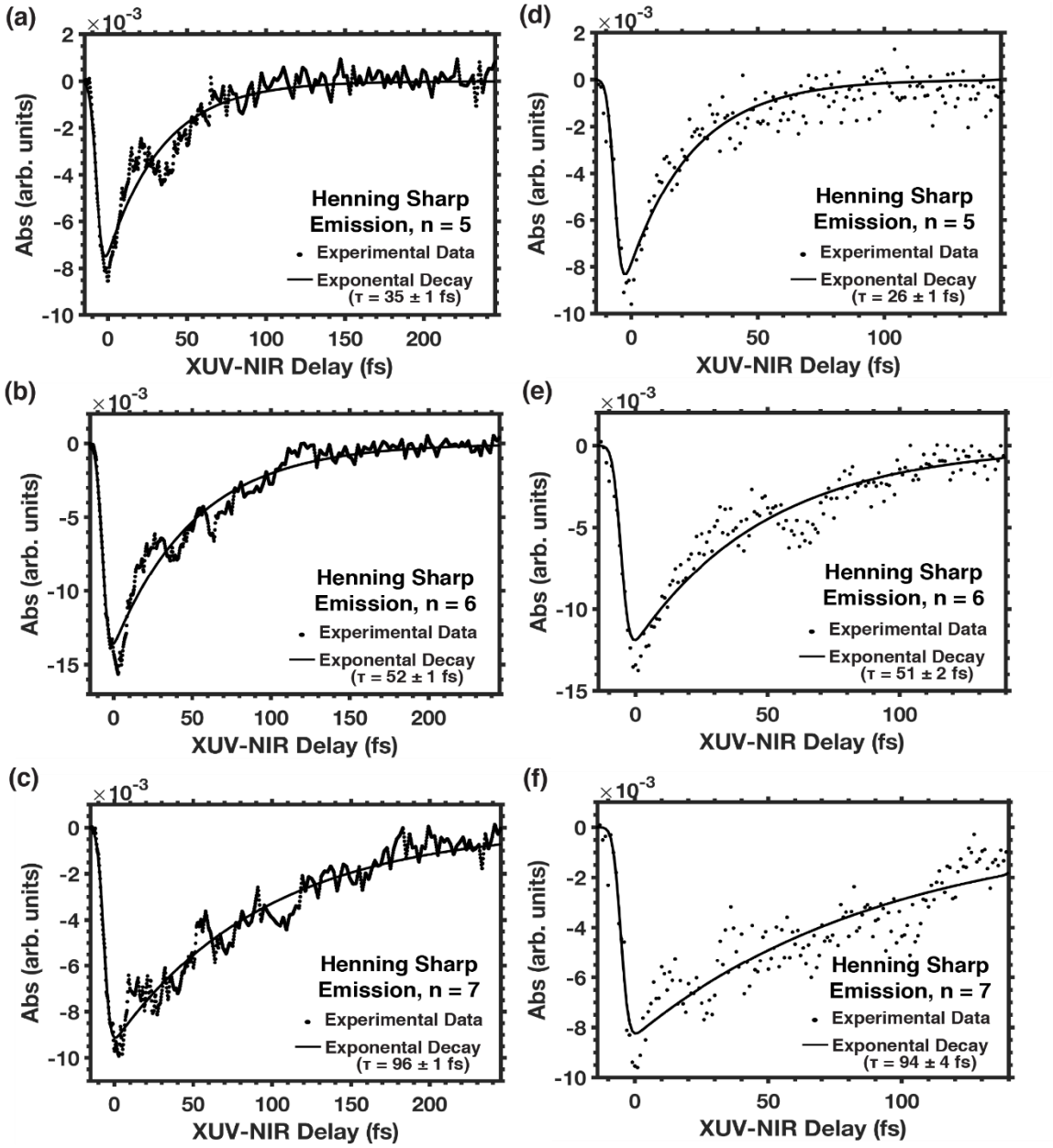

Figure 4.8 Delay-dependent traces of wave-mixing emission features observed at the energy positions of the Henning sharp (a) n = 5 (17.49 – 17.55 eV), (b) n = 6 (17.66 – 17.70 eV), and (c) n = 7 (17.77 – 17.80 eV) states in dataset #1 and the (d) n = 5 (17.48 – 17.54 eV), (e) n = 6 (17.65 – 17.71 eV), and (f) n = 7 (17.76 – 17.81 eV) states in dataset #2. The dots in each of the panels represent measured experimental data while the solid lines are numerical fits. The time constants and errors provided here correspond to the least squares fit of a single data set. The data points of dataset #1 were interpolated to obtain a constant step size for analysis. The decay constants measured correspond with the lifetimes of the Henning diffuse states, not the sharp states from which they emit.

Chapter 5: Nonresonant Coherent Amplitude Transfer in Attosecond Four-Wave-Mixing Spectroscopy

The content and figures of this chapter are reprinted or adapted with permission from J. D. Gaynor, A. P. Fidler, Y. Kobayashi, Y.-C. Lin, C. L. Keenan, D.M. Neumark, S.R. Leone, Phy. Rev. A. ***107****, 023526 (2023).*

5.1 Abstract

Attosecond four-wave mixing spectroscopy using an XUV pulse and two noncollinear near-infrared pulses is employed to measure Rydberg wave packet dynamics resulting from extreme ultraviolet excitation of a 3s electron in atomic argon into a series of autoionizing $3s^{-1}np$ Rydberg states around 29 eV. The emitted signals from individual Rydberg states exhibit oscillatory structure and persist well beyond the expected lifetimes of the emitting Rydberg states. These results reflect substantial contributions of longer-lived Rydberg states to the four-wave mixing emission signals of each individually detected state. A wave packet decomposition analysis reveals that coherent amplitude transfer occurs predominantly from photoexcited $3s^{-1}(n+1)p$ states to the observed $3s^{-1}np$ Rydberg states. The experimental observations are reproduced by time-dependent Schrödinger equation simulations using electronic structure and transition moment calculations. The theory highlights that coherent amplitude transfer is driven non-resonantly to the $3s^{-1}np$ states by the near-infrared light through $3s^{-1}(n+1)s$ and $3s^{-1}(n-1)d$ dark states during the four-wave mixing process.

5.2 Introduction

Rydberg wave packets are nonstationary states composed of a coherently phased superposition of stationary Rydberg eigenstates. These states are typically well characterized in noble gases, lending them well to systematic investigation. Rydberg state lifetimes are expected to scale by $(n^*)^3$, where the effective principal quantum number, $n^* = n - \delta$, accounts for the quantum defect, δ; this follows from established rules for the oscillator strengths of autoionizing states in a Rydberg series [144-146]. Thus, Rydberg series in atomic gases can be used to investigate the evolution of Rydberg wave packets following the broadband excitation of a coherent superposition of well-defined stationary eigenstates. Recent interest in using Rydberg atoms in quantum simulators by coherently manipulating core electrons of atoms while they exist in excited Rydberg states underscores the importance of precisely measuring coherent interactions among autoionizing Rydberg states [147]. The ability to prepare and manipulate quantum superposition states coherently, affecting their individual components and time-dependent evolution, has long been sought after to develop new quantum technologies [148]. One key aspect of interpreting quantum coherences is precisely understanding how information about the superposition is encoded in the reporting states from which a signal is detected.

Using broadband attosecond light pulses at extreme ultraviolet (XUV) photon energies produced in tabletop optics laboratories, one can generate a coherent electronic wave packet comprising a superposition of multiple Rydberg states. The evolution of these

coherent dynamics may then be followed with attosecond and few-femtosecond (fs) temporal resolution owing to the ultrashort pulse durations that are now routinely available [149]. Attosecond four-wave mixing (FWM) spectroscopy is a powerful new means of measuring ultrafast dynamics in atomic and molecular systems that are excited by such broadband XUV attosecond pulses [6,8,9,12,150]. This FWM technique utilizes a noncollinear beam geometry to generate background free XUV emission signals from phase-matched wave-mixing pathways in a sample. Recent attosecond FWM studies have shown that accurate lifetimes of highly excited individual states are directly obtainable in the time-domain for a few specific cases. For example, the autoionization lifetimes of the $4p^{-1}6d$, $4p^{-1}7d$, and $4p^{-1}8d$ Rydberg states in gaseous Kr were directly characterized by Fidler *et al.* [11] in agreement with frequency-domain literature values. Lin *et al.* [14]measured the few-fs lifetimes of two vibrational levels in gaseous O_2 in the $3s\sigma_g$ Rydberg series converging to the O_2^+ *c* state around 21 eV, revealing an interplay between electronic autoionization rate and internuclear distance. In a study of NaCl with Na^+ $L_{2,3}$-edge excitation, Gaynor *et al.* [15] identified and characterized the few-fs lifetimes of several atomic-like core-excitons that are highly localized about the Na^+ in the ionic solid. In some cases, the accurate time-domain retrieval of dynamics using attosecond FWM spectroscopy can be known, or assumed, to be through resonant transitions between XUV-excited bright states and nearby dark states driven by few-cycle near-infrared (NIR) pulses. However, the FWM process can involve optical transitions between multiple excited states, which may occur resonantly or non-resonantly, and the origin of the FWM signal from each individual state may not arise from the particular observed state. An accurate understanding of time-dependent coherent dynamics in atomic and molecular systems requires careful consideration of each light-matter interaction involved in the FWM experiment [16,151].

Figure 5.1 illustrates how a broad bandwidth of XUV excited states, such as in a Rydberg wave packet, is monitored in attosecond FWM spectroscopy. The blue shaded region indicates the coherent excitation of many stationary eigenstates by the broadband XUV light pulse represented by the blue arrow, and the two red arrows reflect consequent time-controlled light-matter interactions between the XUV excited states and nearby dark states that are driven by few-cycle NIR pulses. The two depicted pathways show the possibility for two or more different excited states within the wave packet to couple directly to the same XUV bright state from which the signal is emitted. As explored in this paper, this mechanism can lead to the amplitudes and timescales from otherwise unexpected states influencing, or even dominating, the dynamics of the FWM emission signals.

In this Chapter, attosecond FWM spectroscopy is used to study Rydberg wave packet dynamics arising from single 3s electron excitations in gaseous Ar, accessing the $3s^{-1}3p^6$ *np* (^{1}P) series of autoionizing Rydberg states that converge to the $3s^{-1}3p^6$ ($^2S_{1/2}$) level of Ar^+ at 29.24 eV [152,153]. A broadband attosecond XUV pulse initiates a coherent superposition of these $3s^{-1}np$ Rydberg states ($n \geq 4$), creating the Rydberg wave packet. Then, two noncollinear few-cycle NIR pulses probe the evolution of the Rydberg wave packet. The light-matter interactions complete a phase-matched wave-mixing process, producing an XUV-emission from each of the $3s^{-1}np$ Rydberg states that is spectrally and temporally resolved. Thus, the wave packet dynamics are projected onto each $3s^{-1}np$ Rydberg state emission. As illustrated in Figure 5.1, the observed time-dependent FWM emission from each Rydberg state contains information about how the amplitudes of the

multiple states in the initial Rydberg wave packet are transferred through the second and third light-matter interactions driven by the NIR pulses.

A comprehensive analysis of coherent superpositions created by the excitation of an Ar $3s^{-1}np$ Rydberg wave packet around 29 eV is presented. The experimental measurements are fitted to a wave packet model to extract the amplitude coefficients of the coherent superposition responsible for the time-dependent FWM emission from individual $3s^{-1}np$ Rydberg eigenstates. Calculations using the time dependent Schrödinger equation support the measurements and wave packet modeling to elucidate the coherent amplitude transfer that occurs during the few-cycle NIR pulse interactions, resulting in the set of coherent oscillations observed in the detected individual state emissions. The results indicate that the coherent decay signals from $3s^{-1}np$ states are dominated by their coupling to longer-lived $3s^{-1}(n+1)$p states created by the XUV excitation pulse, and that this coupling occurs via non-resonant amplitude transfer through the optically dark $3s^{-1}(n+1)$s and $3s^{-1}(n-1)$d states driven by the NIR pulses. Moreover, each emitting $3s^{-1}np$ state displays strong quantum beating, primarily between itself and the $3s^{-1}(n+1)$p state, with minor components from other states. Overall, the Rydberg series measurements reported here act as a vehicle for discussing the role of non-resonant coherent amplitude transfer in attosecond FWM spectroscopy.

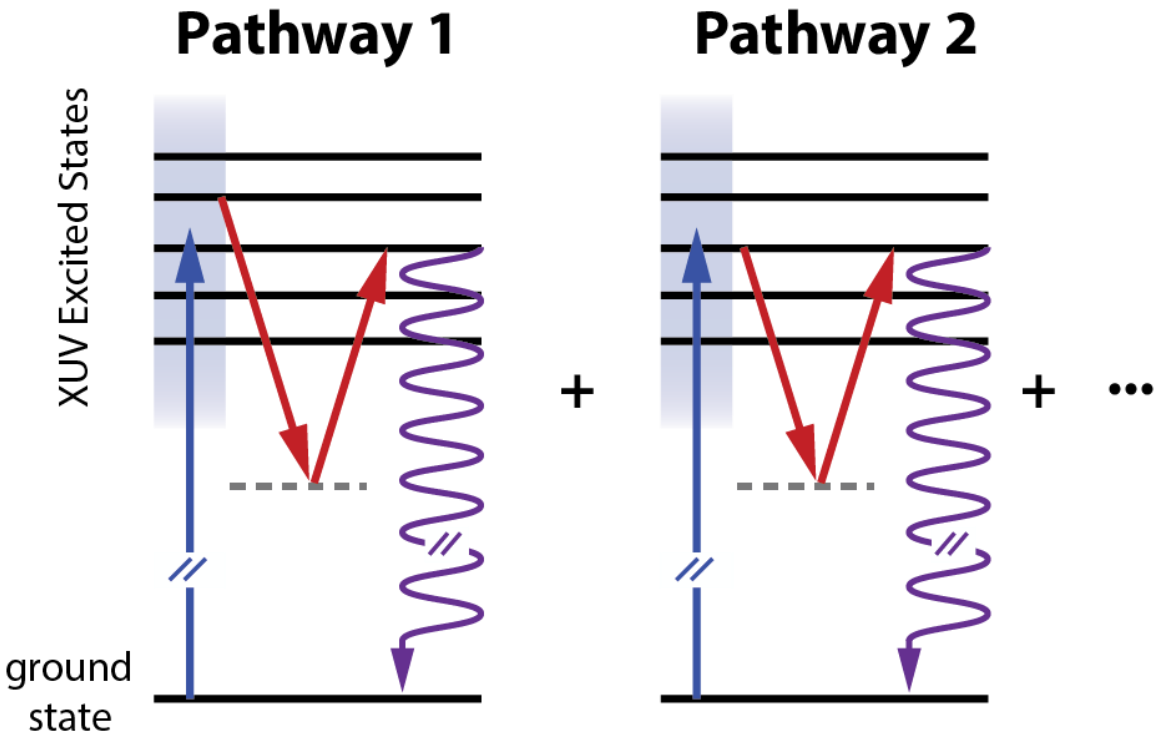

Figure 5.1 Multiple pathway interference schematic for tracking quantum coherences. A broadband attosecond extreme ultraviolet (XUV) pulse excites a large superposition of states, creating a wave packet. The wave packet can then evolve, and be affected by, consequent light-matter interactions. The detected emission from a single state may contain information from multiple pathways that end in the same final emitting state. The amplitudes and timescales of the measured dynamics can be influenced by each light-matter coupling.

5.3 Results and Analysis

5.3.1 Attosecond FWM Spectra of Ar Rydberg Wave packets

The apparatus and technique have been described previously [11,15]. Briefly, the output of a Ti:sapphire laser (Femtopower, 1 kHz repetition rate, 1.7 mJ/pulse, 22 fs, 780 nm) is spectrally broadened in a stretched hollow core fiber compressor (Few-Cycle Inc.) and temporally compressed using a combination of seven chirped mirror pairs (Ultrafast Innovations, PC70), fused silica wedge pairs, and a 2 mm thick ammonium dihydrogen phosphate (ADP) crystal. This yields pulses of sub-6 fs pulse durations with spectra spanning 550-950 nm and ~600 μJ/pulse energies. The beam is then split by a 75:25 (R:T) beam splitter in a Mach-Zender interferometer to separate the NIR driving pulse used to create the XUV pulse by high harmonic generation (HHG) from the pulse used to generate the two noncollinear NIR beams.

Attosecond pulses of XUV radiation in the 25-45 eV range are produced by HHG in Kr (~4 Torr backing pressure). A 150 nm thick Al foil attenuates the co-propagating NIR driving field from the newly generated XUV pulse. The transmitted XUV pulse is refocused by a gold-coated toroidal mirror through an annular mirror into a 1 mm pathlength gas cell for the sample, in which Ar flows out of the laser entrance and exit pinholes at a backing pressure of 14 Torr. The remaining NIR pulse in the other arm of the Mach-Zender interferometer is delayed relative to the XUV beam using a piezoelectric translation stage, and this beam is then further split with a 50:50 beam splitter to create the two NIR pulses for use in the wave-mixing experiment. The relative temporal delay between the two NIR pulses is further controlled using a second piezoelectric translation stage. The two NIR beams are focused and routed through the vacuum chamber to the sample cell to overlap with the XUV pulse spatially and temporally. The two NIR beams are vertically arranged, one above and one below the XUV beam. The interaction of all three beams with the sample produces the phase-matched background free FWM signal.

The NIR pulse envelope is estimated to be 5.6 fs from the rise time of the Ar $3s^{-1}4p$ autoionization signal measured by attosecond transient absorption (ATA). The emitted XUV signals are filtered using another 150 nm Al foil, then spectrally dispersed in the horizontal plane with a flat field grating and recorded using an X-ray CCD camera. In addition to the background free wave-mixing signals, there are ATA signals that co-propagate with the XUV beam. The wave-mixing signals can be isolated from the ATA signal and residual XUV beam, and then further optimized, using a vertically translatable camera mount that allows for the unwanted ATA signals and XUV beam to be translated off the CCD imaging area.

The transient FWM spectrum of the Ar $3s^{-1}np$ Rydberg wave packet is shown in Figure 5.2 (a) with temporal lineouts shown as solid lines in Figure 5.2 (b). Time-dependent emissions from the $3s^{-1}5p$-9p Rydberg states appear as horizontal features in Fig. 5.2 (a). Signatures from the coherent superposition of Rydberg states are prominent in the FWM signals, manifested as strong intensity oscillations in the emissions from each $3s^{-1}np$ Rydberg state. Clear variations exist in the coherent oscillation periodicity and modulation depth for $3s^{-1}np$ emissions of different principal quantum number. In general, the oscillations have a larger modulation depth and a lower frequency as n increases. The decay times of the $3s^{-1}np$ emissions increase with n, in agreement with the well-known trend in autoionization lifetimes. However, the measured decay time of each $3s^{-1}np$ emission is

substantially longer than expected from frequency-domain linewidth measurements [152,154,155] and calculations [156] found in the literature for that state. For example, the $3s^{-1}5p$ and $3s^{-1}6p$ state linewidths obtained from synchrotron photoabsorption experiments are 28.2 meV and 12.6 meV, respectively, corresponding to lifetimes of 23.3 fs and 52.2 fs [152,154]. For comparison, single exponential decay functions with the decay rate corresponding to the frequency-domain line widths for the $3s^{-1}5p$ and $3s^{-1}6p$ Rydberg states are shown in Figure 5.2 (b) as dashed blue and dashed red lineouts, respectively. The experimental temporal lineouts of the $3s^{-1}5p$ (blue) and $3s^{-1}6p$ (red) states in Figure 5.2 (b) decay on ~50 fs and ~150 fs timescales, respectively.

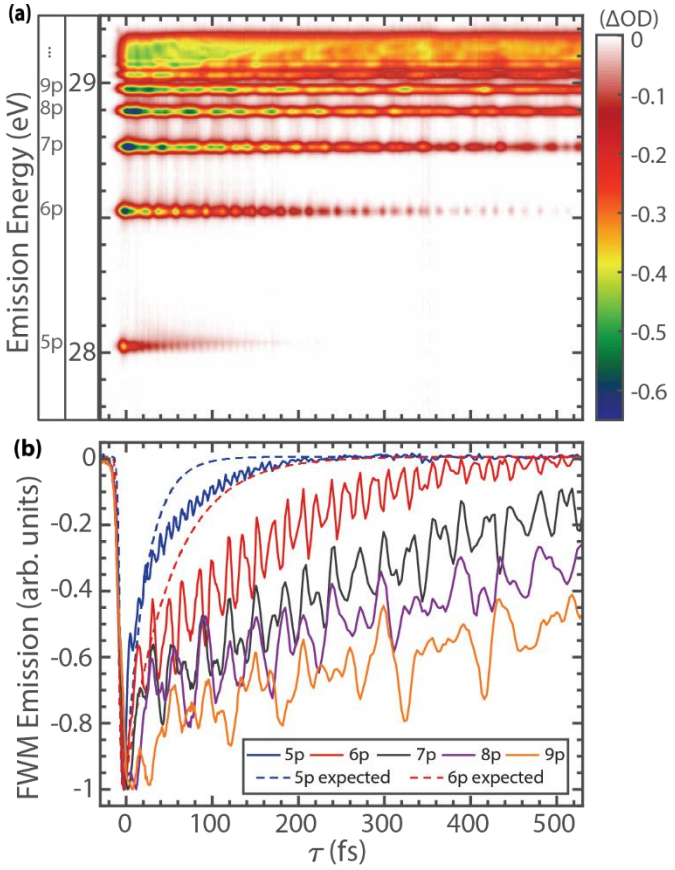

Figure 5.2 Strong coherent oscillations in transient four-wave mixing spectra of Ar $3s^{-1}np$ Rydberg series. The transient four-wave mixing spectra of the autoionizing Ar $3s^{-1}np$ Rydberg series (a). Temporal traces taken at the peaks of various Rydberg state emissions to see the temporal oscillations more clearly (b). The solid lineouts in (b) correspond to experimentally measured traces while the dashed blue and dashed red traces are simulated single exponential decay functions with the decay rates specified from frequency-domain linewidth measurements of 23.3 fs for the 5p and 52.2 fs for the 6p, respectively.

The discrepancy between the frequency-domain linewidths and the time-domain FWM decays in Figure 5.2 (b) along with the pronounced quantum beating, conveys that the observed Ar $3s^{-1}np$ Rydberg series FWM emissions exhibit more complex dynamics than a one-to-one mapping of the initial Rydberg wave packet excited by the attosecond XUV pulse. Previous work [11] has shown this one-to-one mapping can occur when the NIR interactions are resonant with XUV-dark states during V- or Λ-type FWM pathways. To

better understand the detected FWM emission from the Ar $3s^{-1}np$ Rydberg wave packet, the features in Figure 5.2 were decomposed into the constituent eigenstates in the superposition by determining their relative amplitudes and phase.

Analysis of the $3s^{-1}5p$ emission is presented in Figure 5.3 (a-d) and the $3s^{-1}6p$ emission is shown in Figure 5.3 (e-h). The decay of the *n*th Rydberg eigenstate is represented as $\psi_n(\omega_n, \Gamma_n, t) = -ie^{i\omega_n t + \frac{\Gamma_n}{2}t}$ while $\Psi(t) = \sum_n A_n \times \psi_n(\omega_n, \Gamma_n, t)$ is the coherent superposition of all Rydberg eigenstates. Here, ω is the Rydberg state energy, Γ is the autoionizing linewidth, and $A_n = a_n e^{i\phi_n}$ are the complex superposition coefficients with amplitudes a_n and phase ϕ_n. The emitted FWM signal reports on the dynamics of the Rydberg wave packet, and the intensity of the emitted electric field during the FWM process is detected experimentally. The experimental data are fit to $|\Psi(t)|^2$ using this model; to fit the FWM emission traces, the Rydberg state energies were initially set to literature values and allowed to float by ± 10 meV to match more closely the 11 meV experimental resolution of our spectrometer. The fits in Figure 5.3 were obtained by including the $4 \leq n \leq 10$ members of the $3s^{-1}np$ series. See Section 5.6 for further information on the fitting procedure.

The emitted FWM signal reflects the dynamics of the coherent superposition resulting from the initial XUV-prepared Ar $3s^{-1}np$ Rydberg wave packet being re-shaped from two NIR light-matter interactions. It is important to note the difference between the initial Rydberg wave packet prepared by the XUV pulse and the coherent superposition that generates the FWM emission signal. The detected coherence signal results from probing the initial XUV-prepared Rydberg wave packet with the two NIR light-matter interactions that project part of the initial Rydberg wave packet onto each final Rydberg state, which then emits a FWM signal.

As shown in Figure 5.3 (a) and 5.3 (e), very good agreement between the model and the experimental data is achieved for the $3s^{-1}5p$ and $3s^{-1}6p$ emissions, giving R^2 goodness of fit parameters of 0.99 and 0.96, respectively. The emitted coherence dynamics observed in the $3s^{-1}5p$ and $3s^{-1}6p$ emissions are then elucidated by plotting the a_n coefficients for all eigenstates in Figure 5.3 (b) and 5.3 (f). Interestingly, emission from the $3s^{-1}5p$ state is dominated by the character of the $3s^{-1}6p$ state; similarly, the $3s^{-1}6p$ emission is dominated by the $3s^{-1}7p$ state. This trend also holds for the $3s^{-1}7p$ emission, although the fit is worse for higher *n* Rydberg states, as neighboring states are energetically closer; see Section 5.6 for 7p fitting.

The FWM intensity oscillations characterizing the coherent superposition are directly analyzed by subtracting the multi-exponential decay that arises from the fits as the diagonal $|A_n\psi_n|^2$ terms. The experimental coherence signatures of the $3s^{-1}5p$ and $3s^{-1}6p$ emissions are isolated in Figure 5.3 (c) and 5.3 (g), along with their Fourier transforms in 5.3 (d) and 5.3 (h), respectively. These signatures reflect the cross terms of the type $(A_n\psi_n)(A_m\psi_m)$ where $n \neq m$. The most intense oscillations of the *np* emission – e.g., peak i at 0.49 eV and peak ii at 0.24 eV in Figures 5.3 (d) and 5.3 (h), respectively – occur at the beat frequency corresponding to the energy difference between the *(n+1)p* and the *np* Rydberg states. These respective energy differences are consistent with the 0.50 eV separation of the $3s^{-1}5p$ and $3s^{-1}6p$ states and with the 0.24 eV separation of the $3s^{-1}6p$ and $3s^{-1}7p$ states as measured in our spectrometer. We note that the 5.6 fs duration of the instrument response may limit the experimental resolution of the coherent modulation depth for superposition states with energetic separation greater than 0.7 eV (5.9 fs). However, this does not alter

the analysis, which is primarily determined by the lifetimes of the decaying Rydberg states, rather than the depth of modulation.

It is clear from the analysis in Figure 5.3 that the NIR wave-mixing pulses drive pathways that transfer amplitude from the $(n+1)p$ states of the Rydberg wavepacket to the np states that produce FWM emission. There are additional superposition components of smaller magnitude in Figures 5.3 (d) and 5.3 (h). Peak iii appears at 0.38 eV in good agreement with the experimentally measured 0.37 eV energy difference between the $3s^{-1}6p$ and $3s^{-1}8p$ Rydberg states. Although weak, peak iv appears at 0.47 eV and is assigned to interfering contributions between the $3s^{-1}5p$ and $3s^{-1}6p$ coherence and the $3s^{-1}6p$ and $3s^{-1}9p$ coherence, both of which are expected at 0.45 eV. As discussed below in Figure 5.4, consideration of oscillator strengths between XUV-bright and XUV-dark states that are all far off-resonant with the NIR pulses provide a rationale for why certain states contribute more than others in this specific case.

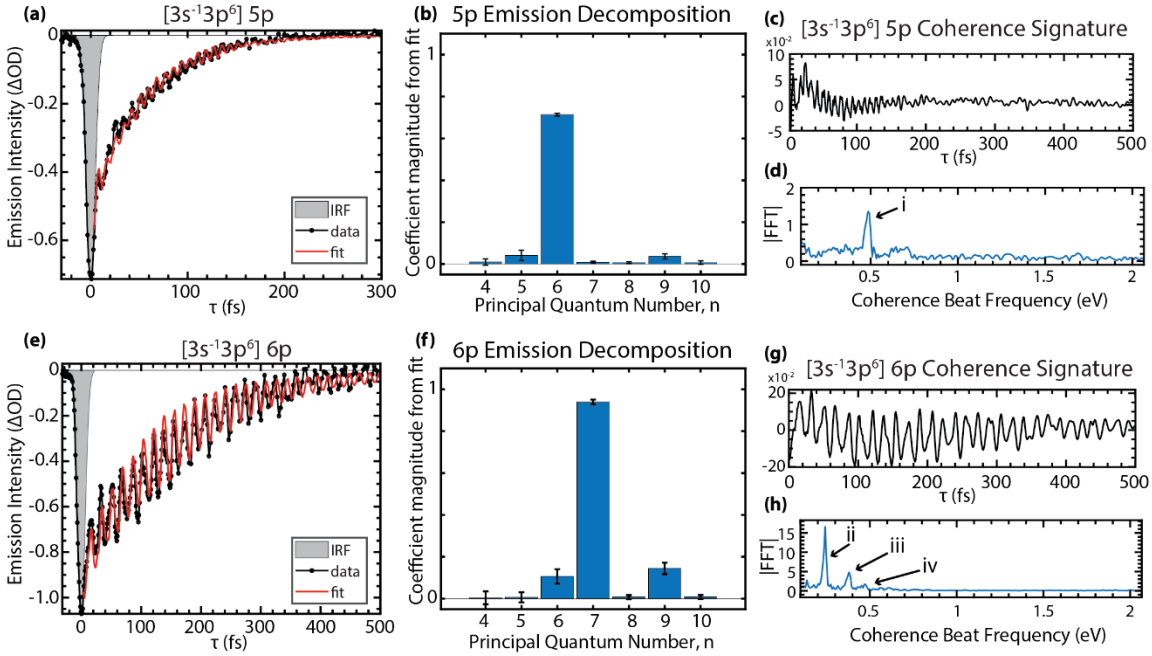

Figure 5.3 Extracting the $3s^{-1}np$ state amplitudes composing the Rydberg wavepacket through four-wave mixing emission. The wave-mixing signal of the $3s^{-1}5p$ signal is analyzed in (a-d) and the $3s^{-1}6p$ signal is analyzed in (e-h). The signals are first fit to the wavepacket model described in the text (a,e). The coefficient amplitudes a_n of each component Rydberg state in the wavepacket is plotted as obtained from the fit (b,f) with the error bars representing the 95% confidence interval of the amplitudes. The exponential decay components from the fit are subtracted to isolate the coherent oscillations in the wave-mixing signals (c,g) and then the oscillations are Fourier transformed to identify the primary coherence components in the signals (d,h). Peaks labeled i-iv are discussed further in the text.

5.3.2 Calculated Oscillator Strengths: A Quantum Roadmap

In this section, the experimentally observed coherence dynamics are explored theoretically to understand the physical origins of the coherence signatures discussed above with the goal of understanding more clearly how the NIR pulses complete the FWM

pathways to produce the emitted signals. To achieve this, the oscillator strengths between the bright and dark states are calculated (Figure 5.4) and the time-dependent emissions of an Ar $3s^{-1}np$ Rydberg wave packet are simulated and analyzed (Figure 5.5). The energies of the Ar ground state, $3s^{-1}np$ ($4 \leq n \leq 9$) states, $3s^{-1}ns$ ($4 \leq n \leq 9$) states, and $3s^{-1}nd$ ($3 \leq n \leq 9$) states are calculated using the Cowan atomic structure code [157]. See Section 5.7 for further details on electronic structure calculations. The oscillator strengths between the XUV-allowed $3s^{-1}np$ states and the XUV-forbidden $3s^{-1}ns$ and $3s^{-1}nd$ states are shown in Figure 5.4 (a) through the relative size of the colored circles. For example, the pink circle in the bottom left reflects the oscillator strength for the transition between the $3s^{-1}5p$ and $3s^{-1}5s$ states and is calculated as 0.494. Similarly, the calculated oscillator strength for the $3s^{-1}5p$ to $3s^{-1}6s$ transition is 0.301. Table 5.1 lists the oscillator strengths for the principal transitions shown in Figure 5.4 (a). The oscillator strengths for the other transitions not listed in the table are typically orders of magnitude smaller; see Section 5.7 for complete list of calculated oscillator strengths.

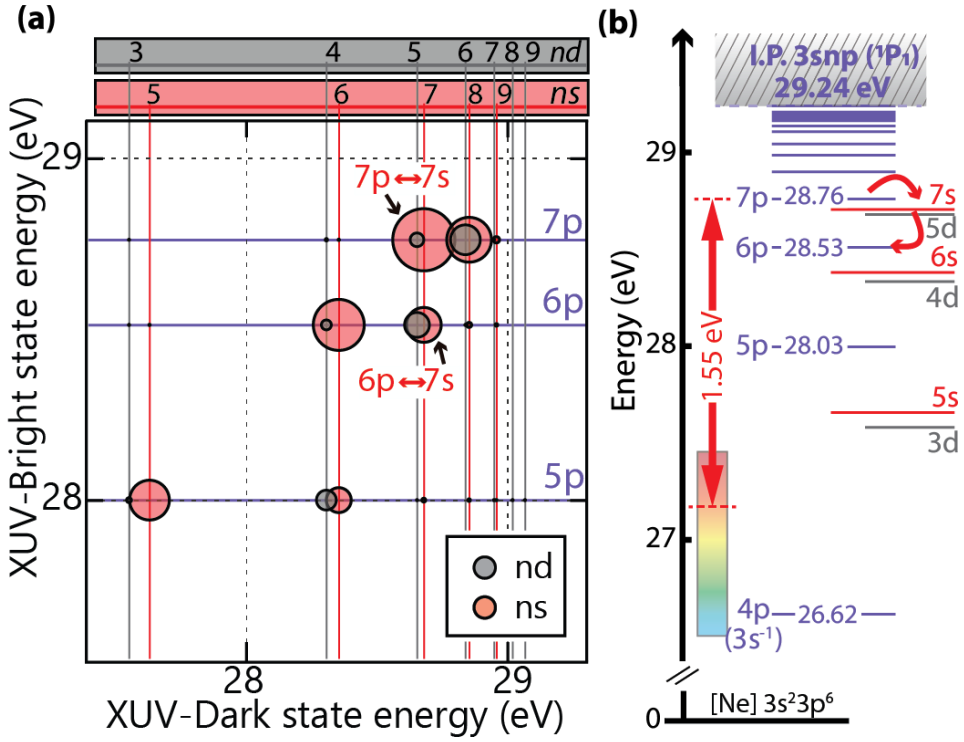

Figure 5.4 Calculated oscillator strengths and energy level diagram for XUV-bright and XUV-dark states. The energies of the $3s^{-1}np$, $3s^{-1}ns$, and $3s^{-1}nd$ Rydberg state with respect to the [Ne] $3s^2 3p^6$ ground state of Ar are shown in (a). The XUV-allowed $3s^{-1}np$ states are plotted on the vertical axis with purple grid lines and the XUV-forbidden $3s^{-1}ns$ and $3s^{-1}nd$ states are plotted on the horizontal axis with pink and grey lines, respectively. The oscillator strengths for the $3s^{-1}np \leftrightarrow 3s^{-1}ns$ / $3s^{-1}nd$ transitions are represented by the size of the circles; the position of the circle in the two-dimensional plot specifies the transition. An energy level diagram of relevant states in Figure 5.3 is shown in (b). The center energy and bandwidth of the NIR pulses is shown with respect to the $3s^{-1}7p$ state to highlight the non-resonant condition probed in the experiment (NIR bandwidth is represented by the rainbow-colored box). See text for discussion of the example pathway highlighted in this figure.

***n*p**	**(*n*)s**	**(*n+1*)s**	**(*n-2*)d**	**(*n-1*)d**
5p	0.494	0.301	0.049	0.238
6p	0.637	0.429	0.103	0.305
7p	0.776	0.557	0.158	0.368

Table 5.1 Calculated oscillator strengths for NIR-driven principal transitions (arb. units)

Collectively, Figure 5.4 (a) and Table 5.1 show that the largest oscillator strengths are for transitions where first the angular orbital momentum quantum number reduces by one (e.g., 7p to 7s in the first column), followed by strong oscillator strengths for transitions where the principal quantum number also changes (e.g, 6p to 7s in the second column). A representative pathway connecting $3s^{-1}7p$ character with the $3s^{-1}6p$ state is pointed out with arrows and labels in Figure 4(a) and with red curved arrows in Figure 5.4 (b). This pathway demonstrates that the $3s^{-1}7p$ excitation can connect to the $3s^{-1}7s$ dark state with the first NIR interaction, followed by the transition to the $3s^{-1}6p$ bright state with the second NIR interaction. In this way, Figure 5.4 (a) serves as a map of the quantum transition pathways that result in the observed coherence signatures and the extended decay times of the Ar $3s^{-1}np$ Rydberg states in Figure 5.2. Specifically, the results suggest that the $(n+1)s$ and $(n-1)d$ states are the dominant XUV-forbidden states connecting the np and $(n+1)p$ states during the FWM process. When the Rydberg wavepacket dynamics are projected back onto the $3s^{-1}np$ states by the $XUV \pm NIR_1 \pm NIR_2$ pulse sequence, the enhanced $(n+1)p$ character extends the coherent wavepacket dynamics observed in the FWM signal decay time beyond what is expected from the individual $3s^{-1}np$ Rydberg states. These calculations are consistent with the experimental observations shown in Figure 5.3. Interestingly, as the energy level diagram in Figure 5.4 (b) shows, the observed FWM transition pathways are highly non-resonant for the NIR pulses. The energy separations between identified states involved in the wave-mixing pathways span 0.05 eV-0.35 eV, whereas the NIR pulse spectrum spans 1.23 eV – 2.25 eV.

To confirm the origin of the time-dependent behavior measured in the FWM experiment, the transient response of the argon atoms is simulated by numerically solving the time-dependent Schrödinger equation (TDSE) where the transition dipole moments between the calculated $3s^{-1}np$, $3s^{-1}ns$, and $3s^{-1}nd$ states are explicitly included. The results are shown in Figure 5.5; see Supplementary Material for TDSE simulation details. The TSDE simulation in Figure 5.5 (a) shows prominent coherences and the beat frequencies are identified by Fourier transform analysis in Figure 5.5 (b). The Fourier components from the TDSE simulation highlight the influence of the oscillator strengths calculated in Figure 5.4 (a) through the dynamics. For comparison with theory, the experimental FWM spectrum in Figure 5.2 (a) has also been Fourier transformed over the XUV-NIR time delay (τ_1), which is given in Figure 5.5 (c). We note that the experimental coherence peaks lie on top of strong features at very low frequencies that approach 0 eV due to the underlying exponential decay dynamics. The noise level in Figure 5.5 (c) is greater than the FFT analyses in Figures 5.3 (d) and 5.3 (h) because the underlying multiexponential decay components are not able to be removed globally to enable the enhanced resolution FFT analysis shown in Figure 5.3.

The black outlined boxes in Figure 5.5 (b) group the beat frequencies of the coherences involving the np and $(n+1)p$ states. The grey box shows the additional $6p \leftrightarrow 8p$ coherence viewed in the 6p emission. Peaks i-iv, as observed in the experimental analysis

of Figures 5.3 (d) and 5.3 (h), are labeled in green in the theoretical coherence map of Figure 5.5 (b), providing theoretical confirmation of the identified coherences and explanation. Peak i is present in the theoretical 5p emission at 0.50 eV coherence frequency and 27.99 eV XUV emission energy. Peak ii is observed in the theoretical 6p emission at 0.24 eV coherence frequency and 28.51 eV XUV emission energy. Peak iii appears at 0.38 eV coherence frequency and 28.51 eV. The two expected contributions to peak iv are present in the theoretical 6p emission; the 5p↔6p coherence is observed at 0.50 eV and the 6p↔9p coherence feature appears at 0.46 eV.

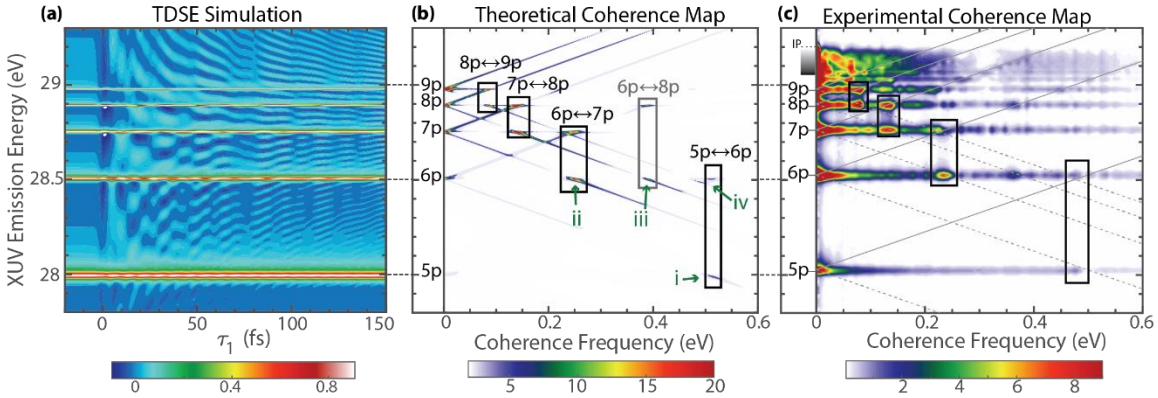

Figure 5.5 Theoretical and experimental coherence maps of the Rydberg wavepacket. A simulation of the Ar $3s^{-1}np$ dipole emission by solving the time-dependent Schrödinger equation (a) captures the extended decay times observed in the wave-mixing experiments. The Fourier transform of the simulated signal (b) further matches the coherent oscillatory signatures observed as the Rydberg wavepacket propagates. The experimental wave-mixing spectrum from Figure 5.2(a) is Fourier transformed for comparison to the result in (b). The solid black boxes in (b) and (c) highlight the retrieved beat frequencies that match the energy differences between the np and (n+1)p Rydberg states, consistent with the wavepacket decomposition trends shown in Figure 5.3(b) and 5.3(f). The grey box in (b) shows an additional coherence contribution relevant for the $3s^{-1}6p$ emission, as discussed in the text. Peaks i-iv from the experimental analysis in Figures 5.3 (d) and 5.3 (h) are labeled in green.

5.4 Discussion

The coherent nature of the dynamics involving many Rydberg eigenstates is on full display in the presented experiments and accompanying theory, as the oscillatory intensity of the *np* FWM emission extends much longer than expected. For example, the $3s^{-1}5p$ emission has visible oscillations out to ~150-200 fs even though the $3s^{-1}6p$ autoionization lifetime is 52.2 fs. Although higher *n* members of the Rydberg series make up small portions of the amplitude distribution in the fitted FWM emissions, they are still part of the coherent superposition and thus exert influence over its time-dependence. The agreement between the experimental FWM signals and the simulated results shows that the detected coherent wave packet dynamics are largely driven by the transition dipoles of the NIR coupled states in the excited $3s^{-1}np$ Ar system itself, even though there are no XUV-forbidden states ($3s^{-1}ns/d$) to complete the wave-mixing pathways lying within the NIR bandwidth. By contrast, previous FWM experiments on the Kr $4s^24p^5nl$ autoionizing

Rydberg series used NIR-resonant $4p^{-1}np$ states to measure $4s^24p^5nl$ state lifetimes that matched frequency-domain lifetime predictions [11]. Theoretical investigations of similar off-resonant conditions in attosecond transient absorption spectroscopy also show that the dynamics can be governed largely by transition dipole moments and coherent dephasing rather than by population transfer and relaxation, as occurs when on resonance [158].

The results in this Chapter may be considered through the lens of wave packet reshaping where coherent amplitude transfer, which occurs through non-resonant NIR light-matter interactions, changes the amplitude coefficients in the superposition of the detected coherence in relation to the initial XUV excited Rydberg wave packet. These FWM studies of Ar Rydberg wave packets show that a systematic alteration of autoionization events is possible that is intrinsic to the system itself after a Rydberg wave packet is launched. As the amplitude distributions show from the wave packet decomposition in Figure 5.3, the off-resonant NIR interactions have the effect of redistributing, or transferring, amplitude among the Rydberg eigenstates that compose the coherent superposition – i.e., from the $3s^{-1}(n+1)p$ states to the $3s^{-1}np$ states. Importantly, the nature of the coherent amplitude transfer relies upon the transition dipole moments connecting $3s^{-1}np$, $3s^{-1}ns$, and $3s^{-1}nd$ states within the excited state system. It is also significant that the FWM emission decays of the autoionizing *np* states are extended here, rather than shortened, with respect to their literature line-width values. Other time-dependent wave packet studies have shown detected coherence lifetimes decaying on the timescale of the shorter-lived components in the superposition [159]. Attosecond transient absorption spectroscopy has been used to measure Ar $3s^{-1}4p$ and $3s^{-1}5p$ decay times consistent with frequency domain literature due to NIR coupling with continuum states or, for the $3s^{-1}4p$ state, through resonant dark states accessed by one NIR photon [86]. The non-resonant NIR-coupled pathways in this attosecond FWM experiment show that the transition dipole moments connecting the $(n+1)s$ and $(n-1)d$ dark states to the *np* states maintain the coherence in the detected superposition, allowing for the *np* state to be detected through its quantum interference with the $(n+1)p$ state long after its autoionization lifetime. The coherent amplitude transfer dynamic reported here sheds new light on important and complex coherent detection dynamics of autoionizing states that are ultimately governed by electron-electron correlations.

There is a longstanding interest in coherently controlling excited state processes with systems ranging in complexity from prototypical atomic Rydberg wave packets [148,160-164] to mixed electronic, vibrational, and rotational wave packets in small molecules [159,165,166]. Often, the approach to controlling wave packet dynamics surrounds the preparation of the coherent superposition using pulse shaping methods with iterative feedback to "customize" the wave packet composition for particular trajectories. The results in this study do not go as far as coherent control. Frequency-domain pulse shaping methods have been previously used in the attosecond FWM experiment to analyze the NIR-frequency dependence of an attosecond FWM experiment on the Ar $3s^23p^5$ *ns/nd* autoionizing Rydberg series [10]. In this application the few-cycle NIR light-matter interactions were on resonance with optically dark $3s^23p^5$ 4p states, which enabled the isolation of specific wave-mixing pathways from the coherences using the pulse shaper. Other more recent experiments have targeted the $3s^23p^5$ *nf* autoionizing Rydberg series in Ar in which Rydberg wave packet control is probed through narrower band Raman transitions and using photoelectron-based detection [167]. In contrast, the results presented

here provide important insight about the role that non-resonant NIR light-matter interactions can have in coherently transferring amplitude during the attosecond FWM process. More broadly, this work emphasizes the importance of carefully considering the nature of each light-matter interaction and coherence transfer during the probing stages of an initially excited wave packet.

5.5 Conclusion

We have reported attosecond FWM spectra of the Ar $3s^{-1}np$ autoionizing Rydberg series around 27-29 eV. This investigation highlights the important role of non-resonant NIR light-matter interactions in probing XUV-excited Rydberg wave packets. The reported experiments and analysis reveal a mechanism of coherent amplitude transfer arising from the non-resonant NIR light-matter interactions that explain the detected FWM emission coherence decays. Importantly, this work identifies the specific optically dark $(n+1)s$ and $(n-1)d$ states that are responsible for transferring $(n+1)p$ character to the np states, from which the FWM emissions are detected. This results in the apparent lifetimes of Rydberg states other than the directly observed individual emissions dominating the FWM coherence decays. The overarching importance of a careful consideration of each light-matter interaction in the attosecond FWM process is emphasized in this work. The insight contributed by this work also has wide ranging implications for current work in quantum information science, where the steps of creation, manipulation, and readout of coherent states are crucial to the performance and robustness of future quantum technologies.

5.6 Appendix A: Experimental Parameters

The equations used to fit the attosecond FWM lineouts are described in the main text. The 5p and 6p states were sufficiently fit using a wave packet of the $3s^{-1}np$ states where $4 \leq n \leq 10$, while the 7p state required up to n=15. The autoionizing Rydberg state energies were obtained from literature values [152,156]. The autoionizing lifetimes for the $3s^{-1}np$ Rydberg states have been reported in the literature up to n=8. In order to constrain the autoionizing lifetimes, τ, for all Rydberg states used in the wave packet model, the lifetimes for the $4 \leq n \leq 8$ states in the series were compiled from the literature [152,153,156] and fit to the well-known cubic scaling law for autoionizing lifetimes [144-146], $\tau = \tau_0(n-\delta)^3$ where τ_0 is a proportionality constant and δ is the known quantum defect. Using this fit, the higher members of the Rydberg series that are not available in the literature are able to be included in the analysis in a consistent manner with the known lifetimes of the lower n members. The cubic scaling fit is shown below in Figure 5.6 for extrapolating higher n member lifetimes.

5.6.1 The Ar $3s^{-1}7p$ Lineout Fit

As noted in the Chapter above, the wave packet model fitting becomes less robust as the stationary Rydberg eigenstates composing the wave packet become closer in energy, which clearly begins to affect the fitting in the 7p lineout. The 7p lineout is shown below in Figure 5.7.

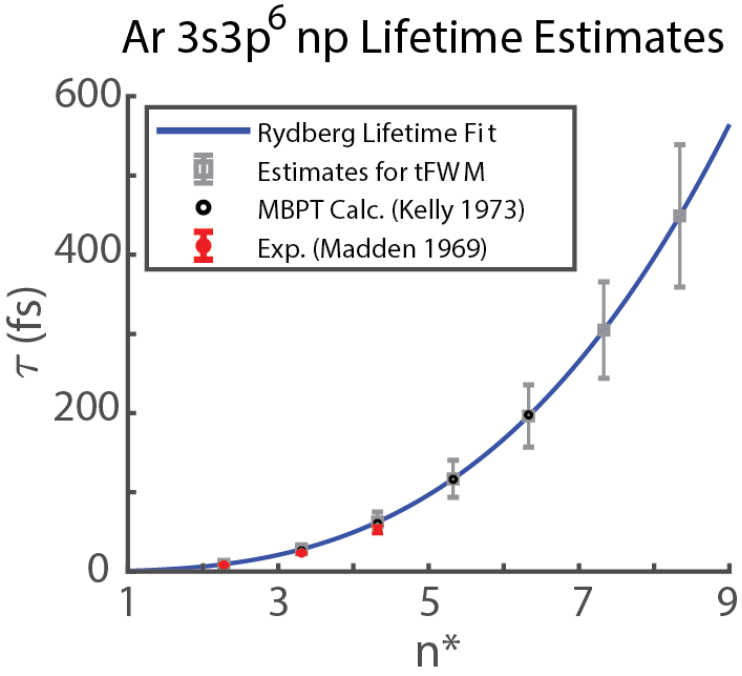

Figure 5.6 Determining autoionization lifetimes of higher members (n>8) of Ar $3s^{-1}np$ autoionizing Rydberg series. The blue fit is used to determine the autoionization lifetime of the higher n members in the wave packet model used to fit the attosecond FWM spectra shown in Figure 5.3.

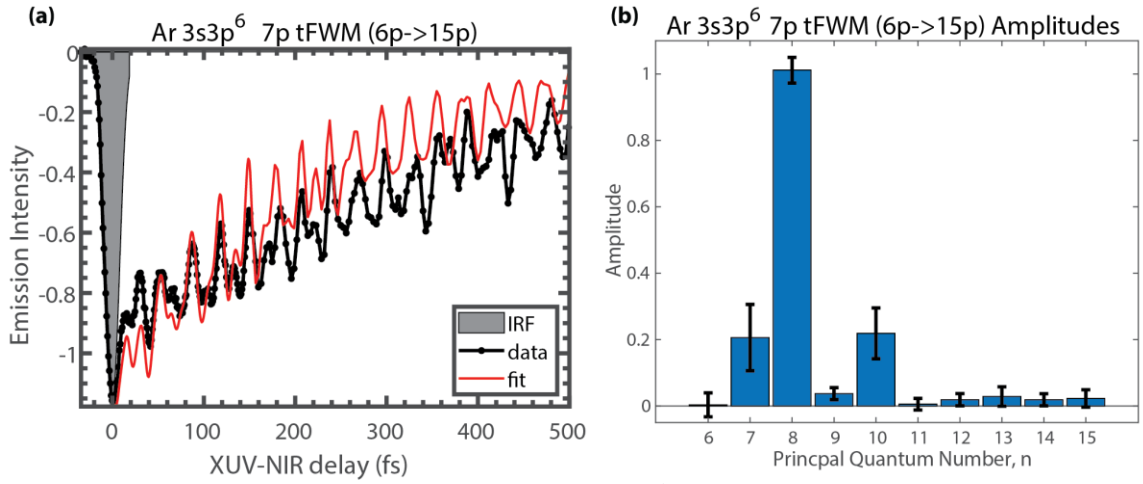

Figure 5. 7 Wave packet model fitting of the Ar $3s^{-1}7p$ lineout. The fit to the experimental data is shown (a) and the extracted amplitude coefficients are shown in (b).

5.6.2 The Fitted Parameters of the Ar $3s^{-1}$ 5p, 6p, and 7p Lineouts.

The Levenburg-Marquardt algorithm was used in a nonlinear least squares fitting routine using the wave packet model equation given in the main text. The amplitude coefficients, a_n, were optimized to fit the experimental data by the fitting algorithm, while the autoionizing linewidth (lifetime), Γ_n (τ_n), and eigenstate energy, ω_n, were initially set to literature-obtained values and then constrained with upper and lower boundaries in the

fitting algorithm to enable convergence. The autoionizing lifetimes were obtained as described above in Section 5.6 based on available literature; the eigenstate energies were given upper and lower boundaries separated by 10 meV to approximate the 11 meV instrumental spectral resolution and enable the fitting algorithm to converge effectively. The phase, ϕ_n, was allowed to float over the range $-\pi$ to π radians during fit optimization (see Tables 5.2, 5.3, and 5.4).

As can be seen from the higher member fitted parameters, especially those for $n \geq 8$, the narrow linewidths are too narrow to be spectrally resolved and they begin to complicate the physical accuracy of the fit.

n	a_n	ϕ_n ***[radians]***	Γ_n (τ_n) ***[eV]***	τ_n ***[fs]***	ω_n ***[eV]***
4	0.00959	2.752	0.090	7.31	26.61
5	0.04113	2.592	0.029	22.46	27.98
6	0.7137	0.822	0.012	54.47	28.49
7	0.00829	-0.488	0.007	93.60	28.78
8	0.00682	-1.925	0.004	157.00	28.91
9	0.03638	-2.643	0.003	243.80	28.98
10	0.00689	0.212	0.002	359.20	29.03

Table 5.2 $3s^{-1}5p$ Fit; $R^2 = 0.99$

n	a_n	ϕ_n ***[radians]***	Γ_n (τ_n) ***[eV]***	τ_n ***[fs]***	ω_n ***[eV]***
4	0.00441	-2.406	0.090	7.31	26.63
5	0.00644	3.142	0.020	33.43	28.00
6	0.1062	0.382	0.009	74.93	28.51
7	0.9393	-0.096	0.005	140.40	28.76
8	0.00753	1.487	0.003	235.30	28.89
9	0.1446	-3.142	0.002	365.80	29.00
10	0.00807	-0.230	0.002	359.20	29.04

Table 5.3 $3s^{-1}6p$ Fit; $R^2 = 0.99$

n	a_n	ϕ_n ***[radians]***	Γ_n (τ_n) ***[eV]***	τ_n ***[fs]***	ω_n ***[eV]***
6	0.00328	-0.9799	0.009	74.9	28.52
7	0.206	-0.8908	0.005	140.4	29.17
8	1.012	-1.143	0.003	235.6	28.74
9	0.037	-0.1997	0.003	243.8	28.88
10	0.2189	1.920	0.001	538.8	29.00
11	0.00540	-0.4899	0.001	550.0	29.02
12	0.01882	-3.139	0.001	1100	29.08
13	0.02858	3.142	0.0004	1499	29.10
14	0.01892	-1.579	0.0004	1700	29.12
15	0.02274	-1.724	0.0003	2400	29.15

Table 5.4 $3s^{-1}7p$ Fit; $R^2 = 0.99$

5.7 Appendix B: Computational Methods

5.7.1 TDSE Simulation

The core-level time-dependent absorption response of argon atoms is simulated by numerically solving the TDSE for the discrete electronic levels,

$$i\frac{\partial}{\partial t}c_n(t) = \epsilon_n - \frac{i\Gamma_n}{2} - \sum_{m\neq n} d_{n,m}E(t) \quad (5.1)$$

In Equation (5.1), $c_n(t)$ is the complex coefficient for the nth electronic state, ϵ_n is the state energy, Γ_n is the autoionization lifetime of the core-excited states obtained in the same way as used for the wave packet modeling and described above in Figure 5.6, E(t) is the laser electric field, and $d_{n,m}$ is the transition dipole moment between the n^{th} and m^{th} states. The electronic structure of argon is computed as described below. The extreme ultraviolet absorption signals are obtained by calculating the single-atom absorption cross section,

$$\sigma(\omega) \propto \omega\, Im\left[\frac{d(\omega)}{E(\omega)}\right] \quad (5.2)$$

where $d(\omega)$ and $E(\omega)$ are the Fourier-transformed dipole moments and applied laser field, respectively [158].The laser electric field consists of a NIR pump pulse (750 nm, 4 fs, 5x10^{11} W/cm^2) and an extreme ultraviolet pulse (40 nm, 80 as, 1x10^{10} W/cm^2). The equation is solved by the fourth-order Runge-Kutta method at a step size of 6 as.

5.7.2 Oscillator Strengths

The electronic structure of argon was computed by using the atomic structure calculation code of Cowan, which is based on a multiconfiguration Hartree-Fock model with empirically adjusted Slater parameters [157].The simulation includes 20 electronic states: the ground state, the $3s^{-1}np$ states ($4 \leq n \leq 9$), $3s^{-1}ns$ states ($4 \leq n \leq 9$), and the $3s^{-1}nd$ states ($3 \leq n \leq 9$). The state energies are given below, as well as the calculated oscillator strengths for the $p\rightarrow s$ and $p\rightarrow d$ transitions (see Table 5.5, 5.6, and 5.7).

$3s^{-1}$ *np*	Energy (eV)	$3s^{-1}$ *ns*	Energy (eV)	$3s^{-1}$ *nd*	Energy (eV)
4p	26.594	4s	25.305	3d	27.554
5p	27.999	5s	27.630	4d	28.306
6p	28.513	6s	28.354	5d	28.652
7p	28.761	7s	28.679	6d	28.837
8p	28.901	8s	28.853	7d	28.947
9p	28.987	9s	28.957	8d	29.018
-	-	-	-	9d	29.066

Table 5.5 Calculated Argon Rydberg State Energies

np	4s	5s	6s	7s	8s	9s
4p	0.35146	0.17195	0.02152	0.00785	0.00395	0.00223
5p	0.00066	0.49417	0.30052	0.03288	0.01177	0.00604
6p	0.00002	0.00282	0.63662	0.42942	0.04497	0.01652
7p	0.00023	0.00005	0.00551	0.77603	0.55703	0.05941
8p	0.00077	0.00015	0.00017	0.00750	0.90966	0.69965
9p	0.00961	0.00556	0.00320	0.00091	0.00206	0.93299

Table 5.6 Calculated Oscillator Strengths, np→ns

np	3d	4d	5d	6d	7d	8d	9d
4p	0.16402	0.00013	0.00119	0.00124	0.00123	0.00272	0.00093
5p	0.04885	0.23818	0.00071	0.00009	0.00035	0.00135	0.00034
6p	0.00423	0.10278	0.30473	0.00284	0.00005	0.00040	0.00002
7p	0.00173	0.00897	0.15809	0.36805	0.00562	0.00006	0.00026
8p	0.00105	0.00342	0.01361	0.21474	0.42845	0.00673	0.00290
9p	0.00077	0.00199	0.00510	0.01827	0.27600	0.46764	0.02398

Table 5.7 Calculated Oscillator Strengths, np→ns

Chapter 6: Conclusions

6.1 Summary of Accomplished Work

There is great interest in developing nonlinear spectroscopies in the XUV region. A table-top technique, attosecond FWM spectroscopy, has been successfully demonstrated, which generates nonlinear signals using an attosecond XUV pulse in combination with two few-cycle NIR pulses. The work detailed in this dissertation has broadened the scope of attosecond FWM spectroscopy. It includes the successful demonstration of probing ultrafast dynamics in molecules and exploring the potential of resonant and non-resonant FWM processes.

In Chapter 3, the precise time-domain measurement of an excited state lifetime in a molecule is first demonstrated with attosecond FWM spectroscopy. This study showed that coupled electronic-nuclear dynamics in gaseous O_2 dictates the relaxation of the 3s Rydberg state in the ionic c $^4\Sigma_u^-$ state series. The 3s Rydberg state supports v=0 and 1 vibrational levels at 20.85 eV and 21.05 eV, respectively, and includes competing autoionization and dissociation decay channels. These decay channels are isolated experimentally from other FWM signals by adjusting the overlap angles of the two noncollinear NIR beams, revealing 5.8 ± 0.5 fs and 4.3 ± 0.7 fs lifetimes for the v=0 and v=1 states, respectively. Theoretical lifetime results of 5.6 fs and 4.8 fs, respectively, match the experimental values very well and provide deeper insight into the dominant decay mechanisms. While predissociation might appear to explain the different lifetimes, theory suggests autoionization dominates the decay for both vibrational states and that nuclear motion can affect this autoionization rate.

In Chapter 4, attosecond FWM spectroscopy is utilized in combination with theory to elucidate the complex nonlinear spectroscopy of short-lived, autoionizing Rydberg states in the polyatomic molecule, CO_2. The photoabsorption spectrum of the linear triatomic molecule CO_2 around 17-18 eV consists of several ionic states and overlapping manifolds of neutral Rydberg states, such as the Henning Diffuse and Sharp series that converge to the ionic B $^2\Sigma_u^+$ state. The inhomogeneous distribution of states in this region requires direct time-domain measurements with nonlinear methods to establish the lifetimes and couplings of these states. The attosecond FWM measurements show the emission from the $nd\sigma_g$ Sharp states (n=5-7) decaying with times of 33±6 fs, 53±2 fs, and 94±2 fs, respectively, which correspond to the lifetimes of the n=6-8 states of the $ns\sigma_g$ Diffuse series. The calculated oscillator strengths reveal enhancement for the diffuse-to-sharp pathways relative to the sharp-to-sharp pathways, in addition to identifying the NIR-resonant $^1\Sigma_g^+$[3pσ_u B $^2\Sigma_u^+$] dark state that favors the diffuse-to-sharp pathway. This work demonstrates that the effects of spectral congestion and inhomogeneous broadening may be circumvented in measuring very short-lived excited states, with careful consideration of the quantum transition pathways available to an excited atom or molecule.

In Chapter 5, wave packet dynamics and non-resonant NIR interactions in Ar are explored by attosecond FWM spectroscopy. Investigations of the inner valence excitations of the autoionizing $3s^{-1}$ np Rydberg states of gaseous Ar around 29 eV reveal coherent dynamics with underlying decay times uncharacteristic of the emitting states, similar to CO_2. However, in Ar the decays of the emitting $3s^{-1}$np Rydberg states are extended beyond their expected lifetimes and similar to the $3s^{-1}$(n+1)p Rydberg state lifetimes. The strong

modulated time-dependent emission measured by attosecond FWM enabled an in-depth wave packet decomposition analysis that explains the observed behavior as a coherent amplitude transfer that occurs predominantly from $3s^{-1}$ (n+1)p Rydberg states to the emitting $3s^{-1}$np Rydberg states. Calculating the oscillator strengths for the transitions between the bright $3s^{-1}$np Rydberg states and the dark $3s^{-1}$ ns/nd dark states shows that the coherent amplitude transfer is facilitated through the $3s^{-1}$ (n+1)s and (n-1)d dark states, which are energetically far-off-resonance with the few-cycle NIR pulses used in the experiment. These experimental observations are also reproduced by simulations based on solving the time-dependent Schrödinger equation. In general, the results show that coherent wave packet dynamics driven non-resonantly are accurately characterized with attosecond FWM spectroscopy.

6.2 Experiments with New Apparatus

As discussed in the Chapter 2, a new apparatus was implemented at end of the 2021. The renovation involved installing a new high-powered laser and making key updrades modifications to the vacuum chambers, with the aim of generating XUV pulses with improved flux and extending FWM experiments to higher XUV and X-ray photon energies. Two experiments have been conducted with the new apparatus, including measurements in the Ne inner valence excited states around 45 eV and Xe core excited state around 65 eV.

6.2.1 Ne Inner Valence Excited States around 45 eV

An experiment to measure autoionization decay lifetimes of inner valence electronic excitations in Ne atoms around 45 eV is performed with the new apparatus. This work is already published and only a brief description is provided in this section [18].

In the experiments, the XUV photon can excite Ne to an inner valence excited bright state, $2s^{-1}3p$, and the $2s^{-1}3s$ and 3d dark states in Ne are resonantly accessible to a NIR photon following an XUV-driven $2s^{-1}3p$ excitation. By controlling delays and the pulse sequence of NIR pulses, as discussed in Chapter 1, the autoionization lifetimes of both optically bright states and optically dark states can be directly characterized in the time-domain with attosecond FWM spectroscopy. The systematic investigation of autoionization decays from orbital angular momentum states with different amounts of core hole penetration of the 2s shell show increasing decay times of 7±2 fs, 48±8 fs, and 427±40 fs for the 3s, 3p, and 3d electrons, respectively. Ab initio calculations provide lifetime values that agree with the time-domain measurements and qualitatively explain the lifetime trend dependence on the extent to which the n=3 Rydberg orbitals penetrate the innermost electron shells of the Ne atoms. This work serves as a benchmark for probing dynamics of resonantly accessible dark states with attosecond FWM spectroscopy.

6.2.2 Xe Core Excited State Around 65 eV

The experiment on Xe around 65 eV is still ongoing, and some preliminary results will be provided in this section.

The absorption edges of core-level electrons are typically well separated for different elements, and they are highly sensitive to the electronic environment and nearby molecular structures. As a result, spectroscopies involving core-excited states can offer an element-specific and localized probe of ultrafast dynamics occurring in molecules, marking

the next frontier of attosecond spectroscopies. Attosecond FWM spectroscopy is intended to be applied to core-excited states, and Xe serves as the initial benchmark target for this investigation.

Xe is selected as the target because the behavior of its $4d^{-1}$ core-excited state around 65 eV is well-characterized [168-174]. Linewidth measurements for different bright states were performed to determine the Auger decay lifetimes in those states [168-170]. Additionally, it has been shown that two dark states, $4d^{-1}6s$ and $4d^{-1}6d$, can be resonantly accessed through the $4d^{-1}6p$ bright state with NIR photon, and the transition dipole moments were studied as well [171-174]. This makes Xe an ideal candidate for conducting the first attosecond FWM experiments on core level states.

A camera image of the FWM signals when all XUV and NIR pulses are temporally overlapped is shown in Figure 6.1 (a). This camera image is masked to eliminate the blooming background from XUV pulses, as discussed in Chapter 2, and only FWM signals emitted at negative angle are shown. There are three distinct features in this camera image, corresponding to $4d_{5/2}^{-1}6p$, $4d_{5/2}^{-1}7p$, and $4d_{5/2}^{-1}8p$, respectively. A bright state scan is performed on the strongest feature $4d_{5/2}^{-1}6p$ at a NIR power of about $5*10^{12}$ W/cm^2, yielding a Auger decay lifetime of 7±2 fs in this state. This lifetime value agrees with the literature value calculated from linewidth measurements as shown in Table 6.1.

An interesting NIR power-dependent behavior is observed during the experiments but has yet to be explained properly. As shown in Figure 6.2 (a)-(c), when the NIR power increases, the fitted lifetime in the bright state becomes longer. A hypothesis is that at high power, the NIR pulse can drive strong Rabi Cycling between the bright states and nearby dark states, and thus a lifetime mixture between the two is measured. Complementary results of dark state scans with different NIR power are provided in Figure 6.2 (d). The results of these scans cannot be fitted with a single decay and contain some oscillations, which indicates that multiple dark states are involved in the experiments. However, at a glance, the dark state features persist longer than the bright state features and decay faster at higher power, which is in agreement with the hypothesis. Experiments to separate the pathways of different dark states, as well as increasing the power to capture the Rabi oscillations directly, are on-going and are expected to provide more evidence.

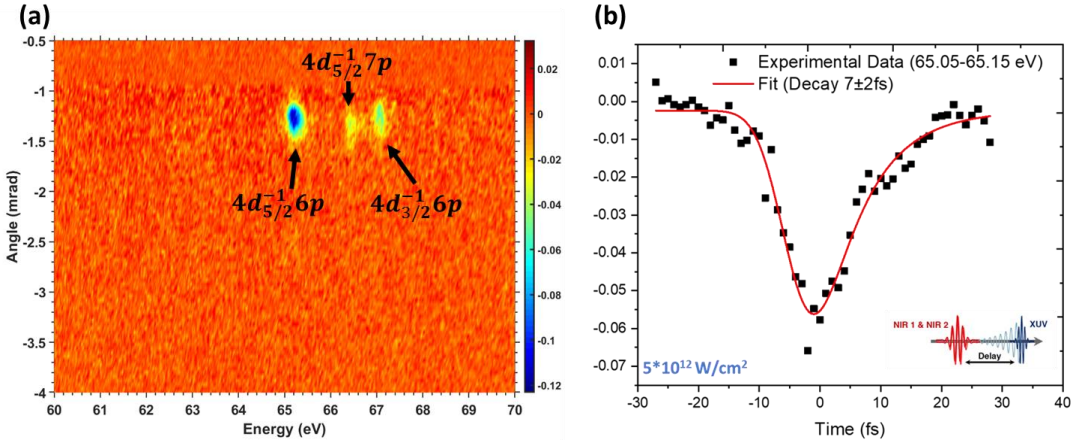

Figure 6.1 ***Preliminary results in Xe $4d^{-1}$ core-excited state around 65 eV.*** *(a) A camera image of FWM signals emitted at negative emission angle is shown and three features are characterized. (b) Bright state scan is applied to the feature with photon energy ranging from 65.05-65.15 eV, corresponding to the $4d_{5/2}^{-1}6p$ state.*

Reference	Linewidth (meV)	Lifetime (fs)
This work		7±2
O.-P. Sairanen *et al. Phys. Rev. A* **54**, 2834 (1996)	109.8 ± 1.0	~6
G C King *et al., J. Phys. B: Atom. Mol. Phys.* **10** 2479 (1977)	111 ± 4	~5.9
S Masui *et al., J. Phys. B: At. Mol. Opt. Phys.* **28** 4529 (1995)	106.3 ± 0.5	~6.2

Table 6.1 ***Lifetime comparison between the current work and the reference.*** *The current work is performed in time domain and lifetime is obtained directly, while the values in the literature are converted from the linewidth measurements.*

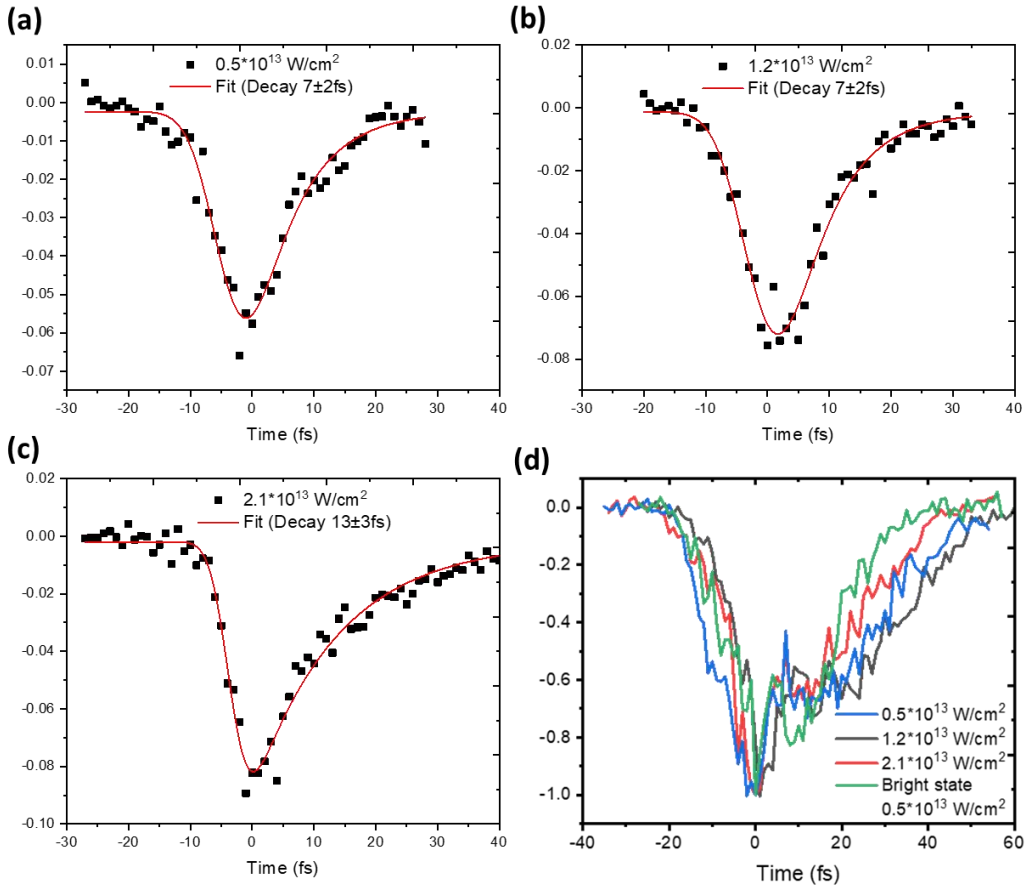

Figure 6.2 ***Power dependent results for feature emitted at*** $4d_{5/2}^{-1}6p$***.*** *Bright state scans are performed at NIR power of (a) 0.5*10^13 W/cm^2, (b) 1.2*10^13 W/cm^2, and (c) 2.1*10^13 W/cm^2. (d) Dark state scans with these three powers are shown in blue, black, and red line, respectively, while a green line shows the decay for bright state scan at low power for comparison.*

6.3 Future Direction

Ongoing efforts are being made to further advance the development of nonlinear spectroscopy in the short wavelength range. Several modifications will be implemented in the apparatus to conduct experiments in the carbon K-edge region (~300 eV). A prospective experimental scheme is shown in Figure 6.3. Briefly, the modifications involve generating attosecond soft X-ray pulses and generating shorter wavelength probe pulses, such as in blue (~400 nm) or UV (~266 nm) region, which will be discussed in separate sections.

6.3.1 Generating Attosecond X-ray Pulses Toward Carbon K-edge

The cutoff photon energy of the HHG process is described by Equation (1.50) and can be related to the wavelength of the driving field λ:

$$E_{Cutoff} \propto I\lambda^2 \tag{6.1}$$

Here, I is the intensity of the pulse. To extend the cutoff energy of attosecond pulses, an OPA (HE-TOPAS Prime Plus, Light Conversion) will be used to convert the 800 nm output of the Legend Elite Duo HE+ to a longer wavelength of 1.3-1.5 μm. However, the efficiency of HHG process also decreases dramatically with λ^{-6} scaling [175], leading to low X-ray flux. To overcome this limitation, a high pressure of helium, typically several bars, as well as longer HHG interaction region are typically employed to increase the flux [176-180]. A newly designed HHG cell with semi-infinite gas cell setup and differential pumping will be implemented to achieve those conditions, as shown in Figure 6.4.

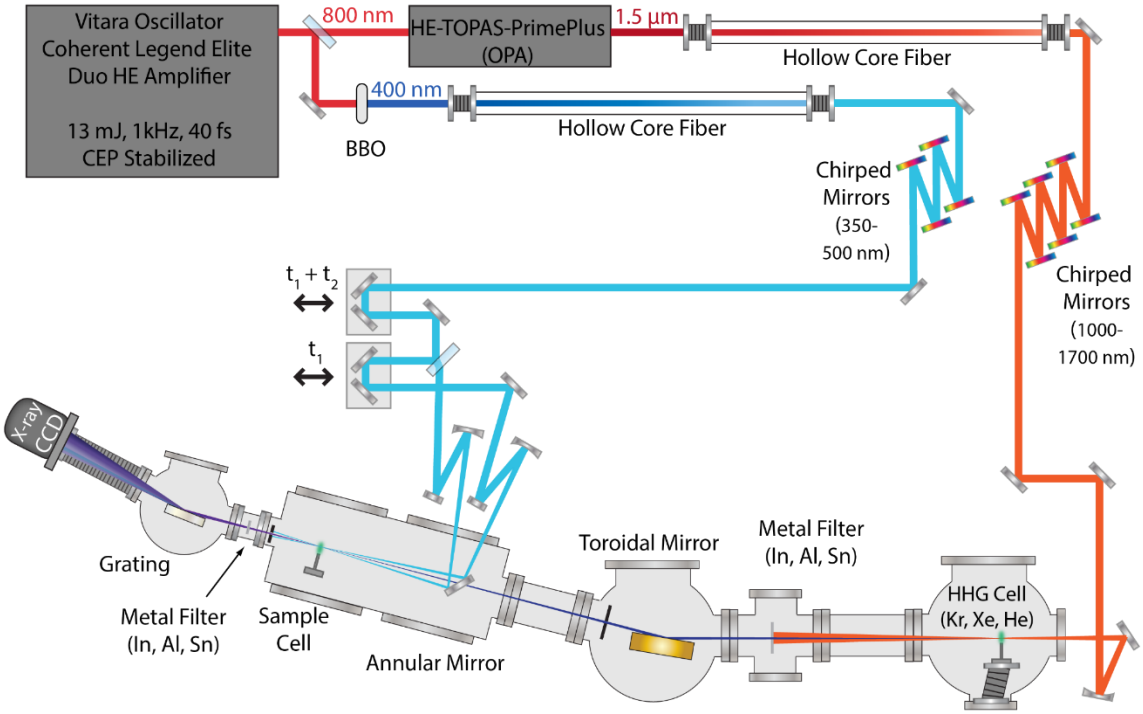

Figure 6.3 ***Schematic of prospective experimental setup.*** *An OPA will be employed to convert 800 nm NIR pulse to a longer wavelength of 1.3-1.5 μm, thereby extending the cutoff of HHG process and generating soft X-rays toward Carbon K-edge (300 eV). The 800 nm will also be frequency-doubled to 400 nm for the probe arms.*

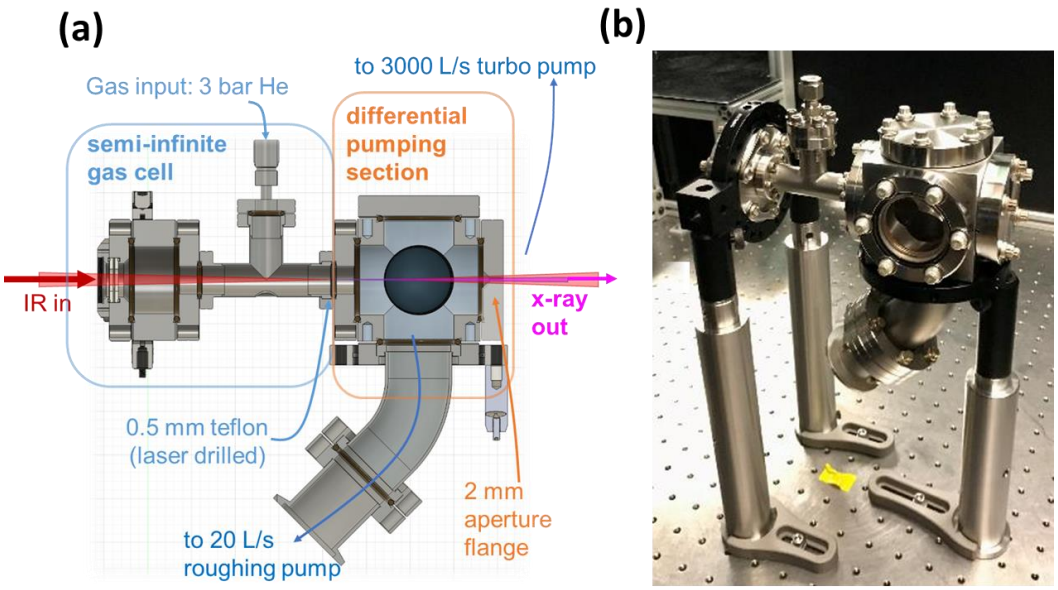

Figure 6.4 ***A newly designed HHG cell.*** *(a) A Schematic of the newly designed cell and (b) a picture of the assembled cell are shown. A semi-infinite gas cell is utilized to extend the length of the HHG interaction region. With the differential pumping scheme, the system can withstand 3 bars of He in the semi-infinite gas cell while maintaining high vacuum in the chamber.*

Another critical factor affecting the X-ray flux is the reflectivity of the X-ray optics. As described in Chapter 2, the current setup uses a gold coated toroidal mirror and grating to reflect the XUV pulse. However, at the photon energy of the carbon K-edge, nickel is shown to have almost two times the reflectively of gold as shown in Figure 6.5 (a). Hence, the optics will be altered to nickel coated to increase the X-ray flux. While the nickel coated toroidal mirror can be purchased, the nickel coated grating is not commercially available, and a gold-coated grating was re-coated with nickel by the CXRO facility as shown in Figure 6.5 (b), (c).

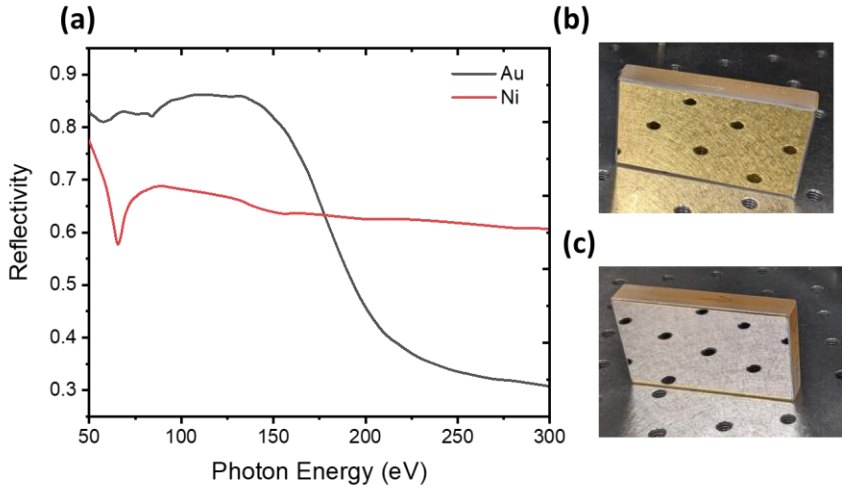

Figure 6.5 ***Choice of X-ray optics.*** *(a)The reflectivity of both gold and Ni are shown at reflection angle of 5°. (b) A gold-coated grating is re-coated with Ni as shown in figure (c).*

6.3.2 *Generating 400 nm and UV Pulses*

As discussed in the Chapter 2, with increasing X-ray photon energies, the emission angle of the FWM signals become smaller. To achieve better separation of the FWM signals, higher photon energies or shorter wavelengths of the probe are required. The 800 nm will be frequency-doubled into 400 nm by a BBO crystal. To achieve the short pulse duration of 400 nm, two methods are considered. The first method involves doubling the long 800 nm pulse and then using a hollow core fiber to spectrally broaden the resulting 400 nm pulse. Subsequently, the pulse is recompressed using 400 nm chirped mirrors, as shown in Figure 6.3. Alternatively, the second method entails doubling the few-cycle 800 nm pulse and compensating for the dispersion introduced by the BBO, as shown in Figure 6.6. Figure 6.6 also illustrates the scheme for generating even shorter wavelength UV pulses at 266 nm. The UV pulses can be utilized as an actinic pulse to initiate the photodissociation of molecule in their excited state, allowing the probing of dynamics with increasing bond distance.

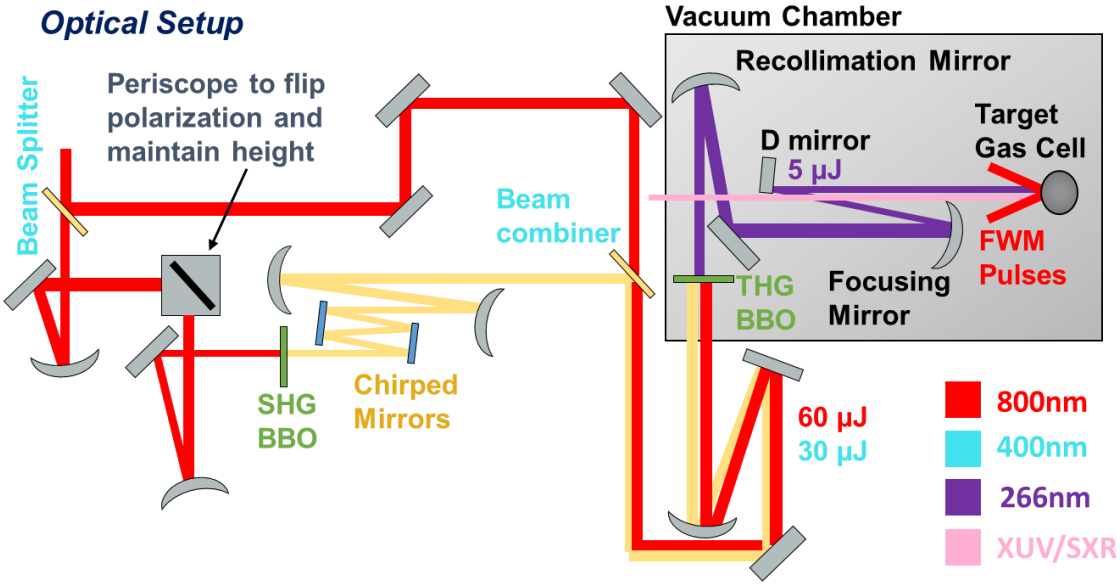

Figure 6.6 ***A schematic of generating 400nm and UV pulses.*** *The few-cycle 800 nm pulses are first split, and part of the beam is frequency-doubled by a BBO crystal, followed by pulse compression with chirped mirrors to generate short 400 nm pulses. The remaining 800 nm beam is combined with 400 nm pulses to generate UV pulses (~266 nm) through sum frenquency generation.*

6.3.3 *Proposed Future Experiments*

With the capability to generate attosecond X-ray pulses, short 400 nm, and UV pulses, a wide range of experiments become possible. Two future experiments are proposed below.

By preparing a system with an actinic photoexcitation UV pulse prior to the FWM pulse sequence, core-excited state lifetimes and their decay channels during photochemical reactions will be directly measured. For example, the photodissociation reaction of ICl will systematically increase the I-Cl bond distance over time, which will be triggered by an UV

pulse at 266 nm. An XUV FWM pulse sequence will then be introduced sequentially to monitor core-excited state lifetimes around the iodine $N_{4,5}$ edge as a function of I-Cl bond length at 50-55 eV. The predicted bond-length dependence of the I- and Cl-centric decay mechanisms of the core-excited states will be directly tested [29], resulting in a more sophisticated understanding of molecular core-hole decay in a heteronuclear diatomic system. Building upon this experiment, CH_3I will be studied similarly by exciting the dissociative $^3Q_0$ state with the 266 nm actinic pulse to trigger lengthening of the C-I bond distance. The XUV pulse at the iodine $N_{4,5}$ edge will produce core-excited states sensitive to this dissociation that are probed by FWM emissions following non-collinear UV-visible pulses.

At the carbon K-edge, a specific aspect of electron correlation will be investigated in formaldehyde (CH_2O), where there is a doubly excited state, C 1s $2b_2(n) - (\pi^*)^2$, predicted to be ~2.3 eV above the C 1s-π^* core-excited state and ~2.8 eV below the C 1s-3p states [181]. This dark state is formed by exciting both a C 1s electron and a non-bonding O electron into a doubly excited $(\pi^*)^2$ state. The ground state n-π^* transition is known to be higher in energy than the predicted n-π^* transition that forms the $(\pi^*)^2$ state starting from the C 1s-π^* core-excited state [181,182], but the energy of the doubly excited state needs experimental confirmation to characterize the electron correlation and core-valence coupling resulting in this energy difference. The energy and dynamics of this dark state will be characterized for the first-time using V-type pathways with UV wave-mixing pulses or Λ-type pathways with NIR pulses. The energetic position relative to each bright state is determined using a pulse shaper in the UV or NIR pulses to perform a multidimensional experiment. Such a measurement is only accessible through the attosecond FWM technique. Similar studies of other carbonyl-containing molecules, like acetaldehyde or acetone, will show how the chemical environment and core-valence coupling affect this electron-electron correlation.

6.4 Conclusion

In conclusion, nonlinear spectroscopies in the short wavelength region are of great interest because of their capability for achieving better temporal and spatial resolution as well as atomic spectral selectivity. Attosecond four-wave mixing, a tabletop nonlinear spectroscopy in the extreme ultraviolet has been demonstrated and has already proven its potential in exploring ultrafast processes in atomic and molecular systems. This dissertation has not only shown the power of attosecond FWM spectroscopy but has also pushed its boundaries to new frontiers. Looking ahead, the upcoming implementation of attosecond FWM experiments in the carbon K-edge will offer new avenues for investigating chemically and biologically significant organic molecules with nonlinear spectroscopies. Overall, attosecond FWM spectroscopy serves as a solid foundation for future explorations in nonlinear spectroscopy at short wavelength, opening doors to innovative applications in various scientific fields.

Bibliography

[1] Schlau-Cohen, G. S. *et al.*, Pathways of Energy Flow in LHCII from Two-Dimensional Electronic Spectroscopy. *The journal of physical chemistry. B* **113,** 15352-15363 (2009).

[2] Ramasesha, K. *et al.*, Water vibrations have strongly mixed intra- and intermolecular character. *Nature chemistry* **5,** 935-940 (2013).

[3] Petti, M. K. *et al.*, Two-Dimensional Spectroscopy Is Being Used to Address Core Scientific Questions in Biology and Materials Science. *The journal of physical chemistry. B* **122,** 1771-1780 (2018).

[4] KRAUSE, J. L.,K. J. SCHAFER and K. C. KULANDER, High-order harmonic generation from atoms and ions in the high intensity regime. *Physical review letters* **68,** 3535-3538 (1992).

[5] Corkum, P. B., Plasma perspective on strong field multiphoton ionization. *Physical Review Letters* **71,** 1994 (1993).

[6] Cao, W. *et al.*, Near-resonant four-wave mixing of attosecond extreme-ultraviolet pulses with near-infrared pulses in neon: Detection of electronic coherences. *Physical review. A* **94,** 021802(R) (2016).

[7] Cao, W. *et al.*, Noncollinear wave mixing of attosecond XUV and few-cycle optical laser pulses in gas-phase atoms: Toward multidimensional spectroscopy involving XUV excitations. *Physical review. A* **94,** 053846 (2016).

[8] Cao, W. *et al.*, Excited-state vibronic wave-packet dynamics in H2 probed by XUV transient four-wave mixing. *Physical review. A* **97,** 023401 (2018).

[9] Warrick, E. R. *et al.*, Multiple pulse coherent dynamics and wave packet control of the N 2 a″ 1 Σ+g dark state by attosecond four-wave mixing. *Faraday discussions* **212,** 157-174 (2018).

[10] Marroux, H. J. B. *et al.*, Multidimensional spectroscopy with attosecond extreme ultraviolet and shaped near-infrared pulses. *Sci. Adv.* **4,** eaau3783 (2018).

[11] Fidler, A. P. *et al.*, Autoionization dynamics of (2P1/2)ns/d states in krypton probed by noncollinear wave mixing with attosecond extreme ultraviolet and few-cycle near infrared pulses. *The Journal of Chemical Physics* **151,** 114305 (2019).

[12] Fidler, A. P. *et al.*, Nonlinear XUV signal generation probed by transient grating spectroscopy with attosecond pulses. *Nat Commun* **10,** 1384 (2019).

[13] Fidler, A. P. *et al.*, Self-heterodyned detection of dressed state coherences in helium by noncollinear extreme ultraviolet wave mixing with attosecond pulses. *J. Phys. Photonics* **2,** 034003 (2020).

[14] Lin, Y. *et al.*, Coupled nuclear–electronic decay dynamics of O 2 inner valence excited states revealed by attosecond XUV wave-mixing spectroscopy. *Faraday discussions* **228,** 537-554 (2021).

[15] Gaynor, J. D. *et al.*, Solid state core-exciton dynamics in NaCl observed by tabletop attosecond four-wave mixing spectroscopy. *Physical review. B* **103,** 245140 (2021).

[16] Fidler, A. P. *et al.*, State-selective probing of CO2 autoionizing inner valence Rydberg states with attosecond extreme ultraviolet four-wave-mixing spectroscopy. *Physical review. A* **106,** 063525 (2022).

[17] Gaynor, J. D. *et al.*, Nonresonant coherent amplitude transfer in attosecond four-wave-mixing spectroscopy. *Physical review. A* **107,** 023526 (2023).

[18] Puskar, N. G. *et al.*, Measuring autoionization decay lifetimes of optically forbidden inner valence excited states in neon atoms with attosecond noncollinear four-wave-mixing spectroscopy. *Physical review. A* **107,** 033117 (2023).

[19] Leone, S. R. and Daniel M. Neumark, Probing matter with nonlinear spectroscopy. *Science* **379,** 6632 (2023).

[20] Thomas, N. C., The Early History of Spectroscopy. *Journal of Chemical Education* **68,** 631–634 (1991).

[21] Demtroder, W., *Molecular Physics*. (Wiley-VCH, 2005).

[22] Baldwin, G. C., *An Introduction to Nonlinear Optics*. (Plenum Publishing Corporation, 1974).

[23] Mukamel, S., *Principles of Nonlinear Optical Spectroscopy*. (Oxford University Press, 1995).

[24] Hamm, P. and M. T. Zanni, *Concepts and Methods of 2D Infrared Spectroscopy*. (Cambridge University Press, 2011).

[25] New, G., *Introduction to Nonlinear Optics*. (Cambridge University Press, 2011).

[26] Griffiths, D. J., *Introduction to Electrodynamics, 4th edition*. (Cambridge University Press, 2017).

[27] Dantus, M., Coherent nonlinear spectroscopy: from femtosecond dynamics to control. *Annual review of physical chemistry* **52,** 639-679 (2001).

[28] Beck, A. R.,Daniel M. Neumark and Stephen R. Leone, Probing ultrafast dynamics with attosecond transient absorption. *Chemical physics letters* **624,** 119-130 (2015).

[29] Marroux, H. J. B. *et al.*, Attosecond spectroscopy reveals alignment dependent core-hole dynamics in the ICl molecule. *Nature communications* **11,** 5810 (2020).

[30] GLOVER, T. E. *et al.*, X-ray and optical wave mixing. *Nature (London)* **488,** 603-608 (2012).

[31] Bencivenga, F. *et al.*, Four-wave mixing experiments with extreme ultraviolet transient gratings. *Nature* **520,** 205-208 (2015).

[32] Foglia, L. *et al.*, First Evidence of Purely Extreme-Ultraviolet Four-Wave Mixing. *Phys. Rev. Lett.* **120,**(2018).

[33] Mincigrucci, R. *et al.*, Advances in instrumentation for FEL-based four-wave-mixing experiments. *Nuclear instruments & methods in physics research. Section A, Accelerators, spectrometers, detectors and associated equipment* **907,** 132-148 (2018).

[34] Wright, J. C.,Daniel D. Kohler and Uwe Bergmann, X-ray/Extreme Ultraviolet Floquet State Multidimensional Spectroscopy, an Analogue of Multiple Quantum Nuclear Magnetic Resonance. *The journal of physical chemistry letters* **14,** 4908-4913 (2023).

[35] Cavaletto, S. M. *et al.*, *Attosecond Monitoring of Nonadiabatic Molecular Dynamics by Transient X-ray Transmission Spectroscopy.* (2023) 10.1021/acs.jctc.3c00062.

[36] Fano, Effects of Configuration Interaction on Intensities and Phase Shifts. *Physical review* **124,** 1866-1878 (1961).

[37] Pfeifer, T.,C. Spielmann and G. Gerber, Femtosecond x-ray science. *Reports on progress in physics* **69,** 443-505 (2006).

[38] Behrens, C. *et al.*, Few-femtosecond time-resolved measurements of X-ray free-electron lasers. *Nature communications* **5,** 3762 (2014).

[39] Attwood, D. and A. Sakdinawat, *X-rays and Extreme Ultraviolet Radiation: Principles
and Applications*. (Cambridge University Press, 2017).

[40] Schafer, K. *et al.*, Above threshold ionization beyond the high harmonic cutoff. *Physical review letters* **70,** 1599-1602 (1993).

[41] Antoine, P.,A. L'Huillier and M. Lewenstein, Attosecond Pulse Trains Using High–Order Harmonics. *Physical Review Letters* **77,** 1234-1237 (1996).

[42] Paul, P. M. *et al.*, Observation of a Train of Attosecond Pulses from High Harmonic Generation. *Science* **292,** 1689-1692 (2001).

[43] Chini, M.,Kun Zhao and Zenghu Chang, The generation, characterization and applications of broadband isolated attosecond pulses. *Nature photonics* **8,** 178-186 (2014).

[44] Warrick, E. R., *Attosecond Nonlinear Spectroscopy of Atoms and Molecules*. (PhD dissertation, University of California, Berkeley, 2017).

[45] Fidler, A. P., *Nonlinear Spectroscopy in the Extreme Ultraviolet: Probing Ultrafast Electronic Dynamics in Atoms, Molecules, and Solids with Attosecond Pulses*. (PhD dissertation, University of California, Berkeley, 2020).

[46] Gallmann, L. and U. Keller, *Femtosecond and Attosecond Light Sources and Techniques for*
Spectroscopy. Handbook of High-resolution Spectroscopy. (2011) https://doi.org/10.1002/9780470749593.hrs086.

[47] Nubling, R. K., Launch conditions and mode coupling in hollow-glass waveguides. *Opt. Eng.* **37,** 2454 (1998).

[48] Timmers, H. *et al.*, Generating high-contrast, near single-cycle waveforms with third-order dispersion compensation. *Optics letters* **42,** 811-814 (2017).

[49] Berry, R. S. and Svend Erik Nielsen, Dynamic Coupling Phenomena in Molecular Excited States. II. Autoionization and Predissociation in H 2 , Hd, and D 2. *Physical review. A, General physics* **1,** 395-411 (1970).

[50] GIUSTI-SUZOR, A. and C. JUNGEN, Theoretical study of competing photoionization and photodissociation processes in the NO molecule. *The Journal of chemical physics* **80,** 986-1000 (1984).

[51] LEFEBVRE-BRION, H. and F. KELLER, Competition between autoionization and predissociation in the HCl and DCl molecules. *The Journal of chemical physics* **90,** 7176-7183 (1989).

[52] Texier, F.,C. Jungen and SC Ross, Quantum beats and Kepler motion in fast competing photoionization and photodissociation processes. *Faraday discussions* **115,** 71-78 (2000).

[53] Hikosaka, Y. *et al.*, Competition between autoionization and dissociation in the [O2+(B 2Σg−)]nl and [O2+(c 4Σu−)]nl Rydberg states investigated by photon-induced dissociation to neutral fragments. *Journal of physics. B, Atomic, molecular, and optical physics* **36,** 4311-4326 (2003).

[54] Lefebvre-Brion, H. and Robert W. Field, *Theœ spectra and dynamics of diatomic molecules*. (Elsevier, Acad. Press, Amsterdam [u.a.], 2004).

[55] Heays, A. N.,A. D. Bosman and E. F. van Dishoeck, Photodissociation and photoionisation of atoms and molecules of astrophysical interest. *Astronomy & Astrophysics (0004-6361)* **602,** A105 (2017).

[56] Akahori, T. *et al.*, Dissociation processes of O 2 in the VUV region 500-700 AA. *Journal of physics. B, Atomic and molecular physics* **18,** 2219-2229 (1985).

[57] Evans, M. *et al.*, High-resolution pulsed field ionization photoelectron study of O2: Predissociation lifetimes and high-n Rydberg lifetimes converging to O2+(c 4Σu−, v+=0,1). *The Journal of chemical physics* **109,** 1285-1292 (1998).

[58] Liebel, H. *et al.*, De-excitation dynamics of Rydberg states in O2: I. Total cross sections for O I fluorescence emission following predissociation of 2σ-1u(c4Σ-u)nσg3Σ-u states. *Journal of physics. B, Atomic, molecular, and optical physics* **35,** 895 (2002).

[59] EHRESMANN, A. *et al.*, De-excitation dynamics of Rydberg states in O2. II: Vibrational and rotational structure of 2σ-1u(c 4Σ-u)(ns/nd)σg 3Σ-u(υ = 0, 1) states. *Journal of physics. B, Atomic, molecular, and optical physics* **37,** 4405-4422 (2004).

[60] Fan, L. *et al.*, Superexcited states of oxygen studied by fast-electron impact. *Physical review. A, Atomic, molecular, and optical physics* **71,** 032704 (2005).

[61] Doughty, B. *et al.*, Ultrafast decay of superexcited c 4Σu- nlσg v=0,1 states of O2 probed with femtosecond photoelectron spectroscopy. *The Journal of chemical physics* **136,** 214303 (2012).

[62] Timmers, H.,Niranjan Shivaram and Arvinder Sandhu, Ultrafast Dynamics of Neutral Superexcited Oxygen: A Direct Measurement of the Competition between Autoionization and Predissociation. *Physical review letters* **109,** 173001 (2012).

[63] Liao, C. *et al.*, Probing autoionizing states of molecular oxygen with XUV transient absorption: Electronic-symmetry-dependent line shapes and laser-induced modifications. *Physical review. A* **95,** 043427 (2017).

[64] Plunkett, A. *et al.*, Ultrafast Rydberg-state dissociation in oxygen: Identifying the role of multielectron excitations. *Physical review. A* **99,** 063403 (2019).

[65] Codling, K. and R. P. Madden, New Rydberg Series in Molecular Oxygen near 500 Å. *Journal of Chemical Physics (U.S.)* **42,** 3935-3938 (1965).

[66] O Edqvist *et al.*, On the Photoelectron Spectrum of O2. *Physica scripta* **1,** 25-30 (1970).

[67] Tanakaa), K. and M. Yoshimine, A theoretical study of the predissociation of the c 4 Σ − u state of O + 2. *The Journal of chemical physics* **70,** 1626-1633 (1979).

[68] Dillon, M. A. and David Spence, A new, optically forbidden Rydberg series in O2 converging to the O+2 c 4Σ− u limit. *The Journal of chemical physics* **74,** 6070-6074 (1981).

[69] Frasinski, L. J.,K. J. Randall and K. Codling, Predissociation of the c4Σu- state of O2. *Journal of physics. B, Atomic and molecular physics* **18,** L129 (1985).

[70] Richard-Viard, M. *et al.*, Isotope effect in the predissociation of the c4Σu- state of O+2. *Journal of physics. B, Atomic and molecular physics* **20,** 2247 (1987).

[71] Gallagher, J. W. *et al.*, Absolute Cross Sections for Molecular Photoabsorption, Partial Photoionization, and Ionic Photofragmentation Processes. *Journal of physical and chemical reference data* **17,** 9-153 (1988).

[72] Baltzer, P. *et al.*, High-resolution inner-valence uv photoelectron spectra of the O 2 molecule and configuration-interaction calculations of Π u 2 states between 20 and 26 eV. *Physical review. A, Atomic, molecular, and optical physics* **45,** 4374-4384 (1992).

[73] Holland, D. M. P. *et al.*, A study of the absolute photoabsorption, photoionization and photodissociation cross sections and the photoionization quantum efficiency of oxygen from the ionization threshold to 490 Å. *Chemical physics* **173,** 315-331 (1993).

[74] Ellis, K. *et al.*, High resolution threshold photoelectron and photoion spectroscopy of oxygen in the 12-50 eV photon range. *Journal of physics. B, Atomic, molecular, and optical physics* **27,** 3415-3426 (1994).

[75] Liebel, H. *et al.*, Neutral photodissociation of O2 Rydberg states accompanied by changes of the Rydberg electron's quantum numbers n and l. *Physics letters. A* **267,** 357-369 (2000).

[76] Karawajczyk, A. *et al.*, Neutral fragmentation of superexcited oxygen molecules. *Physical review. A, Atomic, molecular, and optical physics* **61,** 032718 (2000).

[77] Demekhin, F. V. *et al.*, The predissociation of the 2σ
−1
u(c 4Σ
–
u, v states of the oxygen molecular ion. *Russian journal of physical chemistry. B* **1,** 213 (2007).

[78] Demekhin, P. V. *et al.*, Investigation of photoionization and photodissociation of an oxygen molecule by the method of coupled differential equations. *Optics and spectroscopy* **102,** 318-329 (2007).

[79] Padmanabhan, A. *et al.*, An angle-resolved dissociative photoionization study of the c4Σ−u state in O+2 using the TPEPICO technique. *Journal of physics. B, Atomic, molecular, and optical physics* **43,** 165204 (2010).

[80] Peng, P. *et al.*, Symmetry of molecular Rydberg states revealed by XUV transient absorption spectroscopy. *Nature Communications* **10,** 5269-8 (2019).

[81] Taylor, J. R., *Scattering theory: the quantum theory of nonrelativistic collisions*. (Dover Publications, 2012).

[82] Ukai, M. *et al.*, State-to-State Behavior in the Neutral Dissociation of O 2 Far beyond the Ionization Threshold. *Physical review letters* **74,** 239-242 (1995).

[83] Piancastelli, M. N. *et al.*, Bond-distance-dependent decay probability of the N 1s →π core-excited state in N2. *Journal of physics. B, Atomic, molecular, and optical physics* **33,** 1819 (2000).

[84] Bian, Q. *et al.*, Bond-distance-dependent Auger decay of core-excited N 2 using an ultrashort x-ray pump and continuous-wave IR-control scheme. *Physical review. A* **99,** 033404 (2019).

[85] Rundquist, A. *et al.*, Phase-Matched Generation of Coherent Soft X-rays. *Science* **280,** 1412-1415 (1998).

[86] Wang, H. *et al.*, Attosecond Time-Resolved Autoionization of Argon. *Physical review letters* **105,** 143002 (2010).

[87] Chini, M. *et al.*, Subcycle ac Stark Shift of Helium Excited States Probed with Isolated Attosecond Pulses. *Physical review letters* **109,** 073601 (2012).

[88] Ott, C. *et al.*, Lorentz Meets Fano in Spectral Line Shapes: A Universal Phase and Its Laser Control. *Science (American Association for the Advancement of Science)* **340,** 716-720 (2013).

[89] Beck, A. R. *et al.*, Attosecond transient absorption probing of electronic superpositions of bound states in neon: detection of quantum beats. *NJP* **16,** 113016-12 (2014).

[90] Li, X. *et al.*, Investigation of coupling mechanisms in attosecond transient absorption of autoionizing states: comparison of theory and experiment in xenon. *JPB* **48,** 125601-10 (2015).

[91] Warrick, E. R. *et al.*, Probing the Dynamics of Rydberg and Valence States of Molecular Nitrogen with Attosecond Transient Absorption Spectroscopy. *The journal of physical chemistry. A, Molecules, spectroscopy, kinetics, environment, & general theory* **120,** 3165-3174 (2016).

[92] Warrick, E. R. *et al.*, Attosecond transient absorption spectroscopy of molecular nitrogen: Vibrational coherences in the b′ 1Σ+u state. *Chemical physics letters* **683,** 408-415 (2017).

[93] Kobayashi, Y. *et al.*, Direct mapping of curve-crossing dynamics in IBr by attosecond transient absorption spectroscopy. *Science (American Association for the Advancement of Science)* **365,** 79-83 (2019).

[94] Stratmann, R. E. and Robert R. Lucchese, A graphical unitary group approach to study multiplet specific multichannel electron correlation effects in the photoionization of O2. *The Journal of chemical physics* **102,** 8493-8505 (1995).

[95] Stratmann, R. E.,Robert W. Zurales and Robert R. Lucchese, Multiplet-specific multichannel electron-correlation effects in the photoionization of NO. *The Journal of chemical physics* **104,** 8989-9000 (1996).

[96] LUCCHESE, R. R., Effects of interchannel coupling on the photoionization cross sections of carbon dioxide. *The Journal of chemical physics* **92,** 4203-4211 (1990).

[97] Lafosse, A. *et al.*, Vector correlations in dissociative photoionization of O2 in the 20–28 eV range. II. Polar and azimuthal dependence of the molecular frame photoelectron angular distribution. *The Journal of chemical physics* **117,** 8368-8384 (2002).

[98] Lin, P. and Robert R. Lucchese, Theoretical studies of cross sections and photoelectron angular distributions in the valence photoionization of molecular oxygen. *The Journal of chemical physics* **116,** 8863-8875 (2002).

[99] Dunning, T. H., Gaussian basis sets for use in correlated molecular calculations. I. The atoms boron through neon and hydrogen. *The Journal of chemical physics* **90,** 1007-1023 (1989).

[100] KENDALL, R. A.,T. H. DUNNING and R. J. HARRISON, Electron affinities of the first-row atoms revisited. Systematic basis sets and wave functions. *The Journal of chemical physics* **96,** 6796-6806 (1992).

[101] Werner, H. *et al.*, Molpro: a general-purpose quantum chemistry program package. *Wiley interdisciplinary reviews. Computational molecular science* **2,** 242-253 (2012).

[102] O'Malley, T. F., Theory of Dissociative Attachment . *Physical review* **150,** 14-29 (1966).

[103] Dubé, L. and A. Herzenberg, Absolute cross sections from the "boomerang model" for resonant electron-molecule scattering. *Phys. Rev., A; (United States)* **20,** 194-213 (1979).

[104] Haxton, D. J.,T. N. Rescigno and C. W. McCurdy, Dissociative electron attachment to the H 2 O molecule. II. Nuclear dynamics on coupled electronic surfaces within the local complex potential model. *Physical review. A, Atomic, molecular, and optical physics* **75,** 012711 (2007).

[105] Simon, B., The definition of molecular resonance curves by the method of exterior complex scaling. *Physics letters. A* **71,** 211-214 (1979).

[106] McCurdy, C. W.,M. Baertschy and T. N. Rescigno, Solving the three-body Coulomb breakup problem using exterior complex scaling. *Journal of Physics B:Atomic, Molecular and Optical Physics* **37,** R137-R187 (2004).

[107] McCurdy, C. W. and Fernando Martín, Implementation of exterior complex scaling in B-splines to solve atomic and molecular collision problems. *Journal of physics. B, Atomic, molecular, and optical physics* **37,** 917-936 (2004).

[108] Vanroose, W. *et al.*, Double photoionization of aligned molecular hydrogen. *Physical review. A, Atomic, molecular, and optical physics* **74,** 052702 (2006).

[109] Scrinzi, A., Infinite-range exterior complex scaling as a perfect absorber in time-dependent problems. *Physical review. A, Atomic, molecular, and optical physics* **81,** 053845 (2010).

[110] Hvizdoš, D. *et al.*, Dissociative recombination by frame transformation to Siegert pseudostates: A comparison with a numerically solvable model. *Physical review. A* **97,** 022704 (2018).

[111] Codling, K.,L. J. Frasinski and K. J. Randall, Competition between autoionisation and predissociation in the Rydberg series approaching the c4Σu- state of O2. *Journal of physics. B, Atomic and molecular physics* **18,** L251 (1985).

[112] E. Merzbacher, *Quantum mechanics*. (John Wiley, 1970).

[113] Mukamel, S., *Principles of nonlinear optical spectroscopy*. (Oxford University Press, New York ; Oxford, 1995).

[114] Moody, G. *et al.*, Intrinsic homogeneous linewidth and broadening mechanisms of excitons in monolayer transition metal dichalcogenides. *Nature communications* **6,** 8315 (2015).

[115] Coen, S. *et al.*, Supercontinuum generation by stimulated Raman scattering and parametric four-wave mixing in photonic crystal fibers. *Journal of the Optical Society of America. B, Optical physics* **19,** 753 (2002).

[116] Drescher, L. *et al.*, Extreme-ultraviolet spectral compression by four-wave mixing. *Nature photonics* **15,** 263-266 (2021).

[117] Krausz, F. *et al.*, Attosecond metrology. *Nature* **414,** 509-513 (2001).

[118] GOULIELMAKIS, E. *et al.*, Real-time observation of valence electron motion. *Nature* **466,** 739-743 (2010).

[119] Cao, W. *et al.*, Attosecond transient absorption of argon atoms in the vacuum ultraviolet region: line energy shifts versus coherent population transfer. *NJP* **18,** 013041 (2016).

[120] Kobayashi, Y. *et al.*, Selectivity of Electronic Coherence and Attosecond Ionization Delays in Strong-Field Double Ionization. *Physical review letters* **120,** 233201 (2018).

[121] Kelkensberg, F. *et al.*, Electron localization following attosecond molecular photoionization. *Nature* **465,** 763-766 (2010).

[122] Calegari, F. *et al.*, Ultrafast electron dynamics in phenylalanine initiated by attosecond pulses. *Science (American Association for the Advancement of Science)* **346,** 336-339 (2014).

[123] SCHULTZE, M. *et al.*, Controlling dielectrics with the electric field of light. *Nature (London)* **493,** 75-78 (2013).

[124] Schultze, M. *et al.*, Attosecond band-gap dynamics in silicon. *Science (American Association for the Advancement of Science)* **346,** 1348-1352 (2014).

[125] Zürch, M. *et al.*, Direct and simultaneous observation of ultrafast electron and hole dynamics in germanium. *Nature communications* **8,** 15734 (2017).

[126] Lashof, D. A. and Dilip R. Ahuja, Relative contributions of greenhouse gas emissions to global warming. *Nature (London)* **344,** 529-531 (1990).

[127] Tanaka, Y. and M. Ogawa, RYDBERG ABSORPTION SERIES OF CO2 CONVERGING TO THE 2Πu STATE OF. *Canadian journal of physics* **40,** 879-886 (1962).

[128] Cook, G. R.,P. H. Metzger and M. Ogawa, Absorption, Photoionization, and Fluorescence of CO2. *The Journal of chemical physics* **44,** 2935-2942 (1966).

[129] Dibeler, V. H. and James A. Walker, Mass-Spectrometric Study of Photoionization VI O_2, CO_2, COS, and CS_2. *Journal of the Optical Society of America (1930)* **57,** 1007 (1967).

[130] Wang, L. *et al.*, High resolution UV photoelectron spectroscopy of CO +2, COS + and CS +2 using supersonic molecular beams. *Journal of electron spectroscopy and related phenomena* **47,** 167-186 (1988).

[131] Parr, A. C. *et al.*, Selective population of spin–orbit levels in the autoionization of a polyatomic molecule: Branching ratios and asymmetry parameters for the Tanaka–Ogawa Rydberg series in CO2. *The Journal of chemical physics* **100,** 8768-8779 (1994).

[132] Shaw, D. A. *et al.*, A study of the absolute photoabsorption, photoionisation and photodissociation cross sections and the photoionisation quantum efficiency of carbon dioxide from the ionisation threshold to 345 Å. *Chemical physics* **198,** 381-396 (1995).

[133] Liu, J.,M. Hochlaf and C. Y. Ng, Pulsed field ionization–photoelectron bands for CO2+(A 2Πu and B 2Σu+) in the energy range of 17.2–19.0 eV: An experimental and theoretical study. *The Journal of chemical physics* **113,** 7988-7999 (2000).

[134] Furch, F. J. *et al.*, Photoelectron imaging of XUV photoionization of CO2 by 13-40 eV synchrotron radiation. *The Journal of chemical physics* **139,** 124309 (2013).

[135] Timmers, H. *et al.*, Coherent Electron Hole Dynamics Near a Conical Intersection. *Physical review letters* **113,** 113003 (2014).

[136] Chang, Z.,Paul B. Corkum and Stephen R. Leone, Attosecond optics and technology: progress to date and future prospects [Invited]. *Journal of the Optical Society of America. B, Optical physics* **33,** 1081-1097 (2016).

[137] Jin, C. *et al.*, Theoretical study of photoelectron angular distributions in single-photon ionization of aligned N 2 and CO 2. *Physical review. A, Atomic, molecular, and optical physics* **81,**(2010).

[138] Lucchese, R. R. *et al.*, Asymmetry in the molecular-frame photoelectron angular distribution for oxygen 1s photoemission from CO2. *JPhysB* **45,** 194014 (2012).

[139] G. Herzberg, *Molecular Spectra and Molecular Structure. III. Electronic Spectra and Electronic Structure of Polyatomic Molecules*. (Van Nostrand–Reinhold, New York, 1966).

[140] Kaufmann, K.,W. Baumeister and M. Jungen, Universal Gaussian basis sets for an optimum representation of Rydberg and continuum wavefunctions. *Journal of physics. B, Atomic, molecular, and optical physics* **22,** 2223-2240 (1989).

[141] Oudar, J. and Y. R. Shen, Nonlinear spectroscopy by multiresonant four-wave mixing. *Phys. Rev., A; (United States)* **22,** 1141-1158 (1980).

[142] Wright, J. C., Multiresonant Coherent Multidimensional Spectroscopy. *Annual review of physical chemistry* **62,** 209-230 (2011).

[143] Demtröder, W. and Wolfgang Demtroder, *Atoms, Molecules and Photons : An Introduction to Atomic-, Molecular- and Quantum-Physics*. (Springer Berlin Heidelberg, Berlin, Heidelberg, 2006).

[144] Gounand, F., Calculation of radial matrix elements and radiative lifetimes for highly excited states of alkali atoms using the Coulomb approximation. *Journal de Physique* **40,** 457-460 (1979).

[145] Stebbings, R. F., *Rydberg states of atoms and molecules*. (Cambridge Univ. Press, Cambridge, 1983).

[146] Lefebvre-Brion, H. and Robert W. Field, *Perturbations in the spectra of diatomic molecules*. (Academic Pr, Orlando, Fla. [u.a.], 1986).

[147] Pham, K. *et al.*, Coherent Light Shift on Alkaline-Earth Rydberg Atoms from Isolated Core Excitation without Autoionization. *PRX Quantum* **3,** 020327 (2022).

[148] Weinacht, T. C.,J. Ahn and P. H. Bucksbaum, Controlling the shape of a quantum wavefunction. *Nature (London)* **397,** 233-235 (1999).

[149] Corkum, P. B. and Ferenc Krausz, Attosecond science . *Nat Phys* **3,** 381-387 (2007).

[150] Ding, T. *et al.*, Time-resolved four-wave-mixing spectroscopy for inner-valence transitions. *Optics letters* **41,** 709-712 (2016).

[151] Mi, K. *et al.*, Method for high precision measurement of decaying dynamics using attosecond wave-mixing spectroscopy. *Optics express* **29,** 2798-2808 (2021).

[152] Madden, R. P.,D. L. Ederer and K. Codling, Resonances in the Photo-ionization Continuum of Ar i (20-150 eV). *Physical review* **177,** 136-151 (1969).

[153] Baig, M. A. and M. Ohno, On the 3s-subshell excitation spectrum of argon. *Zeitschrift f r Physik D Atoms, Molecules and Clusters* **3,** 369-373 (1986).

[154] Sorensen, S. *et al.*, Argon 3s autoionization resonances. *Physical review. A, Atomic, molecular, and optical physics* **50,** 1218-1230 (1994).

[155] Wu, S. *et al.*, Electron-impact study in valence and autoionization resonance regions of argon. *Physical Review A* **51,** 4494-4500 (1995).

[156] Kelly, H. P. and Raymond L. Simons, Photoabsorption by Neutral Argon Calculated by Many-Body Perturbation Theory. *Physical review letters* **30,** 529-532 (1973).

[157] Robert D. Cowan, *The theory of atomic structure and spectra*. (University of California Press, Berkeley, 1981).

[158] Wu, M. *et al.*, Theory of strong-field attosecond transient absorption. *JPB* **49,** 062003 (2016).

[159] Dai, X. *et al.*, Preparation of a wave packet through a mixed level in Li2; predissociation of one member of the superposition. *Chemical physics letters* **402,** 126-132 (2005).

[160] Grochmalicki, J. and M. Lewenstein, Excitation of Rydberg wavepackets by short laser pulses. *Journal of physics. B, Atomic, molecular, and optical physics* **21,** 3285-3302 (1988).

[161] Raman, C.,M. F. Decamp and P. Bucksbaum, Redistribution of atomic Rydberg states by tunable narrow band picosecond far-infrared pulses. *Optics express* **1,** 186-196 (1997).

[162] Ivanov, M. Y. and Albert Stolow, Coherent control of high- n Rydberg lifetimes using wavepacket technology. *Chemical Physics Letters* **265,** 231-238 (1997).

[163] Weinacht, T. C.,J. Ahn and P. H. Bucksbaum, Measurement of the Amplitude and Phase of a Sculpted Rydberg Wave Packet. *Physical review letters* **80,** 5508-5511 (1998).

[164] Stavros, V. G. and H. H. Fielding, Influence of weak electric fields on Rydberg electron wavepacket dynamics in the radial coordinate. *Chemical physics letters* **284,** 93-100 (1998).

[165] Dai, X. and Stephen R. Leone, Control of wave packets in Li2 by shaping the pump and probe pulses for a state-selected pump-probe analysis of the ionization continuum. *The Journal of chemical physics* **127,** 014312 (2007).

[166] Knappenberger, K. L. *et al.*, Stark-assisted population control of coherent CS2 4f and 5p Rydberg wave packets studied by femtosecond time-resolved photoelectron spectroscopy. *The Journal of chemical physics* **127,** 124318 (2007).

[167] Plunkett, A. *et al.*, Raman Interferometry between Autoionizing States to Probe Ultrafast Wave-Packet Dynamics with High Spectral Resolution. *Physical review letters* **128,** 083001 (2022).

[168] King, G. C. *et al.*, An investigation of the structure near the L2,3 edges of argon, the M4,5 edges of krypton and the N4,5 edges of xenon, using electron impact with high resolution. *Journal of physics. B, Atomic and molecular physics* **10,** 2479 (1977).

[169] Masui, S. *et al.*, New measurements of the widths of the Xe 4d levels. *Journal of physics. B, Atomic, molecular, and optical physics* **28,** 4529-4536 (1995).

[170] Sairanen, O. *et al.*, High-resolution pre-edge structure in the inner-shell ionization threshold region of rare gases Xe, Kr, and Ar. *Physical review. A, Atomic, molecular, and optical physics* **54,** 2834-2839 (1996).

[171] Lin, M. *et al.*, Strong-field induced XUV transmission and multiplet splitting in 4d(-1)6p core-excited Xe studied by femtosecond XUV transient absorption spectroscopy. *The Journal of chemical physics* **137,** 244305 (2012).

[172] Kobayashi, Y. *et al.*, Attosecond transient-absorption dynamics of xenon core-excited states in a strong driving field. *Physical review. A* **95,** 031401 (2017).

[173] Anand, M. *et al.*, Attosecond counter-rotating-wave effect in xenon driven by strong fields. *Physical review. A* **95,** 053420 (2017).

[174] Kolbasova, D. *et al.*, Probing ultrafast coherent dynamics in core-excited xenon by using attosecond XUV-NIR transient absorption spectroscopy. *Physical review. A* **103,** 043102 (2021).

[175] Shiner, A. D. *et al.*, Wavelength scaling of high harmonic generation efficiency. *Physical Review Letters* **103,** 073902 (2009).

[176] Cousin, S. L. *et al.*, High-flux table-top soft x-ray source driven by sub-2-cycle, CEP stable, 185-μm 1-kHz pulses for carbon K-edge spectroscopy. *Optics letters* **39,** 5383-5386 (2014).

[177] Ishii, N. *et al.*, Carrier-envelope phase-dependent high harmonic generation in the water window using few-cycle infrared pulses. *Nature Communications* **5,** 3331 (2014).

[178] Stein, G. J. *et al.*, Water-window soft x-ray high-harmonic generation up to the nitrogen K-edge driven by a kHz, 2.1 μ m OPCPA source. *Journal of physics. B, Atomic, molecular, and optical physics* **49,** 155601 (2016).

[179] Attar, A. R. *et al.*, Femtosecond x-ray spectroscopy of an electrocyclic ring-opening reaction. *Science (American Association for the Advancement of Science)* **356,** 54-59 (2017).

[180] Barreau, L. *et al.*, Efficient table-top dual-wavelength beamline for ultrafast transient absorption spectroscopy in the soft X-ray region. *Scientific Reports* **10,** 5773 (2020).

[181] Schirmer, J., A. Barth and F. Tarantelli, *Theoretical study of K-shell excitations in formaldehyde.* (1988) 10.1016/0301-0104(88)87254-9.

[182] Moule, D. C. and A. D. Walsh, Ultraviolet spectra and excited states of formaldehyde. *Chemical reviews* **75,** 67-84 (1975).